Radiation Effects in Optical Link Components for Future Particle Physics Detectors

Pavel Stejskal

CERN, CH-1211 Genève 23, Switzerland
Blackett Laboratory, Imperial College, London SW7 2AZ, United Kingdom

A thesis submitted to Imperial College London
for the degree of Doctor of Philosophy

March 2013

I declare that I have elaborated this thesis independently, citing all information sources that I used.

Brno, 25.3.2013 Pavel Stejskal

Abstract

Optical link components used in future particle physics experiments will typically be exposed to intense radiation fields during the lifetime of the experiment and the qualification of these components in terms of radiation tolerance is thus required. Data on semiconductor lasers and photodiodes for use in 10 Gb/s datalinks tested during high-fluence (in excess of 10^{15} particles/cm^2) neutron and pion irradiation in 2009 and 2010 are presented with annealing data. In order to predict the behaviour of a laser irradiated with the different particle fluxes at different locations inside a particle physics experiment, radiation damage in lasers has been modelled. The model describes the degradation of the *L-I* characteristic of a semiconductor laser undergoing irradiation with the annealing processes taken into account. The robustness of the model has been checked against the experimental data. Additionally, the author's method to estimate Single Event Upsets in photodetectors using GEANT4 is presented. Use of optoelectronic devices in digital data transmission systems in HEP detectors is also discussed.

Acknowledgements

In the first place I would like to thank to my supervisors Jan Troska and Geoff Hall for their valuable advice, enduring guidance and for encouraging and supporting me in all my efforts.

My greatest words of thanks also belong to Asen Christov for his worthy help and advice concerning FLUKA simulations of various materials, to Otilia Militaru of UCL and Maurice Glaser of CERN for their valuable help with preparation and execution of the neutron and pion tests, respectively.

Last but not least, I thank to the whole Opto group in CERN for an enjoyable and productive working environment they are creating.

Contents

List of Abbreviations

ADC	Analogue to Digital Converter
ALICE	A Large Ion Collider Experiment
APD	Avalanche Photo-Diode
ASIC	An Application-Specific Integrated Circuit
ATLAS	A Toroidal LHC Aparatus
BD	Blue-Ray Disc
BER	Bit-Error Rate
CD	Compact Disc
CERN	Organisation (originally Conseil) Européenne pour la Recherche Nucléaire
CMOS	Complementary Metal–Oxide–Semiconductor
CMS	Compact Muon Solenoid
COTS	Commercial Off-The-Shelf
DAQ	Data Acquisition
DBR	Distributed Bragg Reflector
DUT	Device Under Test
DVB	Digital Video Broadcasting
DVD	Digital Video Disc
ECAL	Electromagnetic Calorimeter
EMI	Electromagnetic Interference
ESD	Electrostatic Discharge
FEC	Forward Error Correction
FPGA	Field Programmable Gate Array
GBT	GigaBit Transceiver
GUT	Grand Unified Theory
HEP	High Energy Physics
HL-LHC	High Luminosity Large Hadron Collider
LASER	Light Amplification by Stimulated Emission of Radiation
LED	Light-Emitting Diode
LEP	Large Electron Positron Collider
LHC	Large Hadron Collider
LHCb	Large Hadron Collider Beauty Experiment
lp-SPL	Low Power Superconducting Proton Linac
LVDS	Low Voltage Differential Signaling
NIEL	Non-Ionizing Energy Loss
NRZ	Non-Return-to-Zero
OMA	Optical Modulation Amplitude

PS	Proton Synchrotron
PSB	Proton Synchrotron Booster
PSI	Paul Scherrer Institut
QCD	Quantum Chromodynamics
RIN	Relative Intensity Noise
ROSA	Receiver Optical Sub-Assembly
SEU	Single Event Upset
SFP	Small Form-Factor Pluggable
SLHC	Super Large Hadron Collider
SM	Standard Model
SPS	Super Proton Synchrotron
TIA	Transimpedance Amplifier
TOSA	Transmitter Optical Sub-Assembly
TOTEM	Total Cross Section and Elastic Scattering Measurement
TTC	Timing, Trigger and Control
UCL	Université Catholique de Louvain
VCSEL	Vertical-Cavity Surface-Emitting Laser

Chapter 1

Introduction

This chapter gives a brief introduction into the world of high energy physics with emphasis on the importance of optical communication systems in today's high energy physics experiments, mainly the experiments on Large Hadron Collider (LHC) at CERN. The ongoing upgrade projects of the LHC are summarised, together with the projects to develop future radiation hard optical links for the LHC experiment upgrades.

1.1 Physics motivation

Since the dawn of time, Man has been trying to understand the origin of the world, to find the answer to the fundamental question: "Where does it all come from?" The modern field of High Energy Physics continues this search for an explanation, shedding light upon the basic building blocks of matter and their mutual interactions.

At the present time it is believed that the building blocks of matter consist of six *quarks* and six *leptons* with their mirror particles, so called antiparticles. These particles interact by the exchange of force-mediating particles known as *bosons*. We identify four fundamental forces: *strong*, *electromagnetic*, *weak* and *gravitational*. All of them have associated particles that mediate the corresponding interaction. For the strong force it is a gluon, the electromagnetic interaction is mediated by a photon, the weak force is caused by the exchange of $W^{\pm}$ and Z^0 bosons and it is assumed that the gravitational force is mediated by hypothetical gravitons. These elementary building blocks of matter along with the force-mediating particles (except the graviton) are described together by a single theory, the *Standard Model of Particle Physics*.

The Standard Model (SM) is a very successful theory which explains, within experimental precision, all experimental phenomena so far observed in the laboratory and also predicts new ones. However, it is not a definitive theory and it suffers from several limitations. First of all, it does not account for gravity. The origin of mass is not resolved; the masses of all particles in the SM have to be determined experimentally. Furthermore, the SM cannot explain some cosmological phenomena like the origin of *Dark Matter* and why the excess of matter over anti-matter is observed in the Universe.

Results obtained from new high-energy physics experiments can lead to the failure of SM predictions so New Physics can be revealed. One of these state-of-the-art facilities is the *Large Hadron Collider* at CERN with its main four experiments which are now playing a crucial role in our future understanding of the laws of Nature.

The physics reach of all particle physics experiments is very closely linked to the sophistication of the available instrumentation. All sort of instruments are used to collect the signals from sensors to amplify, digitize, transfer, process and store them with the highest possible speed and precision. Such tasks are very demanding in terms of resources, and therefore very expensive and complex apparatus must be developed. Optical data transmission systems, which are one such example, play a substantial role in the readout and control of current particle physics detectors. As these systems are operated in high radiation environment, extensive studies have been carried out to understand their behaviour under irradiation.

1.1.1 The Standard Model

More than 20 years ago, S. Glashow, A. Salam and S. Weinberg elaborated the *Standard Model of Electro-Weak Interactions* which earned them the Nobel Prize in 1979. This theory combined with *Quantum Chromodynamics* (QCD), forms a more general theory called *Standard Model*, which is the most successful theory of elementary particles at the present time.

The Standard Model is a low-energy model, consistent with existing experimental observations, which may be part of a more fundamental theory, the *Grand Unified Theory* (GUT) – not elaborated yet. The Standard Model is able to describe a vast amount of experimental data but unanswered questions still exist. One of them is a fact that *Charge conjugation* (C – transforms particle into its antiparticle), *Parity* (P – creates the mirror image of a physical system), *Time reversal* (T) symmetries and the CP product of two symmetries are slightly violated during certain types of weak decays. In contrast these symmetries are conserved in strong and electromagnetic interactions.

The Standard Model of particle physics is a theory which describes three of the four known fundamental interactions between the elementary particles that make up all matter. These three forces are the strong, weak and electromagnetic force described by the interactions via gauge boson exchange.

Constituents of matter

Among fermions, the fundamental constituents of the matter with non-integer spin, the leptons and the quarks can be distinguished. They can be organised in a structure of twelve particles (six leptons and six quarks) with their antiparticle counterparts and are classified in three families, the so-called generations (see Table 1.1).

Leptons and quarks form two different groups of particles. The main difference between them is that quarks, unlike leptons, participate in strong interactions. Other characteristics of quarks and leptons are:

	1st Generation		2nd Generation		3rd Generation	
Quarks	u d	*up* *down*	c s	*charm* *strange*	t b	*top* *bottom*
Leptons	ν_e e	*electron neutrino* *electron*	ν_μ μ	*muon neutrino* *muon*	ν_τ τ	*tau neutrino* *tau*

Table 1.1: Organization of fundamental fermions.

- Each quark carries one of three color charges: red, green or blue. This color charge enables them to feel the strong force.
- The up-type quarks (up, charm and top) carry an electric charge of +2/3, and the down-type quarks (down, strange and bottom) carry an electric charge of –1/3, enabling both types to participate in electromagnetic interactions.
- Leptons do not carry any color charge.
- The up–type leptons (the neutrinos) carry no electric charge. They do not participate in electromagnetic or strong interactions.
- The down-type leptons (electron, muon and tau) carry an electric charge of –1 so they are sensitive to the electromagnetic field.
- Both quark and leptons feel the weak force.

All stable matter is formed only from quarks and leptons of the first generation.

Force-mediating particles

In the Standard Model all interactions are mediated by the exchange of particles. These particles are bosons, i.e. they have an integer spin. The different types of force-mediating particles are:

- **Photons** – massless particles which mediate the electromagnetic force between electrically charged particles.
- $\mathbf{W^+}$, $\mathbf{W^-}$ and $\mathbf{Z^0}$ **gauge bosons** – massive particles mediating the weak interaction between quarks and leptons.
- Eight **gluons** – massless particles responsible for the strong interactions. These particles can interact among themselves.

The Standard Model predicts also one boson that has been only recently observed [84]. It is the so-called *Higgs boson*, a massive elementary particle playing a key role in explaining the origins of the mass of elementary particles. The search for this particle has been very intensive

but, until recently, the evidence for the existence of Higgs boson has been indirect. It is expected that LHC will be able to confirm its reality. Recent results have identified a boson with spin not equal to 1 and with a mass of about 125 GeV which appears to be consistent with the Higgs boson. However, more work and data are required to confirm that all its properties are those expected.

The limitations of the Standard Model

As already stated, the Standard Model is a successful description of particle physics; however, some weaknesses are still present. Firstly, it incorporates a rather high number (19) of free parameters. Furthermore, neither the gravitational force is included nor the origin of the mass is explained in the Standard Model – masses have to be determined experimentally. The observed difference between the presence of matter and antimatter in the universe cannot be explained by the Standard Model either. However, despite these weak points, the Standard Model remains the most accurate and experimentally proven theory in Particle Physics. On the other hand it is the major ambition of Particle Physics to detect effects unexplainable by the Standard Model.

1.1.2 Testing of the Standard Model and beyond

The Standard Model outlined in previous section was verified, except the Higgs boson, by experiments at Large Electron Positron (LEP) collider at CERN. As already mentioned, the description of matter by the Standard Model is incomplete and raises many questions which remain unanswered. To improve our understanding of the working of the Universe, a Large Hadron Collider (LHC) was built, partly using infrastructure of its predecessor LEP. Its main purpose is to search for the Higgs and Beyond Standard Model physics, which might include supersymmetric particles (ATLAS and CMS), the study of the quark-gluon plasma in Pb-Pb collisions (ALICE) and of CP violation and B-physics (LHCb). Possible indications of physics beyond the Standard Model as well as the measurements of total cross section, elastic scattering and diffractive processes (TOTEM) are also of interest.

The Large Hadron Collider

The LHC is a two-ring, superconducting accelerator and collider built in the 27 km long LEP tunnel. It is constructed to deliver up to 14 TeV center of mass collision energies.

The Figure 1.1 shows an overview of the LHC accelerator complex and the locations of individual detectors in the LHC beam. Acceleration of protons up to 50 MeV starts in the linear accelerator (Linac). The next accelerating stage is composed of two rings, the *Proton Synchrotron Booster* (PSB), which can boost the particles up to 1.4 GeV, and the *Proton Synchrotron* (PS) which reaches a proton energy of 26 GeV before extraction. The final link in the injector chain for the LHC is the *Super Proton Synchrotron* (SPS) that accelerates protons from the PS to 450 GeV, ready for injection into the LHC.

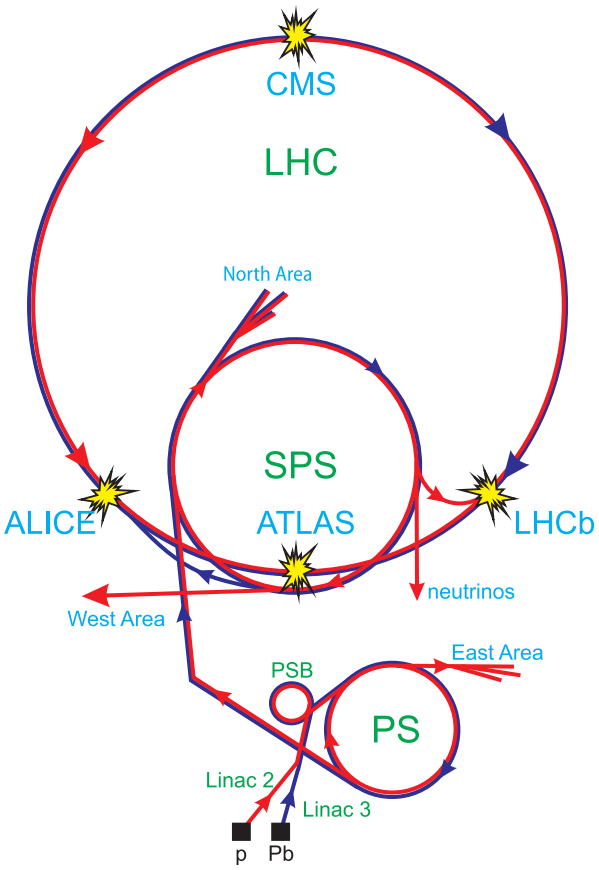

Figure 1.1: The LHC accelerator complex. The accelerating path for the protons and Pb ions is marked in red and blue respectively.

Performance of the LHC The number of events per second N_{ev} generated in the LHC collisions is given by:

$$N_{ev} = L\sigma_{ev} \tag{1.1}$$

where L is the luminosity of the machine, which is one of the main parameters of the accelerator, and σ_{ev} is the cross section for the process under study.

The machine luminosity depends only on the beam parameters and is expressed (for the Gaussian beam) as:

$$L = \frac{N^2 n_b f \gamma}{4\pi \varepsilon_n \beta^*} F \tag{1.2}$$

where N is the number of protons per bunch, n_b the number of bunches per beam, f the revolution frequency, γ the relativistic gamma factor, ε_n the normalized transverse beam emittance which characterizes the compactness and divergence of the bunches, β^* the beta function at the collision point which measures the ability of magnets to focus the beam at the *Interaction Point* (IP) and F the geometric luminosity reduction factor due to the crossing angle at the IP. The nominal values of these parameters for the LHC are presented in Table 1.2. The plan for the year 2012 was to collide beams with energy of 4 TeV with a bunch spacing of 50 ns delivering an integrated luminosity of at least 15 fb^{-1} by the end of the year. This was achieved, with of 23 fb^{-1} provided to the experiments.

Parameter	Units	Injection	Collision
Proton energy	[GeV]	450	7000
Stored energy per beam	[MJ]	23.3	362
Circulating beam current	[A]	0.582	
Number of particles per bunch	[-]	1.15×10^{11}	
Number of bunches	[-]	2808	
Bunch spacing	[ns]	25	
Revolution frequency	[kHz]	11.245	
Synchrotron radiation power per ring	[W]	6.15×10^{-2}	3.6×10^{3}
Peak luminosity in IP_1 and IP_5	$[cm^{-2}s^{-1}]$	-	1.0×10^{34}
Geometric luminosity reduction factor F	[-]	-	0.836
Relativistic gamma factor γ	[-]	479.6	7461
Normalized transverse beam emittance ε_n	[µm]	3.5	3.75
Beta function at IP_1 and IP_5 (ATLAS & CMS)	[m]	18	0.55
Beta function at IP_2 (ALICE)	[m]	10	0.5 for Pb
Beta function at IP_8 (LHCb)	[m]	10	1–50

Table 1.2: Relevant LHC beam parameters for the peak luminosity and proton operation (data taken from [17]).

There are two major experiments at the LHC demanding the highest possible luminosity: ATLAS and CMS are aiming at a peak luminosity of $L = 1.0 \times 10^{34}\ cm^{-2}s^{-1}$. In addition to these high luminosity experiments there exist two other experiments that require low luminosity (for the proton operation of the LHC). One of them is LHCb with peak luminosity of $L = 2.0 \times 10^{32}\ cm^{-2}s^{-1}$ and second is TOTEM ($L = 2 \times 10^{29}\ cm^{-2}s^{-1}$ with 156 bunches). Peak luminosity required by the dedicated ion experiment ALICE is of $L = 1.0 \times 10^{27}\ cm^{-2}s^{-1}$ for nominal Pb-Pb ion operation with 600 bunches.

The high beam intensities implied by a designed luminosity of $L = 1.0 \times 10^{34}\ cm^{-2}s^{-1}$ exclude the use of antiproton beams and therefore one common vacuum and magnet system for both circulating beams. To collide two beams of equally charged particles requires that opposite polarity magnetic dipole fields are provided for each beam. The LHC is therefore designed as a proton-proton collider with separate magnetic fields and vacuum chambers in the main arcs and with common sections only at the insertion regions where the experimental detectors are located.

Since there is not enough room for two separate rings of magnets in the LEP tunnel, the LHC uses twin bore magnets which consist of two sets of coils and beam channels within the same mechanical structure and cryostat.

The peak beam energy in a storage ring depends on the integrated dipole field along the storage ring circumference. Aiming at peak beam energies of up to 7 TeV inside the existing LEP tunnel a peak dipole field of 8.33 T is required as well as the use of superconducting magnet technology operating at a temperature of 1.9 K.

The High Luminosity Large Hadron Collider

The physics reach of the LHC will be defined by the energy and integrated luminosity delivered to the experiments. In order to push that limit further, the HL-LHC project, formerly known as the *Super Large Hadron Collider* (SLHC), aims to provide approximately a six-fold increase in integrated luminosity from 500 fb^{-1} to 3000 fb^{-1} by 2030. According to the current schedule, the LHC will be upgraded in at least two steps during long shut-downs reaching a peak luminosity of 5×10^{34} $cm^{-2}s^{-1}$ in 2023 [90].

In the first planned long shut-down of the LHC in 2013–2014, interventions are foreseen to permit the machine to operate at its design parameters, i.e. with beams colliding at 7 TeV and with the luminosity of at least 1.0×10^{34} $cm^{-2}s^{-1}$. At a later point, Linac 4, a replacement of Linac 2 with an output energy of 160 MeV, should be ready for commissioning. After this upgrade, peak luminosity could exceed nominal LHC luminosity by a factor of 2.

Further upgrades during long shut-downs in 2018 and possibly in 2022 will require further changes in the injector chain due to the ageing of current machine components. There are currently several ongoing upgrade studies. Linac 4 should be followed by a *Low Power Superconducting Proton Linac* (lp-SPL) with an extraction energy of 4 GeV. The current PS will be possibly replaced by a new 50 GeV synchrotron called PS2 which will, apart from the energy increase, also double the proton flux. There are discussions to upgrade even the SPS to an SPS+ which should inject 1 TeV beam into the LHC ring.

1.2 Overview of optical data transmission links at LHC

Radiation tolerant, high speed optoelectronic data transmission links are fundamental building blocks in today's large scale *High Energy Physics* (HEP) detectors, as exemplified by the four experiments at the *Large Hadron Collider* (LHC) [1, 9, 18, 88]. New experiments or upgrades will impose even more stringent demands on these systems from the point of view of performance and radiation tolerance. This can already be seen from the developments underway for the HL-LHC project.

Optical data transmission systems are highly appealing for use in the high radiation environments that are now present in almost every particle physics experiment. There are several aspects that make optical data link systems advantageous over traditional copper-based solutions. First of all, the maximum achievable data-rate is potentially greater for optical links. Concerning the noise in a transmission system, optical systems are more beneficial as well. They do not suffer from cross-talk and are electrically isolated, consequently no parasitic ground loops are present and they are not susceptible to *Electromagnetic Interference* (EMI).

The optical data links have to fulfill several stringent requirements in order to be qualified for use in physics experiments with a high radiation environment. All the components placed on the detector side of the optical data transmission system must be able to withstand high radiation doses over the entire lifetime of the experiment. Additionally, the amount of material used in

the innermost regions of detectors must be kept to a minimum, since excess material degrades the tracker performance and the resolution of the energy-measuring detectors – calorimeters. Another constraint is the magnetic field in which the devices are operated. The components for the optical data links should not be influenced by the magnetic field and should not perturb it.

The final requirement is that the cost of the readout system remains within acceptable limits. Commercially available devices must be used wherever possible and the development of customized components and systems should be minimized. However, the functional reliability in high radiation environment of the *Commercial Off-The-Shelf* (COTS) devices must be proven. This imposes extensive irradiation testing of components to qualify them for operation.

In the following, three different approaches to implement optical data links in the LHC experiments are discussed. These examples form a representative sample of different approaches to the optical readout of the detectors.

1.2.1 Slow analogue readout and digital control – the CMS Silicon Tracker

The CMS central tracker contains ~ 10 million silicon microstrips arranged in close vicinity of the interaction point. The whole tracker operates at a temperature of −10 °C in a magnetic field of 4 T. Optical data transmission is used for both data readout and control signals. Data generated by the silicon tracker are sent to a counting room over a 65 m long optical link, while timing, trigger and control (TTC) information is passed in both directions between detector and counting room. The schematic view of the CMS tracker readout and control system is shown in Figure 1.2.

The CMS Tracker readout system

Electrical signals from the silicon microstrips are amplified, sampled at the LHC bunch-crossing frequency of 40 MHz and stored in an analogue pipeline memory by the APV front-end ASIC [72]. Upon receipt of a Level-1 Trigger, data from all silicon microstrips are time-multiplexed (256:1) onto 40 000 unidirectional analogue optical data links and transmitted to a Front End Driver (FED) located in a counting room where the data are digitized and formatted before being sent to higher level data acquisition (DAQ) systems. To avoid severe power implications and the need of internal analogue to digital converters (ADC), analogue data transmission at 40 MSamples/s with a dynamic range > 9 bits is used.

The analogue optical readout is a multiway unidirectional system based on *edge-emitting* laser transmitters coupled to single-mode optical fibre; see Figure 1.3. The edge-emitting laser operating at wavelength $\lambda \approx 1310$ nm is directly modulated by the custom-designed laser driver ASIC (LLD). Individual fibres from the pigtailed lasers are connected to a fan-in, which merges single fibres into a 12-fibre ribbon cable. Single ribbon cables are connected to a multi-ribbon cable of 8×12 fibres. In the counting room each ribbon connects directly to a 12-channel analogue receiver module on the FED.

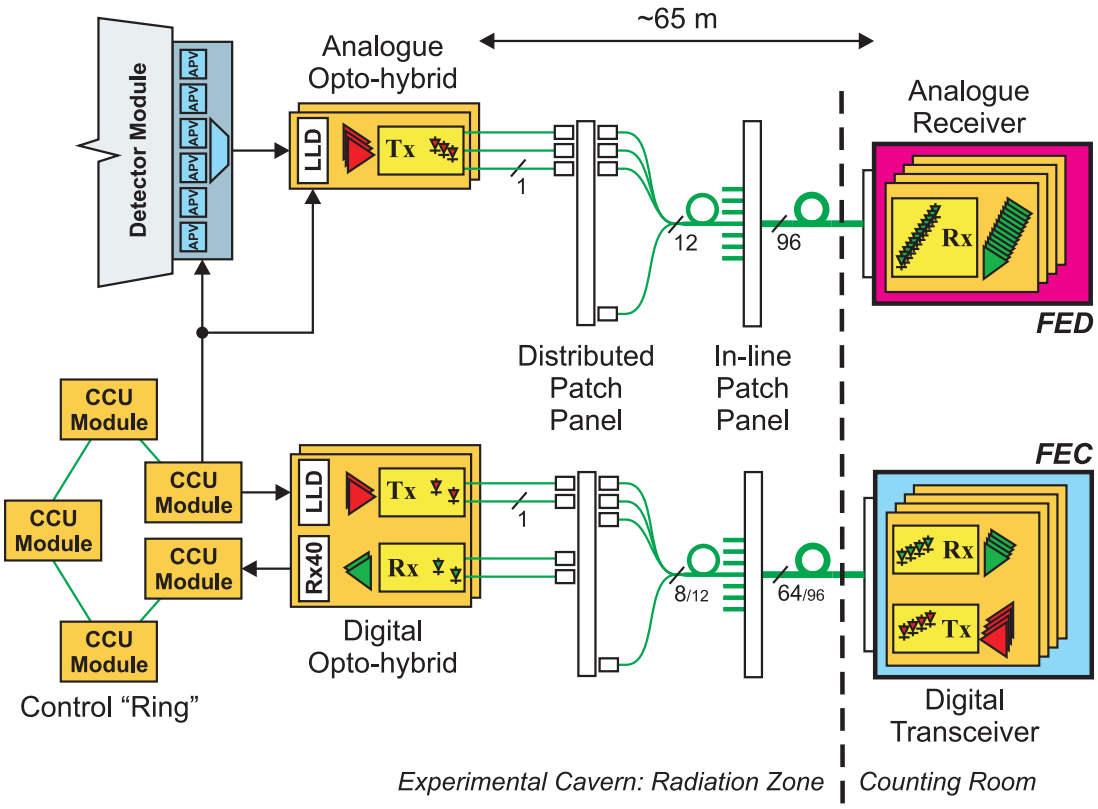

Figure 1.2: Overview of the CMS tracker readout and control systems. The upper part of the image represents the readout path while the bottom one the digital and control path.

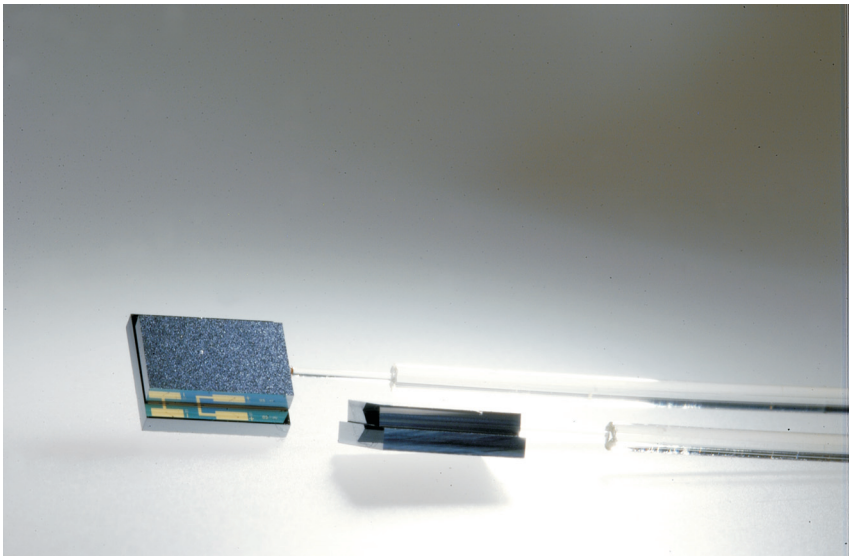

Figure 1.3: The CMS Tracker edge-emitting laser diodes coupled to single-mode optical fibre.

The CMS Tracker control system

The CMS tracker control system is a 2500 channel bi-directional link with control data, clock and trigger signals sent by the Front-End Controller (FEC), located in the counting room, to the Communication and Control Units (CCU) sitting on mechanical substructures of the tracker as well as status data and clock signals returned from the front-end to the back-end. The tracker control system uses a token ring architecture with the FEC acting as a master. The optical signal generated by the FEC is converted to an LVDS electrical signal by the digital optohybrid. These LVDS signals are passed around the ring of CCU modules for processing and then converted back to an optical signal which is returned to the FEC.

Digital control and timing information generated by the FEC is sent by the transmitter-half of a 4-channel digital transceiver on two fibres, see lower part of Figure 1.2. After passing through an identical fibre system to the analogue link, the data are detected by pigtailed InGaAs photodiodes and recovered by a custom-designed digital receiver ASIC (Rx40). After passing around the control ring, data are returned to the receiver part of the digital transceiver using another pair of fibres of the same digital optical link. This bi-directional optical link therefore carries both 40 MHz clock and 40 Mb/s digital control data.

1.2.2 Slow digital readout – the ATLAS Semiconductor Tracker and Pixel Detector

The ATLAS Semiconductor Tracker (SCT) is made of silicon modules mounted on a four-layer barrel around the interaction region and nine disks on either side for end-cap coverage. Each silicon module consist of two single-sided strip detectors. The total number of channels is 6.2×10^6. The SCT operates in a magnetic field of 2 T and the temperature is kept at around $-7\,°C$.

The ATLAS Pixel Detector is composed of three barrel layers cylindrically arranged around the beam axis and three forward and backward disks. The detector consists of 1 744 pixel modules, each containing a silicon sensor read out by 16 front-end chips controlled by a Module Control Chip (MCC). Each module contains 46 080 channels, yielding a total of ~ 80 million channels in the system. The architecture of the optical link system is very similar to the SCT system.

Similarly to the CMS tracker, data generated by the silicon detector modules are sent to a remote counting room, while TTC signals are transferred in the opposite direction. This communication is made by individual optical links which are based on GaAs *Vertical-Cavity Surface-Emitting Lasers* (VCSEL), emitting light at a wavelength λ of 840 nm, and epitaxial Si p-i-n diodes. The whole optical system is illustrated in Figure 1.4.

The SCT readout system

The readout of one SCT module is based on 12 ABCD ASICs [19]. The binary data are stored in a 132 cell deep pipeline memory and read out upon receipt of a Level 1 trigger. Unlike the CMS

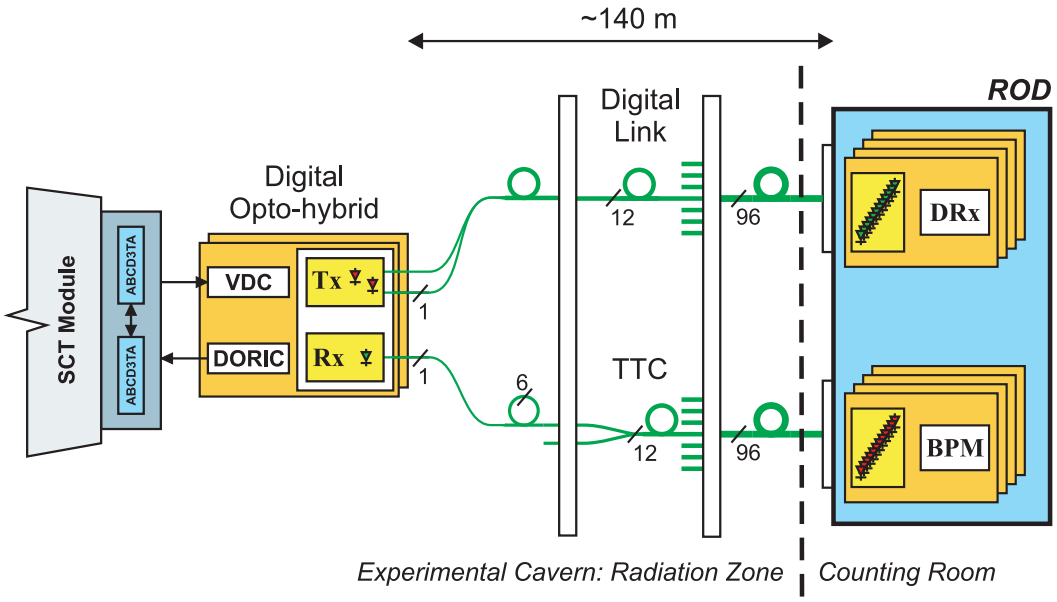

Figure 1.4: Overview of the ATLAS SCT readout and TTC systems. Routing of the readout signals between SCT module and Readout Driver is depicted in the upper part. Control data links are shown in the lower part of the image.

Tracker, the ATLAS SCT uses digital readout of its modules. Binary data from one SCT module are transferred by two optical data links in a *Non-Return-to-Zero* (NRZ) format to the off-detector electronics in the SCT Readout Driver (ROD) located in a counting room.

The digital optical readout of the SCT module is a two channel transmission system operating at 40 Mb/s. The VCSEL Driver Chip (VDC), developed specially for the SCT project, translates LVDS data from the silicon module to the current signal to drive two VCSEL diodes. The VCSELs are contained within the on-detector opto-package, where the light is coupled into a 50 µm diameter multi-mode fibre. As for the CMS tracker, fibres are merged into a 12-fibre ribbon cable and then connected to a 8 × 12 multi-ribbon cable which connects directly to the ROD. In the ROD, the optical signal is converted back to LVDS signal by another custom ASIC, the DRX-12.

The SCT TTC system

Optical links are also used to send the TTC data from the RODs to the SCT modules. The control data links use Bi-Phase Mark (BPM) encoding to combine the 40 MHz machine clock with a 40 Mb/s control data stream. The on-detector Digital Optical Receiver IC (DORIC) decodes the encoded input data to recover the 40 MHz bunch crossing clock and control signals. These TTC signals are transmitted to the front-end ABCD ASICs.

The BPM encoding done by the custom made BPM-12 ASIC located in the ROD, sends transitions corresponding to clock leading edges. The extra transitions at clock trailing edges indicate data logical '1's, see Figure 1.5. The output of the BPM-12 ASIC drives an array of 12 VCSELs which feed the optical signals into 8-ribbon multi-mode optical fibre. The overall optical path distance

is about 140 m. The signal is converted from the optical to electrical domain by on-detector Si p-i-n diodes within the opto-package.

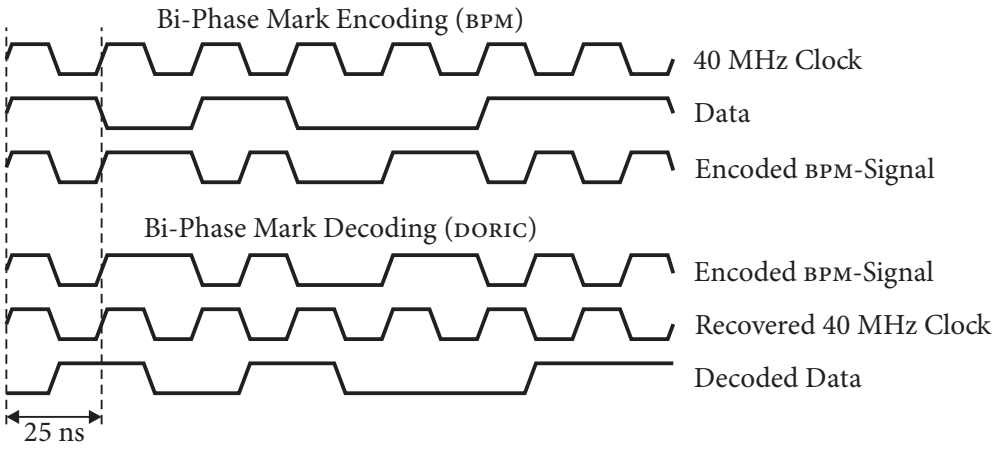

Figure 1.5: The Bi-Phase Mark encoding and decoding scheme.

The ATLAS Pixel readout system

The difference between the ATLAS SCT and Pixel Detector readout system is the separation of the MCC and the opto-board which accomodates VDCs with VCSELs. The MCC outputs the data via ~ 1 m long micro twisted-pair cable to a VDC to drive a VCSEL. Due to the higher data-rate in the Pixel Detector, a higher transmission rate is necessary. In case of the outer layers and the disks of the pixel detector system, the readout data link operates at 80 Mb/s. The innermost layer in the centre of the Pixel Detector will produce higher data-rate of 160 Mb/s, which results in doubling the optical fibres. As in the SCT, the data are sent to the ROD in NRZ format.

Unlike the SCT, the Pixel Detector uses a VCSEL array instead of a single channel device. Two 4-channel VDCs plus one 8-channel VCSEL array are mounted on the opto-board. The innermost layer has in addition two more VDCs and one more VCSEL array to handle the higher occupancy. Each VCSEL array is housed inside an opto-package and coupled to a multi-mode 8-fibre ribbon cable which connects to the 80 m distant counting room.

The ATLAS Pixel TTC system

The ATLAS Pixel TTC System is almost identical to the SCT one. The digital receiver placed on the opto-board is a 4-channel updated version of the SCT DORIC. Two DORICs convert the electrical signal from an 8-channel Si p-i-n array to an LVDS signal which is fed through the micro twisted-pair cable to the MCC. The fibre ribbons are identical to those for the data links.

1.2.3 Fast digital readout – the CMS Electromagnetic Calorimeter

The CMS Electromagnetic Calorimeter (ECAL) is made out of ~ 76 000 lead tungstate ($PbWO_4$) crystals arranged into a barrel and two endcaps inside the Tracker solenoid. The CMS ECAL uses approximately 11 000 optical fibres, each of which is an 800 Mb/s point-to-point digital link that is built using identical or similar components to the CMS Tracker.

The CMS ECAL readout system

The light generated in scintillating $PbWO_4$ crystals is converted by avalanche photodiodes in the barrel and by vacuum phototriodes in the endcaps into an electrical signal which is digitized by a 40 MHz 12-bit ADC. A Front End board takes the signals from groups of 25 channels and calculates basic energy sums, known as trigger primitives. These trigger data together with data from crystals are converted by the Gigabit Optical Link (GOL) Opto-Hybrid (GOH) into an optical signal which is sent through the same optical link system used in the CMS Tracker to the off-detector 12-channel digital receiver module. A proprietary G-Link transmission protocol is used for trigger information, while readout data stream is transmitted using an 8b/10b protocol.

1.2.4 Comparison of technology choices

As described, the ATLAS and CMS collaborations made very different technology choices for their optical link systems. Concerning the component selection, the edge-emitting lasers selected by the CMS are a good choice for the analogue link because of their good linearity and mature technology. VCSELs were the choice made by the ATLAS collaboration due to their low current threshold and high slope efficiency which allows them to operate at low drive currents. In addition, threshold current shifts caused by irradiation are smaller in VCSELs than in edge-emitting lasers. Finally, the cost of a bare 850 nm VCSEL is lower than a bare 1310 nm edge-emitting laser.

The choice of single-mode fibre operated at 1310 nm was made by the CMS Tracker for its analogue readout links. This type of fibre is favoured for long-haul distances because of the lower attenuation. However, for the short optical links used in CMS this has no significant impact. As a matter of fact, the selection of a 1310 nm single-mode fibre turned out to be disadvantageous when looking for receiver modules since devices developed for shorter distances usually operate at 850 nm. Another complication is the small core fibre diameter, typically 8 μm, which makes the alignment of fibres more critical, thus expensive. The ATLAS collaboration chose 850 nm step index multi-mode fibre because of the easier fibre alignment and sufficient bandwidth for the low speed digital links.

The choice of an analogue modulation format by the CMS Tracker significantly constrained the technology choices for its optical link. As a result, the analogue modulation scheme made it impossible to use standard COTS receiver modules and a special receiver ASIC had to be developed. For the HL-LHC, the use of standard digital modulation formats is highly recommended. The

other systems mentioned in this chapter use digital readout. The only drawback is the use of unbalanced NRZ code in the SCT and Pixel readout which requires a careful optimization of receiver thresholds. In the future, balanced digital codes should be employed wherever possible.

While the different technology choices made by the two experiments did not seem to have a major impact on system quality in the very beginning, it turned out that VCSELs used in some subdetectors have had serious reliability problems. These VCSEL failures are occuring with a mean time to failure of approximately one year. The explanation of these failures is the extreme sensitivity of VCSELs to electro-static discharge and humidity [94]. Optical spectrum analysis of the VCSELs proved to be a powerful diagnostic tool and early warning system. The mitigation of these reliability issues is the early replacement of failing devices with more robust ones. In contrast to the VCSELs, CMS edge-emitting lasers are functioning as expected.

Contrary to the early price estimates, which were more favourable for the VCSELs, the cost of all customized links is comparable. The choice of the VCSELs as transmitters in ATLAS experiment seemed to be advantageous because a bare 850 nm VCSEL is cheap but this benefit was diluted since custom device packaging dominates the cost. Furthermore, a multi-mode fibre is more expensive than single-mode which increases the final cost of the link even more.

It should be noted at this point that the experiments at the LHC essentially pioneered the employment of optical links for DAQ and detector control in HEP. At the time of detector readout design – end of the last century – the optical links were common mainly in long-haul telecommunication systems and the market for short distance, high density links was not as developed as it is nowadays. Another aspect is that the HEP community does not present a big customer to manufacturers of optical link components, hence they do not feel the need to develop special radiation-hard components, which in turn means that these have to be stringently tested.

1.3 A radiation-hard readout and control system for HL-LHC detectors

Two projects that aim at development of radiation hard optical links for HL-LHC will be described in this section. These are the Versatile Link project, whose main task is to provide radiation tolerant optical links for future HEP experiments, and the GigaBit Transceiver project which delivers required chip-sets and firmware for these optical links.

1.3.1 The Versatile Link project

The Versatile Link is a project to develop a bi-directional, radiation hard, high speed optical link for future detectors in high energy physics experiments. The versatility of the project means that it will be offered in several variants with many options; in particular, two versions of the link will be provided operating with 1310 nm single-mode and 850 nm multi-mode fibres.

For the LHC detectors, application specific optical links were independently developed for each data acquisition and detector control system resulting in large number of different link architectures. To reduce the final cost of the link and subsequently also the maintenance issues, a single project aiming at developing a versatile link was approved [8]. Thanks to the development of optoelectronic components and ASICs, a general purpose optical link covering most transmission applications can be envisaged. The final functionality will be determined by the link topology and configuration of microcontrollers.

The versatile link will be available with single-mode and also with multi-mode fibres operating at 1310 nm and 850 nm, respectively. This wavelength diversity is offered so that the currently installed optical fibres in the LHC experiments can be reused. Its design data transfer rate is set at ~ 5 Gb/s which is the maximum operating speed of the GBT project. However, most of the components of the versatile link are tested and selected for 10 Gb/s.

A schematic diagram of the Versatile Link is in Figure 1.6. It consist of three main parts, Versatile Transceiver (VTRX), passive optical components and back-end components. Where possible, most of the components will be off-the-shelf to reduce the final cost. The exception is the VTRX which will be placed in areas exposed to high radiation fluxes.

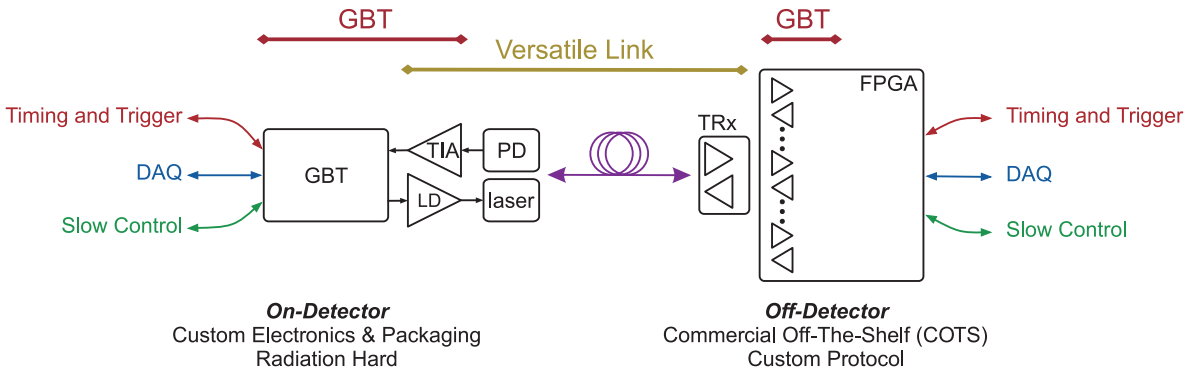

Figure 1.6: Radiation hard optical link architecture.

Since the back-end components are placed in the counting rooms, they do not have to meet the same stringent radiation and magnetic requirements as front-end components. As a result, commercial components will be used for both transmitters and receivers. Single transceivers are readily available for both 850 and 1310 nm wavelengths. Significant improvement in channel density and also cost is achieved by using array transmitters and receivers. Commercial devices meeting Versatile Link specifications are available for both design wavelengths even though the selection of 1310 nm array transmitters is limited.

Concerning passive optical components, the current infrastructure of the LHC experiments will be most likely used in the case that the original wavelength will be preserved. The reason for this is that the bandwidth of installed fibres is sufficient for data transfer at rates up to 10 Gb/s over lengths of 150 m.

The versatile transceiver

Due to the environment in which the VTRX will be operated, it is the only custom developed component of the Versatile Link. It will have to sustain environmental conditions such as a radiation field of $1.5 \times 10^{15}{}_{1\,\mathrm{MeV}}$ neutrons/cm^2 and 500 kGy total dose, magnetic field up to 4 T and wide temperature range from −10 to 40 °C [8]. For this reason, the VTRX has to be a low-volume device made of low-mass, non-magnetic material.

Samples of various commercially available bi-directional transceivers were evaluated with the final verdict that the customized *enhanced small form-factor pluggable* (SFP+) transceiver, which supports data rates up to 10 Gb/s, is the most suitable for the VTRX [7]. In order to meet the environmental constraints, materials of which the SFP+ transceiver is made have to be modified. As an example, the receptacle of the SFP+ transceiver will be custom made from plastic by means of 3D printing. This rapid prototyping method will most likely be used also as a manufacturing method for the final product.

Another customization of the VTRX related to the radiation environment is its internal components. In place of standard laser drivers and photodiode receivers a custom designed radiation hard GBLD and GBTIA are used; see later in this section. Standard SFP+ contains a laser diode mounted in a *transmitter optical sub-assembly* (TOSA) with a p-i-n photodiode mounted in a *receiver optical sub-assembly* (ROSA) together with a *Transimpedance Amplifier* (TIA). This architecture will be preserved in the VTRX except for the standard limiting amplifier in the receiving chain which is already part of the ROSA mounted GBTIA. The optical components, laser diode and p-i-n photodiode, will be standard commercial components capable of operating up to the high fluences present in the HL-LHC trackers.

1.3.2 The GigaBit Transceiver project

The GigaBit Transceiver (GBT) project is the answer to the need for a radiation-hard ASIC for bi-directional optical links capable of sustaining radiation doses planned for the HL-LHC. It aims to provide radiation hard front-end electrical components residing on the detectors as well as a transfer protocol for detector data, timing and trigger signals and slow controls which can be implemented in back-end FPGAS.

The GBT project [67] consist of the following systems: GBTX – a serializer-deserializer chip receiving and transmitting encoded data at 4.8 Gb/s rate with an interface to front-end electronics, GBTIA – a transimpedance amplifier receiving a serial data stream from the photodiode [63], and GBLD – a laser driver to bias and modulate a laser at 4.8 Gb/s [60].

The main challenge of the GBT design is its radiation hardness and robustness against *single event upsets* (SEU). Another HEP specific requirement is the predictable and rather constant latency. These requirements are met by implementation of triple modular redundancy in a commercial radiation resistant 130 nm CMOS technology.

In terms of errors in the data transmission chain due to SEUS, a *forward error correction* (FEC) to maintain low *bit-error rate* (BER) is implemented in a GBT protocol. Channel data are divided

into blocks of k bits to which redundant control bits are added that can, on the receiving side, detect and also correct possible errors that occurred during transmission. The output stream is thus enhanced to $n \geq k$ bits. A GBT frame is composed of a 4 bit header, 4 bit slow control data followed by 80 bits of user data. This frame is coded by a 32 bit long Reed-Solomon code. Reed-Solomon codes, which are used, e.g., in data storage applications or *digital video broadcasting* (DVB) services, can correct bursts of up to $\lfloor (n-k+1)/2 \rfloor$ erroneous symbols. In the GBT case this allows a maximum of 16 erroneous bits that can be corrected.

The GigaBit Transimpedance Amplifier

This 5 Gb/s fully differential optical receiver, designed specifically for highly degraded photodiodes operated in harsh radiation fields, incorporates not only a trans-impedance amplifier but also a limiting amplifier and a 50 Ω line driver. It can cope with leakage currents up to 1 mA, a current which is typical of highly damaged photodiodes due to high radiation doses. It exhibits a sensitivity of −19 dBm with a BER of 10^{-12}. As a natural consequence of the design and technology, this ASIC is also very resistant to SEUs.

The GigaBit Laser Driver

The GBLD is a radiation tolerant 5 Gb/s fully differential laser driver capable of providing a modulation current up to 24 mA and a maximum laser bias current of 43 mA with optional pre-emphasis to compensate for any external capacitive loads present in laser matching circuits. Such a wide modulation and bias current range is needed since the GBLD is designed to drive both edge-emitting lasers and VCSELs. These two laser types have very different driving characteristics, with the former type requiring high modulation and bias currents while the latter needs low bias and modulation currents.

The difficulty arising from the 130 nm CMOS technology used for all GBT chips is the maximum allowed voltage which is limited to 1.5 V. However, most lasers operate at voltages up to 2.5 V. To address this problem special transistors with a thicker oxide layer capable of 2.5 V are used in output stages while the rest of the GBLD internal circuitry is operated at 1.5 V. A drawback of these special transistors is their limited bandwidth.

1.3.3 Review of the radiation environment of HL-LHC detectors

The already high particle flux encountered at the LHC will be several times higher at the HL-LHC. The electrical and optical devices close to the interaction region will be exposed to a very harsh radiation environment resulting in displacement and ionization damage in their active volumes. Moreover, these parts of detectors will not be accessible during the operation of the HL-LHC, thus their reliability is of primary importance.

The radiation environment will be dominated by a pion flux with energies around 300 MeV and by spallation neutrons having energy ~ 1 MeV. Figure 1.7 shows the expected total fluence

as a function of radius of the CMS detector for an integrated luminosity of 500 fb^{-1} and 3000 fb^{-1} for the LHC and the HL-LHC, respectively. It can be seen that the expected total fluence at a distance of 20 cm from the interaction point, which is a typical tracker position, is of the order $10^{15}{}_{1\,MeV}$ neutrons/cm^2. It has been requested that the qualification level for the upgraded trackers should be $1.5 \times 10^{15}{}_{1\,MeV}$ neutrons/cm^2 [8].

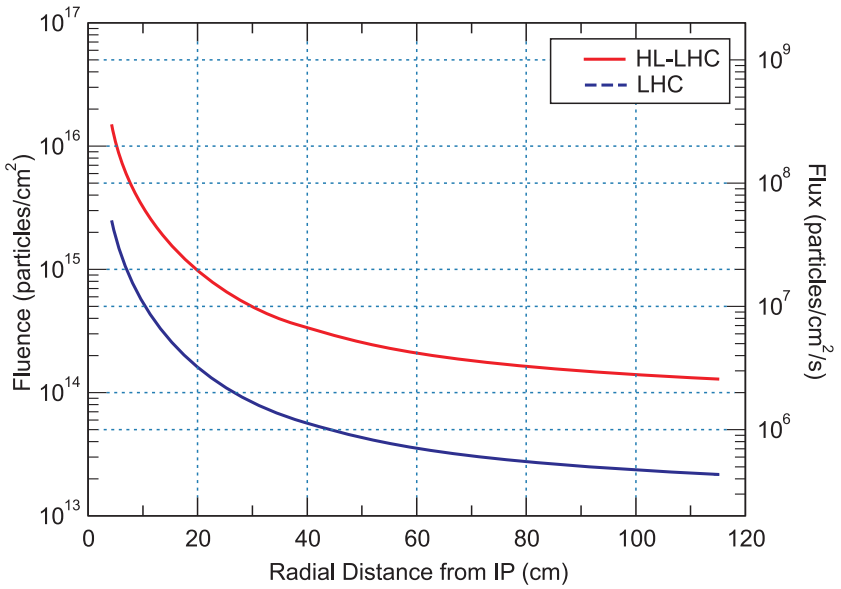

Figure 1.7: The expected CMS Si total flux and fluence for 500 fb^{-1} and 3000 fb^{-1} integrated luminosity as a function of radial distance from the interaction point (graph taken from Jan Troska).

Considering the six-times increase in total fluence foreseen at the HL-LHC, it is obvious that the current detectors used in the LHC experiments close to the interaction region will have to be replaced with upgraded ones able to withstand such a high particle flux. Therefore, trackers and parts of the forward calorimeters for the HL-LHC will be re-designed for an integrated luminosity of 3000 fb^{-1} [82].

1.4 Scope of the thesis

After the introductory chapter, which outlined the importance and main requirements of optical transmission links in HEP experiments and gave examples of current use and future projects in this field, there follow two theoretical chapters. These deal with semiconductor lasers and photodiodes in terms of their principles of operation and the impact of irradiation on their performance. The thesis is then focussed on the experimental part. The fourth chapter presents the results from irradiation tests of the candidate devices for Versatile Link. Along with results, newly developed models describing their degradation under irradiation as well as an annealing phase are presented. Chapter five acts as an intermezzo in which a method to simulate SEUs in photodiodes is introduced. The last chapter then sets the outcomes of the irradiation tests in the context of the requirements for HEP experiments. It provides suggested guidance about how to

use the models to predict the behaviour of optoelectronic components in the final application and how these predictions can be employed in the design stage of new optical links. Methods for online monitoring of laser performance in system are also proposed.

Chapter 2

Semiconductor lasers

The purpose of this chapter is to provide a basic understanding of the principles of the semiconductor lasers which further chapters will refer to. The basic operational principles of lasers are outlined and then described using rate-equations for both steady-state and small signal analysis. Finally, a review of radiation effects in semiconductor lasers is presented.

2.1 Operational principles of semiconductor laser diodes

In comparison with other types of lasers, semiconductor lasers are rather unique. They can operate with very low input power which also means that they can be very small and efficient. Their means of operation are also somewhat different. The lasing action in a semiconductor laser is initiated by the injection of carriers over the interface of different semiconductor materials. The layer in which gain is produced is called the *active layer* and is made of a direct band-gap material. Another special feature is that electrical carrier injection into a laser junction is used as the source of pumping energy for the laser.

The semiconductor material has to be excited, i.e. its thermal equilibrium has to be broken, in order for it to emit optical radiation. In semiconductor lasers this is achieved by injection of charge carriers across a semiconductor diode junction. These charge carriers (electrons and holes) recombine via *radiative transitions* to produce light. Competing non-radiative transitions are also possible, a typical example being *Auger transitions* where the energy is transferred to the crystal lattice in the form of phonons. It should be noted that the wavelength of emitted light depends on the type of semiconductor material, specifically the width of its band gap.

Further explanation requires the introduction of a *two-state quantum system*. Only three types of interaction between radiation and matter are possible in such a system as is depicted in Figure 2.1. Figure 2.1(a) shows *absorption*, where an incident photon transfers its energy to an electron which is excited from the valence band to the conduction band. An electron in the conduction band can de-excite to the valence band by emission of radiation of the same energy as the band-gap. This process is called *spontaneous emission of radiation* and is shown in Figure 2.1(b).

The third type of interaction is called *stimulated emission of radiation* (Figure 2.1(c)). In this process a photon reacts with an excited electron in the conduction band, causing it to de-excite to the valence band accompanied by the emission of a photon. The newly created photon is identical with the incident one: it has same direction of propagation; and the same wavelength, phase, and polarization as the stimulating one. The resulting radiation is thus *coherent* and light is amplified by this process. *Light-emitting diodes* (LED) operate on the principle of spontaneous radiation whereas laser diodes are based on the stimulated emission of radiation as the name implies.

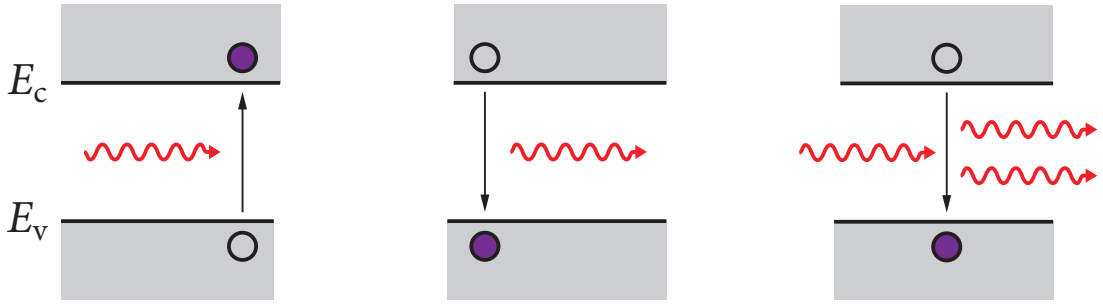

(a) absorption (b) spontaneous emission (c) stimulated emission

Figure 2.1: Three possible interactions between radiation and matter in two level quantum system.

Stimulated emission outweighs the competing spontaneous emission only when more electrons are present in the conduction band than in the valence band. This *population inversion* is the first condition of lasing and in semiconductor lasers is achieved by the application of a drive current to the semiconductor structure. Continuous current flow leads to continuous stimulated emission only if enough photons are constantly present in the active layer to trigger this process. The intensification of light is achieved by positive optical feedback and confinement of photons in an optical resonator. This is the second basic condition of lasing. The optical feedback is accomplished in a form of *Fabry-Pérot* resonator by a system of mirrors, either semitransparent – cleaved surfaces of laser die – or by distributed *Bragg mirrors* with high reflectivity. Optical mode confinement is typically achieved through dielectric waveguiding.

As already mentioned, semiconductor lasers are pumped by electrical current flowing across the junction region where the *n*-type material is joined with the *p*-type material. The current is produced by applying a voltage across the *pn* junction, thereby producing an electrical field that forces electrons from the *n*-type side to the *p*-type and holes in the reverse direction. Electrons and holes are attracted to each other and thus recombine. If the current is low, incoherent light is produced and the laser diode operates as an LED. By increasing the current flowing through the junction, more electrons are pumped into the conduction band and once the population inversion is achieved optical gain is produced. The current at which this occurs is called the laser *threshold current*. The dependence of laser light output on injection current is shown in Figure 2.2.

Laser threshold Although stimulated emission can occur as soon as a current flows through a laser junction, the laser does not emit coherent light until the current reaches the *threshold*

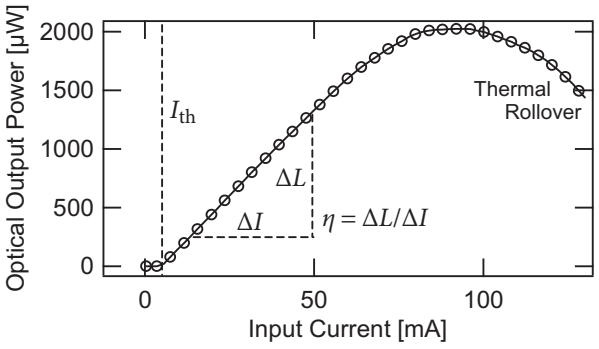

Figure 2.2: Typical *L-I* plot of an un-irradiated laser operated at room temperature.

current, denoted I_{th}. In other words, the laser oscillation condition is that the gain just exceeds the absorption loss. With a further increase in current, the active region of a semiconductor laser exhibits optical gain and the light passing through it is amplified. Spontaneously emitted photons serve as the noise input that triggers the amplification process. Typical values of threshold current are in the order of mA, smaller values indicating superior performance. Threshold current is minimized by maximizing internal quantum efficiency and by minimizing resonator losses.

Slope efficiency The slope efficiency is another performance parameter of a semiconductor laser. It is a measure of the percentage of electrons injected through the junction above the laser threshold that contributes photons to the emitted coherent light. Referring to Figure 2.2, the slope efficiency $\eta = \Delta L/\Delta I$ is the slope of the linear part of the *L-I* curve above threshold. This efficiency is restricted by carrier and photon losses inside the laser cavity.

The slope efficiency does not remain constant with increasing current – the output power saturates for large values of current and exhibits a *thermal rollover* as non-radiative transitions become more and more dominant. Three factors may contribute to this phenomenon. The first mechanism is junction heating that may reduce the charge carrier recombination time τ_e as the laser power increases. The decrease in τ_e is due to Auger recombination which is strongly temperature dependent. The second mechanism is the increase of internal losses with current so that fewer photons contribute to the output power. The final mechanism is the possible increase in leakage current, i.e. the current that flows outside the active region. With further increase of the driving current, the laser comes to a point at which it no longer lases and behaves like an LED.

Non-radiative recombination As already mentioned apart from the desired radiative recombination of electrons and holes in the semiconductor, these may also recombine non-radiatively. Non-radiative recombination processes include Auger recombination, recombination at defects and surface recombination. During the Auger recombination process the energy of the electron-hole pair is transferred to another electron which is subsequently excited. This electron then relaxes back to thermal equilibrium by losing its energy to phonons that dissipate in the crystal lattice. Defects in the active region of the semiconductor laser produce a continuum of quantum

states in the band-gap in localized regions of the material. Electron and holes that are in the vicinity of the defect state can recombine non-radiatively via that continuum of quantum states. Surface recombination may occur at the edges of active region or in the interface between the active and cladding layers. Generally, the surface represents a strong perturbation of the crystal lattice with a correspondingly high concentration of defects. It is these defects that can act as centres of non-radiative recombination.

2.1.1 Material systems

All semiconductor lasers are typically grown on four material types depending on the desired output wavelength. Three of these materials (GaAs, InP and GaN) are composed of atoms with three and five valence electrons and are denoted *III-V* compounds. The other one is a *II-VI* compound, ZnSe. These four different substrate materials preselect the operation wavelength range by defining which junction materials offer the best lattice match to them. Lasing wavelength is then determined by stoichiometry of the active region material. Various possible combinations of materials are in Figure 2.3.

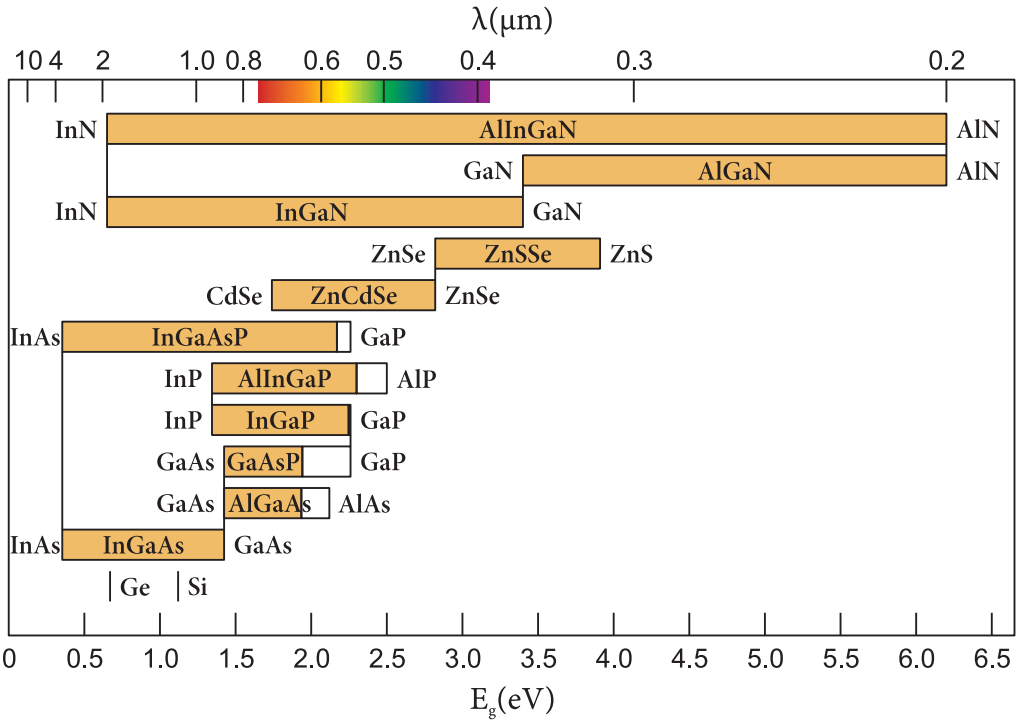

Figure 2.3: Bandgap energy E_g and corresponding wavelength λ for selected semiconductor compounds. Shaded regions represent compositions with a direct bandgap.

Gallium Arsenide based lasers This binary direct bandgap semiconductor was used to fabricate the first laser diode with the emission wavelength of 873 nm [75]. Lasers grown on this substrate operate in the red and near-infrared parts of spectrum from 635 nm up to 870 nm.

Adding aluminium to GaAs to create the ternary compound $Al_xGa_{1-x}As$ increases its bandgap. The emission wavelength can be compositionally tuned while preserving the lattice matching. Currently, compact disc (CD) players use a 780 nm AlGaAs laser. Short-haul (up to several hundred meters) high speed data transmission systems operating at 850 nm also use AlGaAs/GaAs lasers as drivers. Another lattice matched semiconductor compound that can be grown on GaAs is AlGaInP. This quaternary compound attains lattice matching only for compositions in the range $(Al_xGa_{1-x})_{0.5}In_{0.5}P$. One of the application of a 650 nm AlGaInP laser are digital video disc (DVD) players.

Indium Phosphide based lasers Long-haul high speed lasers generally operate in the vicinity of 1550 nm wavelength where the minimum loss in optical fibre occurs. These lasers use quaternary, compositionally tunable semiconductor $In_{1-x}Ga_xAs_{1-y}P_y$ grown on an InP substrate. Thanks to its ease of wavelength tuning, InGaAsP lasers also operate near 1310 nm, a wavelength where the minimum material dispersion occurs. The latter are used for short-haul communication systems.

Zinc Selenide based lasers These lasers with their derived alloys were the first semiconductor lasers operating in the blue and green portions of optical spectrum [77]. The active layer was mainly composed of ZnCdSe with ZnSSe as a cladding. With the introduction of gallium nitride-based lasers these lasers became obsolete mainly due to problems of long-term operation and reliability.

Gallium Nitride based lasers GaN is a recently developed direct band gap semiconductor alloy with a bandgap wavelength of 366 nm falling in the near-ultraviolet region of the spectrum. By addition of indium to GaN a ternary direct bandgap semiconductor $In_xGa_{1-x}N$ is produced that is tunable over a wavelength range from 366 nm to 580 nm, thus being complementary to AlGaInP lasers. The main application of these lasers is for Blue-ray Discs (BD) operating at 405 nm which falls in fact into the violet region of spectrum.

2.1.2 Laser structures

Semiconductor lasers are fabricated in variety of forms operating from the mid-ultraviolet to far-infrared portions of the spectrum and with output powers ranging from nW to kW in case of arrays of laser diodes. Semiconductor lasers can be of two types depending on the direction of light emission: *edge emitting lasers*; or *surface emitting lasers*.

Edge emitting lasers

These lasers typically use large Fabry-Pérot resonators with typical lengths $l \approx 500$ μm and widths $w \approx 2$ μm. They are often operated as multi-spatial mode devices suitable for high-power applications. However, they can be also operated with single spatial and longitudinal

modes. There are several general structures for edge emitting lasers using either traditional heterojunctions or quantum-well active regions with gain or index guided structures.

A simple *pn* junction or *homojunction* is convenient only as a source of incoherent light in LEDs. The practicality of homojunction lasers is significantly reduced by the large amount of heat dissipation which means in turn that they can be effectively operated only at temperatures well below room temperature or for very short periods of time.

Considerable improvement in the efficiency of lasers is achieved through the use of *heterojunctions*. Heterojunctions consist of several layers of various lattice-matched semiconductor materials. The active layer is fabricated from a direct bandgap material while the adjacent *cladding* layers can be of indirect bandgap material. The target of heterostructures is to squeeze the region of light emission to a smaller volume, thus reducing the heat dissipation and consequently improving the efficiency. Lasers with only one heterostructure are seldom used. More common are lasers with several heterostructures which prevent unwanted diffusion of charge carriers outside the active region and further stimulate the emission of radiation. This system of heterostructures combined with an optical resonator in the form of a block with cleaved facets is depicted in Figure 2.4.

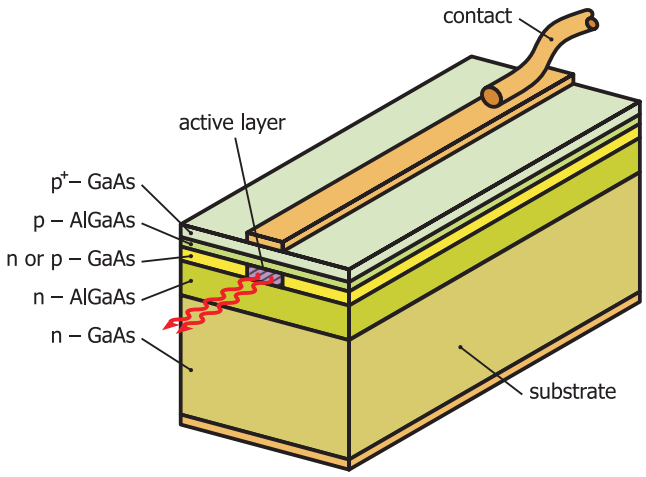

Figure 2.4: Edge-emitting GaAs semiconductor laser with double heterostructure.

Further improvement in laser efficiency, laser resistance and heat dissipation is achieved in quantum well lasers. The active layer of these lasers is squeezed to only a few nm creating step-function bands with discrete energies. The outcome of this reduction in size is a lower threshold current due to a higher electron concentration per unit volume and minimum heat dissipation since most of the heat is produced within the active region. The disadvantage of quantum well lasers is the low output power since the total number of charge carriers participating in radiative recombinations is reduced. This drop in power can be mitigated by stacking several quantum wells in parallel while still retaining the important confining features of the quantum well. Such devices are known as multiple quantum well lasers.

Two types of structure exist to confine the optical mode of the active region in the lateral direction. In the first case, referred to as *gain guiding*, the region where the gain is produced is limited in width. Alternatively, the optical beam can be confined by reflection at interfaces of

the active region by fabricating an index of refraction change into the laser. This is referred to as *index guiding*.

Gain-guided structures In this case, the confinement of the optical mode is achieved by current flow. When the current flows into the active region, it produces gain only in a narrow stripe determined by the metallic contact as shown in Figure 2.5. The disadvantage of this structure is that the effective width of the gain region broadens as the current density in the active layer increases.

Index-guided structures The other means of laser mode confinement in the lateral plane is fabricating cladding layers of a different material. Different materials have a different index of refraction, thus an index-guided structure is created provided that the index of refraction of the adjacent layer is lower than that of the active layer. Thus the laser operates in a waveguide mode determined by the width of the higher index material as shown in Figure 2.6.

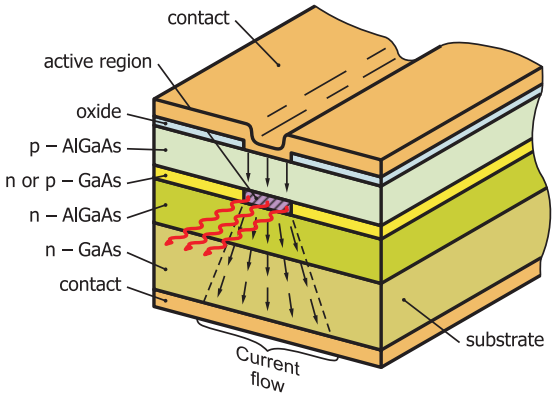

Figure 2.5: Gain guided GaAs laser structure.

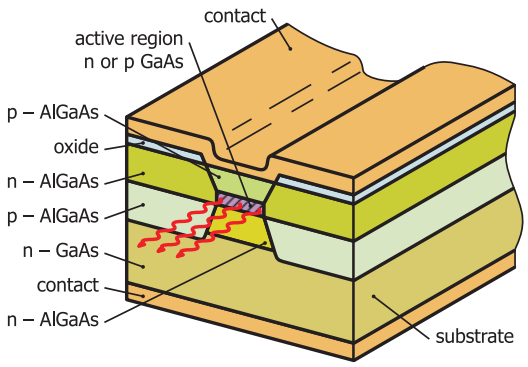

Figure 2.6: Index guided GaAs laser structure.

Surface emitting lasers

The disadvantage of edge-emitting lasers for some applications is that the emission of light is parallel to the surface of the wafer. For many applications requiring two-dimensional laser arrays it is desirable to have semiconductor lasers emitting in the direction normal to the axis of the laser gain medium. These lasers are commonly referred to as *surface emitting lasers* (SELs). They can be of two different structures. The first one is a laser with a distributed grating coupler known as a *grating coupler surface emitting laser* (GSEL). The grating redirects a portion of light out of the cavity in the direction normal to the gain axis of the laser. The other structure has a cavity perpendicular to the semiconductor substrate with mirrors fabricated at the ends of active region. These lasers are referred to as *vertical cavity surface emitting lasers* (VCSELs).

Since the thickness of the active region typically made up of multiquantum wells is very small (only a few nm), the single pass gain is minimal – usually a fraction of 1 %. High gain and high mirror reflectivities > 99 % are thus mandatory to ensure that cavity losses are smaller

than the gain available from a single pass. The high reflectivity is provided by *distributed Bragg reflectors* (DBRs). These mirrors have two alternating layers with a high refractive index ratio and quarter-wavelength thickness. The reflected waves from all layers add up constructively, allowing for DBR reflectances above 99 %.

A VCSEL emitting at 850 nm is shown schematically in Figure 2.7. It is a laser grown on a GaAs substrate with alternating layers of *n*-AlGaAs to form a *n*-DBR with a GaAs active region surrounded by AlGaAs cladding followed by a *p*-AlGaAs DBR. The number of pairs needed to fabricate a high reflectivity DBR depends on the refractive index ratio of layers of a pair. For a higher index ratio fewer pairs are needed.

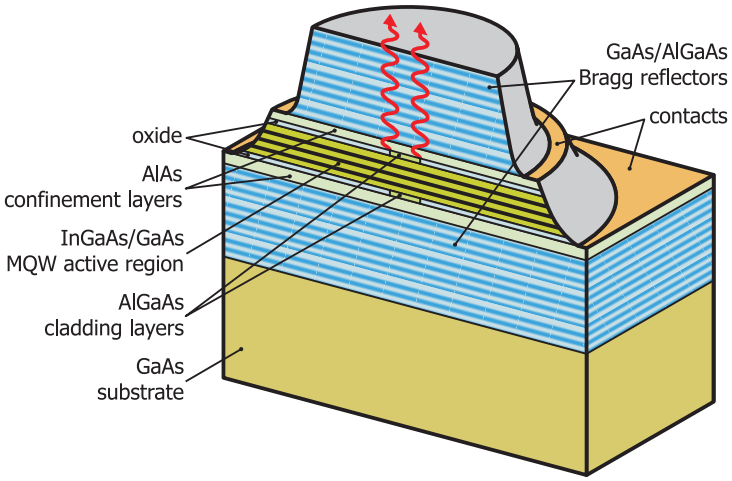

Figure 2.7: Schematic diagram of a multiquantum well GaAs/InGaAs VCSEL.

VCSELs typically have a low threshold current and high efficiency resulting in low power consumption and, in contrast with edge emitters, exhibit a circular beam output. Because VCSELs are microresonator lasers, they yield very large longitudinal mode spacing, thereby only one mode can fall into the gain bandwidth of the laser.

The range of operation of VCSELs stretches from the visible to the near-infrared portions of the spectrum. They are fabricated with a broad range of diameters, the smallest being ≈ 1 µm. Common VCSELs are operated at wavelengths of 780 nm for use in CD players, 850 nm in local optical communication networks, as well as 1.3 µm and 1.55 µm in high-speed long distance optical links.

In contrast to short-wavelength GaAs VCSELs, the performance of InP-based devices is limited by the disadvantageous properties of the InGaAsP material system. This is demonstrated mainly in DBRs where the InGaAsP/InP system exhibits only a small variation in refractive indices. To obtain high mirror reflectances, a large number of layers must be grown which in turn cause significant diffraction losses. InGaAsP is also a material with low thermal conductivity which causes excessive temperature increase in the active region during laser operation. One of the concepts that overcomes these limitations is the utilization of InP/GaAs wafer bonding where DBRs in long wavelength VCSELs are replaced by superior GaAs based mirrors. The advantage of GaAs is also its transparency for longer wavelengths which offers an option to extract light through the substrate.

2.1.3 Output spectra

The output spectrum of a semiconductor laser is governed by several factors. It depends on the bandwidth of the active region where the gain is larger than losses; on the allowed longitudinal modes which are determined by the geometry and material of the optical resonator; and on factors like *spatial-hole burning* [78]. These effects are illustrated in Figure 2.8. A surprising feature of semiconductor lasers is the fact that although the gain profile is *homogeneously broadened* [98], more longitudinal modes appear in the output spectrum carrying a significant amount of optical power even at high currents above threshold.

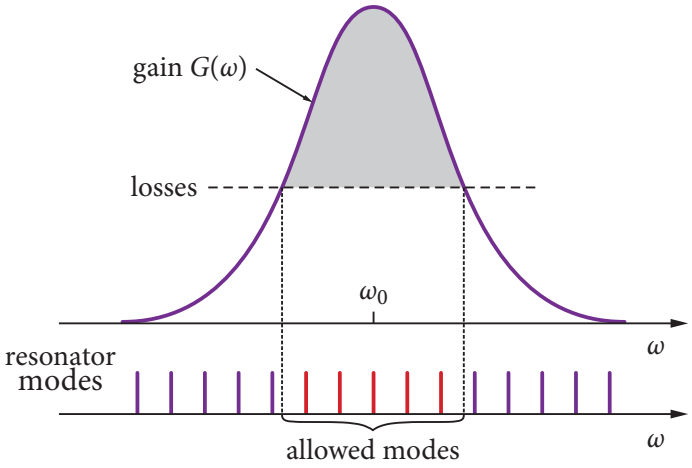

Figure 2.8: Illustration of dependence of allowed longitudinal modes on gain spectrum and resonator modes. Laser oscillation can occur only at frequencies for which the gain is grater than losses, i.e. in a shaded area.

The mechanism that largely contributes to the multi mode behaviour of semiconductor laser is the spontaneous emission which is acting as a noise source triggering all the allowed modes for which the round trip gain between mirrors is greater than losses. Over the threshold the modes that are closest to the central frequency of the medium gain envelope grow faster than side modes which saturate. With increasing current, side modes lose power as the gain is reduced while the more central modes continue to grow, albeit at a slower rate. This is demonstrated in Figure 2.9 where the spectra are shown for various output powers.

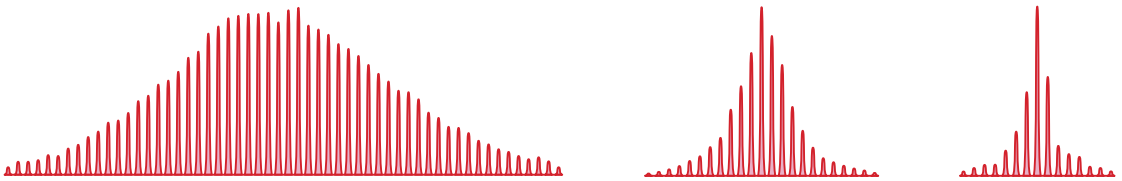

(a) $P_0 = 0.82$ mW (b) $P_0 = 4.6$ mW (c) $P_0 = 11.7$ mW

Figure 2.9: Normalized longitudinal mode spectra of a gain guided laser at three different power levels.

The physical process that allows more longitudinal modes within a single laser cavity is spatial-hole burning. This process is particularly prevalent in short cavities, like those found in

semiconductor lasers, where standing waves are present. Once a standing wave pattern develops within the laser cavity, the light intensity is zero at the cavity mirrors and at every half-wavelength interval between mirrors. No stimulated emission occurs at these null points, therefore different longitudinal modes can use this otherwise wasted gain.

2.2 Rate-equation model of semiconductor laser operation

The rate-equations provide a description of a semiconductor laser in terms of static, spectral and dynamic characteristics and their dependence on various parameters. They describe the interplay between photons and charge carriers inside the laser cavity.

For a uniform electron density n in the conduction band of the active region of a semiconductor laser, the single-mode rate-equation can be written as [6, 74]:

$$\frac{\mathrm{d}n}{\mathrm{d}t} = \frac{I}{qV} - \gamma_e n - GP \tag{2.1}$$

$$\frac{\mathrm{d}P}{\mathrm{d}t} = (GV - \gamma)P + R_{\mathrm{sp}}, \tag{2.2}$$

where I is the current, q the elementary charge, P the photon number within the cavity, V the volume of the active region, G is the gain per unit time and volume, R_{sp} is the spontaneous emission term and γ_e and γ are the decay rates of electrons and photons, respectively. Equations (2.1) and (2.2) apply only to single mode operation of the laser or to the operation with a limited number of modes with relatively similar properties. In the multi-mode case, the rate-equations take the form:

$$\frac{\mathrm{d}n}{\mathrm{d}t} = \frac{I}{qV} - \gamma_e n - \sum_m G_m P_m \tag{2.3}$$

$$\frac{\mathrm{d}P_m}{\mathrm{d}t} = (G_m V - \gamma)P_m + R_{\mathrm{sp}}(\omega_m), \tag{2.4}$$

where $G_m = G(\omega_m)$ is the mode gain. Equations (2.1) and (2.2) can be also used for multi-mode operation to some extent. In that case P represents the summation over the photon numbers of individual modes, and G and R_{sp} are a weighted average depending on the mode intensity.

2.2.1 Steady-state characteristics

The steady state solution of the rate-equations can be used to obtain the response of a laser for continuous-wave operation. This is beneficial to characterize laser performance by two main characteristics, the light-current curve and the longitudinal mode spectrum.

Light-current curve

Assuming steady state operation, i.e. setting all time derivatives to zero, and expressing R_{sp} as:

$$R_{\mathrm{sp}} = \beta_{\mathrm{sp}} \gamma_e V n, \tag{2.5}$$

where β_{sp} is a fraction of photons spontaneously emitted into the lasing mode, the rate-equations (2.1) and (2.2) may be rewritten as:

$$J - \gamma_e n - G(n)P = 0 \tag{2.6}$$

$$P\big(G(n) - \gamma/V\big) + \beta_{sp}\gamma_e n = 0. \tag{2.7}$$

The term $J = I/qV$, which is proportional to the drive current, can be regarded as a pumping term. To compute the equations, the explicit form of the gain G must be known [6,16,74,78,96,97]. In the simplest case, it can be expressed as $G(n) = kn$, where k is a constant.

In order to be able to solve equations (2.6) and (2.7) numerically, the constant factors (which can differ by several tens of orders of magnitude) should be eliminated. Thus, the following dimensionless quantities are introduced:

$$N = n/n_{th}, \qquad j = \frac{J}{J_{th}}, \qquad p = \frac{\gamma P}{J_{th}V}, \tag{2.8}$$

where the subscript 'th' denotes the quantities at threshold. The relationship between threshold current J_{th} and the electron density at threshold n_{th} is obtained from equation (2.6), where the photon number P is substituted from equation (2.7). It is customary to neglect spontaneous emission when defining J_{th} [6,74]. Setting $\beta_{sp} = 0$, we obtain:

$$J_{th} = \gamma_e n_{th}. \tag{2.9}$$

The electron density at threshold n_{th} is calculated from the condition

$$G(n_{th}) = \gamma/V. \tag{2.10}$$

Taking these definitions into account and expressing the gain constant k from condition (2.10) as:

$$k = \frac{\gamma}{Vn_{th}}, \tag{2.11}$$

the rate-equations may be written in a normalized form as:

$$j - N - pN = 0 \tag{2.12}$$

$$p(N-1) + \beta_{sp}N = 0. \tag{2.13}$$

If spontaneous emission is neglected, the solution of the equations (2.12) and (2.13) below threshold is:

$$N = j \tag{2.14}$$

$$p = 0, \tag{2.15}$$

and above threshold:

$$N = 1 \tag{2.16}$$

$$p = j - 1. \tag{2.17}$$

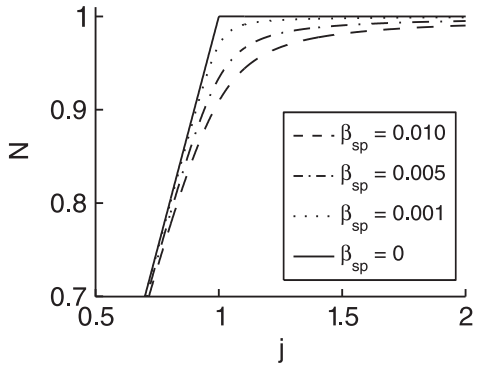

Figure 2.10: The normalized electron density N as a function of normalized drive current j for different values of spontaneous emission factor β_{sp}.

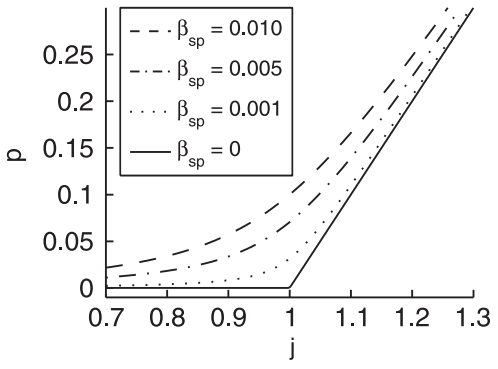

Figure 2.11: The normalized photon number within the laser cavity p as a function of normalized drive current j for different values of spontaneous emission factor β_{sp}.

If spontaneous emission is taken into account, the numerical solution of N and p depending on j for different values of β_{sp} is shown in Figures 2.10 and 2.11, respectively.

From these plots is evident that the parameter β_{sp} governs the shape of curves near the threshold region where spontaneous emission is significant.

The drawback of these simple rate-equations is their linearity in the region above threshold. In their simplest form, they do not model thermal rollover for high injection currents. A commonly used approach to model thermal rollover is the modification of the gain term G by introducing a *gain suppression factor* ε. At high photon densities, the gain is reduced by a factor $1/(1+\varepsilon P)$ [15] or $1/\sqrt{1+\varepsilon P}$ [4]. The gain can be then written as:

$$G(n,P) = \frac{G(n)}{1+\varepsilon P}. \tag{2.18}$$

The explicit form of $G(n)$ is varied according to application as in the case of equations (2.1) and (2.2). The resulting *L-I* curve exhibits a quadratic behaviour above threshold.

In order to further improve the shape of *L-I* curve, other factors such as leakage current or temperature dependence are incorporated into the rate-equations as in [61, 62]. In both cases, higher order polynomials are used for this purpose. Even though the description of *L-I* curves is more accurate, an obvious disadvantage is the enormous number of free parameters. A completely different approach to describe laser behaviour is to use complex semiconductor laser simulators [46, 55, 68, 76].

Longitudinal mode spectrum

Multi-mode rate-equations can be also used to obtain the laser output spectrum. With the help of equations (2.1) and (2.2) the relative intensities of individual modes can be calculated. In order to solve these equations the gain spectrum $G_m = G(\omega_m)$ has to be known. A simple

approximation is that the gain decreases quadratically from its peak value. According to [6] the modal gain can be expressed as:

$$G_m = G_0 \left[1 - (m/M)^2\right], \tag{2.19}$$

where M is the number of highest mode, i.e. $2M+1$ represents the total number of longitudinal modes with positive gain. It is determined by:

$$M = \left\lfloor \frac{\Delta\omega_g}{\Delta\omega_L} \right\rfloor, \tag{2.20}$$

where $\Delta\omega_g$ is the frequency spread over which the gain is non-zero and $\Delta\omega_L$ is the longitudinal mode spacing, see Figure 2.12.

This approximation assumes that the central most intense mode is located at the peak gain frequency ω_0 and is mainly applicable to index guided lasers which exhibit a rather small number of longitudinal modes. The photon number P_m of an individual mode is obtained from equation (2.2) as:

$$P_m = \frac{R_{\mathrm{sp}}(\omega_m)}{\gamma - VG_m}, \tag{2.21}$$

with the assumption that all modes have the same loss γ.

Expressing G_0 as $G_0 = kn$ and denoting $g_m = 1 - (m/M)^2$ one can follow the same normalization procedure as for the single-mode case. The resulting normalized multi-mode equations can be written as:

$$j - N - N \sum_{m=-M}^{M} g_m p_m = 0 \tag{2.22}$$

$$p_m(Ng_m - 1) + \beta_{\mathrm{sp}} N = 0, \tag{2.23}$$

with the assumption that $R_{\mathrm{sp}}(\omega_m)$ can be replaced by $R_{\mathrm{sp}}(\omega_0)$. This is justified by the fact that the spontaneous emission spectrum is much larger than the longitudinal mode one.

Calculated *L-I* curves for the multi mode case with $M = 10$ are shown in Figure 2.13. It can clearly be seen that the multi-mode rate-equations describe the saturation of side longitudinal modes well. The level of saturation of side modes is proportional to the value of β_{sp}. The normalized multi-mode spectra calculated for three different values of current are shown in Figure 2.14. As can be seen, the spectrum is symmetric which is in accordance with the assumption that the gain spectrum (2.19) is symmetric. In reality, both the gain and longitudinal mode spectra show some level of asymmetry.

2.2.2 Small-signal analysis

This subsection describes the dynamic characteristics of a semiconductor laser using rate-equations. In contrast to the previous steady state case, small signal analysis investigates the transient response of a semiconductor laser before it reaches a steady state.

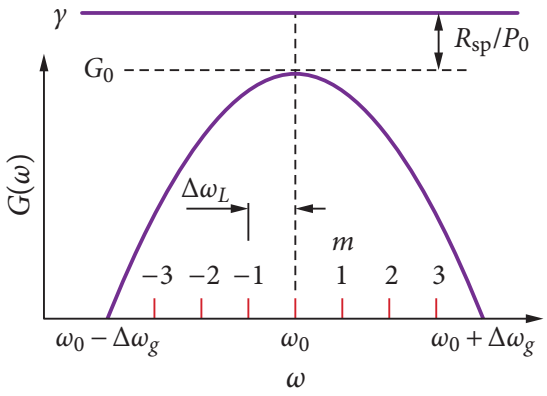

Figure 2.12: Quadratic gain spectrum with a schematic illustration of longitudinal modes.

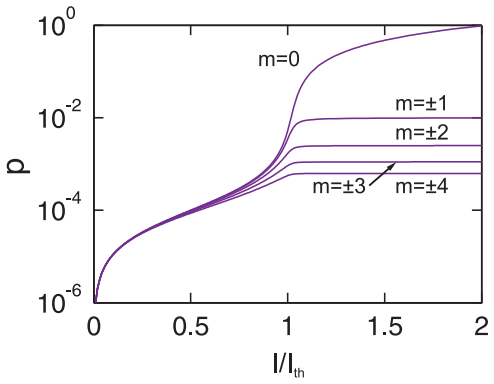

Figure 2.13: Calculated normalized photon number as a function of normalized current for the first 9 longitudinal modes ($\beta_{sp} = 10^{-4}$).

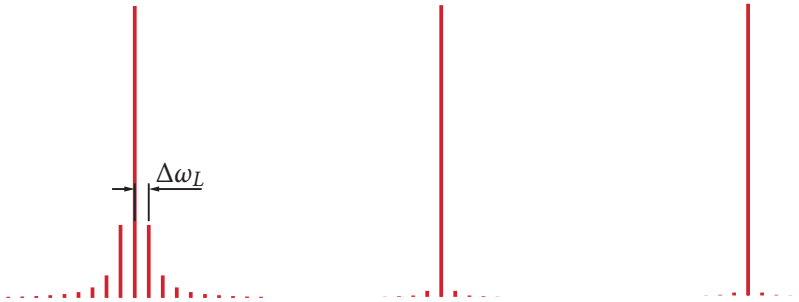

(a) $I/I_{th} = 1.1$ (b) $I/I_{th} = 1.5$ (c) $I/I_{th} = 2.0$

Figure 2.14: Calculated longitudinal mode spectra at three different drive current levels.

Relaxation oscillations

When changing the laser operation from one steady-state to another, the laser passes through a transient state in which the output exhibits damped periodic oscillations. These *relaxation oscillations* are due to the intrinsic resonance of the nonlinear laser system. The frequency and damping rate of these oscillations can be obtained by small-signal analysis of the single-mode rate equations (2.1) and (2.2).

In a small-signal analysis, the steady state quantities P and n are perturbed by a small amount δP and δn, i.e.:

$$n(t) = n + \delta n \tag{2.24}$$

$$P(t) = P + \delta P. \tag{2.25}$$

The solution for δP and δn can be found from linearised rate equations of δP and δn:

$$\frac{\mathrm{d}(\delta n)}{\mathrm{d}t} = -\Gamma_n \delta n - \left(G + P\frac{\partial G}{\partial P}\right)\delta P \tag{2.26}$$

$$\frac{\mathrm{d}(\delta P)}{\mathrm{d}t} = -\Gamma_P \delta P + \left(PV\frac{\partial G}{\partial n} + \frac{\partial R_{sp}}{\partial n}\right)\delta n, \tag{2.27}$$

where

$$\Gamma_n = \gamma_e + n\frac{\partial \gamma_e}{\partial n} + P\frac{\partial G}{\partial n} \tag{2.28}$$

$$\Gamma_P = \gamma - GV - PV\frac{\partial G}{\partial P} \tag{2.29}$$

are the decay rates of fluctuations in the photon populations and carrier density, respectively. The solution of this eigenvalue problem is in exponential form:

$$\delta n(t) = \delta n_0 \, \mathrm{e}^{-(\gamma_r \pm \mathrm{j}\omega_r)t} \tag{2.30}$$

$$\delta P(t) = \delta P_0 \, \mathrm{e}^{-(\gamma_r \pm \mathrm{j}\omega_r)t}, \tag{2.31}$$

where δn_0 and δP_0 are the initial values of perturbation,

$$\gamma_r = \frac{1}{2}(\Gamma_n + \Gamma_P) \tag{2.32}$$

is the damping rate of relaxation oscillations and ω_r, the relaxation oscillation angular frequency, can be approximated as [6]:

$$\omega_r \approx \sqrt{GPV\frac{\partial G}{\partial n}}. \tag{2.33}$$

Assuming linear gain as in steady state case and using the expressions (2.9–2.11) , the relaxation oscillation quantities γ_r and ω_r can be further simplified as:

$$\gamma_r = \gamma_e \left(\frac{I}{I_{\mathrm{th}}}\right) \tag{2.34}$$

$$\omega_r = \sqrt{\gamma\gamma_e \left(\frac{I}{I_{\mathrm{th}}} - 1\right)}, \tag{2.35}$$

under the assumption that $n = n_{\mathrm{th}}$ for $I \geq I_{\mathrm{th}}$.

Intensity noise

Until this point, quantities P and n were assumed to remain stable once the steady-state was reached. In reality laser output exhibits intensity and phase fluctuations due to the quantum nature of the lasing process. The phase fluctuations are responsible for spectral broadening of longitudinal modes, i.e. for the width of observed spectral lines. The intensity noise, which can limit system performance of optical communication systems if it is too high, reaches its maximum around threshold and then decreases rapidly with an increase in the drive current. The spectrum of the intensity noise exhibits a peak near the relaxation oscillation frequency. This noise is characterized by the *relative intensity noise* (RIN). RIN can be used to determine the resonance frequency, the intrinsic bandwidth and the damping factor of lasers. It can be calculated as:

$$\mathrm{RIN} = \frac{\left\langle \delta P(t)^2 \right\rangle}{\langle P(t) \rangle^2}, \tag{2.36}$$

where the time average $\langle \delta P(t)^2 \rangle$ arises from the autocorelation function $\langle \delta P(t)\delta P(t+\tau)\rangle$ evaluated at zero. The term $\delta P(t)$ can be calculated from the modified set of equations (2.26) and (2.27) to which Langevin noise sources $F_n(t)$ and $F_P(t)$ are added [6].

The RIN can be represented in the frequency domain by the definition of the RIN spectral density by means of a Fourier transform:

$$\mathrm{RIN}(\omega) = \frac{S_P(\omega)}{\langle P(t)\rangle^2}, \tag{2.37}$$

where the spectral density $S_P(\omega)$ of the random process $\delta P(t)$ is defined as:

$$S_P(\omega) = \int_{-\infty}^{\infty} \langle \delta P(t)\delta P(t+\tau)\rangle \, \mathrm{e}^{-\mathrm{j}\omega\tau} \, \mathrm{d}\tau. \tag{2.38}$$

With a known spectral density $S_P(\omega)$, the RIN can be expressed as [6]:

$$\mathrm{RIN}(\omega) = \frac{2R_{\mathrm{sp}}\left[\Gamma_n^2 + \omega^2 + P^2\left(\frac{\partial G}{\partial n}\right)^2(1+\gamma_e n/R_{\mathrm{sp}}P) - 2\Gamma_n P\frac{\partial G}{\partial n}\right]}{P\left[(\omega_r-\omega)^2+\gamma_r^2\right]\left[(\omega_r+\omega)^2+\gamma_r^2\right]}. \tag{2.39}$$

This expression allows to evaluate the relaxation oscillation quantities from the measured spectral curve. Using the equations (2.34) and (2.35) electron and photon decay rates of the laser under test can be calculated. The experimental attempt to measure the RIN is described in section 4.6.

2.3 Radiation effects in semiconductor lasers

A study of radiation effects in semiconductor lasers became relevant as soon as the first lasers were released for military and space industry use. Early experiments were performed on a GaAs edge-emitting laser diodes irradiated by gamma and neutrons [11, 12]. Lasers were irradiated up to a relatively low – from present point of view – fluences of 10^{14} n/cm^2. Nevertheless, these fluences were high enough to observe phenomena like changes in a laser threshold and annealing after irradiation. Later works then report on laser behaviour with fluences up to 10^{15} n/cm^2 [20].

Semiconductor lasers were extensively tested in the past to qualify components for use in the CMS Tracker Optical Readout and Control Links at LHC. Irradiation tests of candidate optoelectronic devices for use in the CMS Tracker were performed by K. Gill et al. in the period 1997–2005 [36–40, 42]. In 2004, the first high fluence irradiation tests of the devices used in the current CMS optical links were made by M. Axer et al. [10]. In this high fluence irradiation test, the lasers were damaged to the point where they were no longer emitting coherent light.

The radiation damage effects observed in semiconductor lasers are caused by displacement and/or ionization. Of the two, it has been found that the effects of displacement damage are much more important for the fluences and doses typical of LHC [36]. Displacement damage occurs in a

material when an incident particle collides with one of the atoms and transfers sufficient energy to it in order to displace it from the original lattice position. If the energy transferred is large enough then the atom can produce further atomic displacements along its trajectory as it comes to rest. Defects known as vacancies and interstitials, which may introduce new energy levels in the band gap, can thus be created in semiconductor materials. These extra energy states act as generation-recombination centres which reduce the efficiency of band-to-band transitions. In lasers, recombination at these defects competes with radiative transitions, resulting in higher threshold current and lower light output efficiency.

2.3.1 Irradiation and annealing

Figure 2.15 illustrates the change of the *L-I* characteristics during neutron irradiation. The device under test (DUT) was an edge-emitting laser used in current CMS optical link generation. As the total fluence increases, both the shift of the threshold current and the loss in efficiency are evident. For higher fluences, the thermal rollover is more visible. The extracted parameters of threshold current and relative efficiency plotted versus the fluence for two irradiated devices are shown in Figure 2.16.

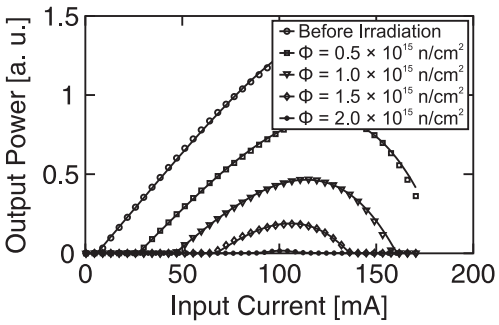

Figure 2.15: Set of typical *L-I* characteristics of a laser measured at different neutron fluences.

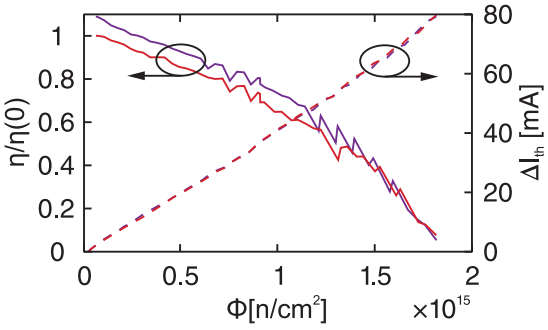

Figure 2.16: Measured threshold current increase ΔI_{th} and relative efficiency η_{rel} versus neutron fluence for two lasers of the same type.

Lasers anneal after irradiation and can recover a significant part of radiation-induced damage [36]. Figure 2.17 illustrates the annealing of an irradiated laser over a period of 200 hours, which is similar to Figure 2.15 with power on a log scale. This result indicates that the radiation-induced damage is flux dependent and that there would be less damage if the same fluence were accumulated over a longer irradiation period. A short-term irradiation test carried out on a timescale of tens of hours thus produces more damage in absolute terms than what would be expected in the final application where the flux is lower.

2.3.2 Non-Ionizing Energy Loss hypothesis for source equivalence

The *Non-Ionizing Energy Loss* (NIEL) is a quantity that describes the amount of energy transferred by an incident particle to a target material by atomic displacements. The concept of the NIEL

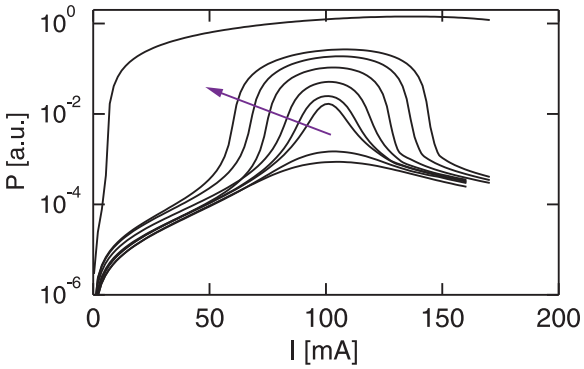

Figure 2.17: Measured *L-I* characteristics after irradiation. The arrow indicates the time evolution of annealing. For reference, the *L-I* curve obtained before irradiation is also included.

is widely used when comparing displacement damage effects in semiconductor devices. It has been successfully demonstrated that the deposited NIEL is linearly proportional to the degradation of semiconductor materials not only at the LHC [49] but also for high-temperature superconductors [93] or solar cells [64, 80, 92].

In optoelectronic devices radiation damage caused by displacement typically has a greater impact on device operation than that caused by direct ionization. This is confirmed by the observation that irradiation by ^{60}Co gammas up to a dose of 100 kGy has no significant impact on device operation [36, 87]. The differences in radiation damage to lasers caused by different hadronic sources are expected to scale with NIEL of interacting particles in the device material [38]. The NIEL fraction of the recoil energy is larger for heavier atoms for a given recoil energy. As an example, the maximum NIEL of a recoiled Si atom in Si bulk is found to be ~ 200 keV, compared to a value of ~ 2 MeV for In in InGaAsP compound which is a typical material of 1310 nm lasers.

As a further example, 1 MeV neutrons can cause a recoil of a Si atom in silicon up to an energy of 130 keV of which 100 keV is deposited as NIEL, i.e. already close to the maximum limit. However, in the case of InGaAsP, the maximum recoil energy from 1 MeV neutrons of a Ga atom is ~ 60 keV, of which 40 keV is typically dissipated in further atomic displacements. Since the NIEL part of the energy dissipated by recoiling atoms in InGaAsP can reach up to several MeV, it is clear that particles of higher energy will generate more damage per recoiling atom than a 1 MeV neutron, in contrast to the situation in silicon devices.

Despite the general acceptance of the NIEL approach, there are still problems that prevent its use in many applications. First of all, it is the limited number of materials and related compounds for which the NIEL is known. For illustration, the calculation of NIEL in ternary and quaternary semiconductor compounds is complex and is further complicated by the need to obtain the precise stoichiometry of the materials used from manufacturers. Due to this lack of data for radiation hardness scaling of complex compounds of optoelectronic devices, these have to be tested in various radiation sources. The testing is mainly performed in irradiation facilities using an intense and well-characterised beam of particles or ions which serve as proxy particles for the final operational environment.

Chapter 3

Photodetectors

Basic operational principles of photodetectors are introduced in this chapter together with a description of their typical material systems. Radiation effects in photodiodes and their subsequent annealing are explained with a brief discussion of single event effects.

3.1 Operational principles of photodetectors for high-speed data transmission systems

Semiconductor photodetectors are based on absorption of light by matter by the *photoelectric effect* [28], where impinging photons react with matter and create electron-hole pairs in the semiconductor material. If these pairs are created within a carrier diffusion length of the *pn* junction of the photodetector they can reach the depletion region where they are separated by the built-in electric field. This creates an additional current produced by the illumination which breaks the thermoelectric equilibrium of the *pn* junction. A *photo-electromotive force* which reduces the potential barrier of the junction is created. This internal voltage produces a current which is proportional to the intensity of illumination.

An ideal diode is described by the *Shockley equation*. The increase in reverse current i as a function of the intensity of illumination can be described as:

$$i = I_0 \left(\mathrm{e}^{\frac{qV}{kT}} - 1 \right) - i_f, \tag{3.1}$$

where I_0 is the saturation current, q is the elementary charge, k is the Boltzmann constant, T is the temperature, V is the voltage across the diode and i_f is the photocurrent proportional to the radiant flux. The constant of proportionality is called *responsivity*, i.e. the photocurrent generated by unit light power of incident monochromatic light. The current of a photodiode is thus composed of two components, a current of a classical semiconductor diode given by the Shockley equation and a component proportional to incident light. A typical I-V characteristics with operating conditions of a generic photodiode are depicted in Figure 3.1. The output voltage lies on the dashed line and is proportional to the photodiode illumination.

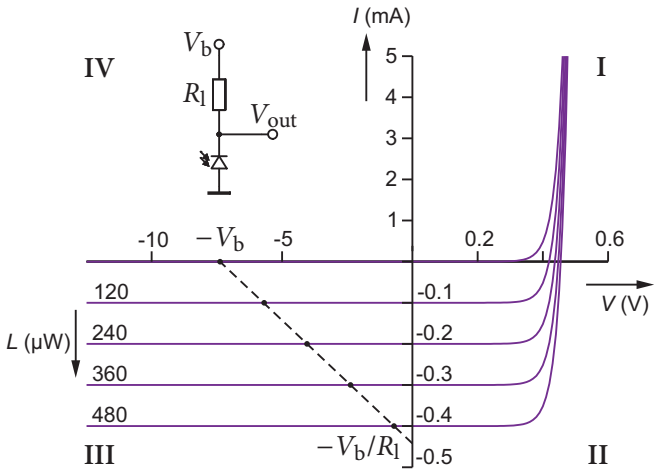

Figure 3.1: *I-V* characteristics of a photodiode with reverse bias operating conditions. Voltage and current on circuit schematic have negative signs with respect to the photodiode *I-V* curves, i.e. quantities V_b and V_{out} are negative on the plot.

The *I-V* characteristics (Figure 3.1) of a photodiode are most dense in the first quadrant (I in Figure 3.1) where a photodiode is least sensitive to incident light. This quadrant is not used for photodiode operation. If a photodiode is operated in the second quadrant, called *photovoltaic mode*, it behaves as a source of energy. The energy of radiation is directly transferred to electricity. Diodes operated in this regime are mostly used as *solar cells*. Good linearity is achieved only with relatively small load resistances.

The operating characteristics are parallel and almost equidistant in the third quadrant. If the bias point is set in this quadrant, it is operated in *photoconductive mode*. Photodiodes used for the detection of optical signals are solely operated in the third quadrant. This region offers the highest sensitivity to incident optical radiation and the most linear transfer characteristics.

Generally, photodiodes are very sensitive to optical radiation, they exhibit very low *leakage current* – the current which flows through the photodiode in the absence of light – but are susceptible to damage at high loads. However, they are very sensitive to humidity, thus good packaging is very important for long-term reliability.

The high-frequency properties of a photodiode are given on the one hand by its capacitance and on the other by the diffusion time of generated charge carriers, i.e. the time taken for generated carriers to reach the depletion region where they are separated. The speed of a photodiode can be improved by optimizing the doping profile. The principle behind it is that an inner electrical field which accelerates minority charge carriers to the photodiode potential barrier is present in regions of inhomogeneous dopant concentration.

3.1.1 Material systems

Semiconductor photodiodes are fabricated in similar material systems to those used for semiconductor lasers that were described in Chapter 2. As for lasers, the choice of photodiode material determines many of their properties. These are chiefly the optical wavelength range to which the photodiode responds and the level of noise. The wavelength sensitivity is determined by the photoelectric effect where only photons with sufficient energy can excite electrons across the bandgap of the material. Photons with lower energy do not react with the photodiode material and the material is transparent to them. Noise is also related to the width of the bandgap, where generally speaking materials with larger bandgap exhibit lower noise.

Conversely to the case of lasers, photodiodes can be fabricated from indirect bandgap material. Energy and momentum conservation are achieved by means of a two-step process. An absorbed photon first excites an electron to a high energy level within the conduction band. The excited electron and its associated hole then quickly relax to the lowest and highest possible levels in the conduction and valence bands, respectively. Since these processes are sequential, they are not unlikely. Typical photodiode materials can thus be both elemental and compound semiconductors. Si and Ge photodiodes belong among the photodiodes made from elemental semiconductors. Silicon photodiodes find their use in the range of wavelength from 800 to 900 nm while germanium photodiodes are best around 1400 to 1500 nm. While silicon photodiodes are still widely used, germanium photodiodes are being replaced by compound semiconductor materials mainly due to their intrinsically high dark current and slow speed caused by their large parasitic capacitance. Photodiodes fabricated from compound semiconductors are typically InGaAs and GaAs photodiodes. Even though they are more expensive their advantage is higher speed, higher efficiency and very low dark current. InGaAs photodiodes are typically used for wavelengths between 1300–1600 nm and GaAs photodiodes in the range 700–860 nm. A plot of responsivity versus wavelength for the materials previously mentioned is in Figure 3.2.

Similarly to lasers, photodiode structures can either be fabricated from a single material or use heterostructures. The advantage of heterojunctions is the possibility of using a larger bandgap material which can make use of its transparency to minimize optical absorption outside the depletion region and thus increase the efficiency. Heterostructures also offer the additional flexibility that light can be received from the substrate side, provided that the substrate is transparent to the incident light. The drawback is that photodiodes with heterostructures are fabricated using a less standard process which is reflected in their higher price. Common photodiode heterojunctions are AlGaAs/GaAs and InGaAs/InP.

3.1.2 p-i-n photodiodes

The high-frequency response of a photodiode can be improved by inserting an intrinsic region between *p* and *n* regions so that a *p-i-n photodiode* is created. These p-i-n photodiodes are constructed in a way that most of the optical radiation is absorbed in an intrinsic region which has about six to seven orders of magnitude higher resistivity than neighbouring regions. A relatively high electrostatic field is present in the intrinsic region, which accelerates the charge

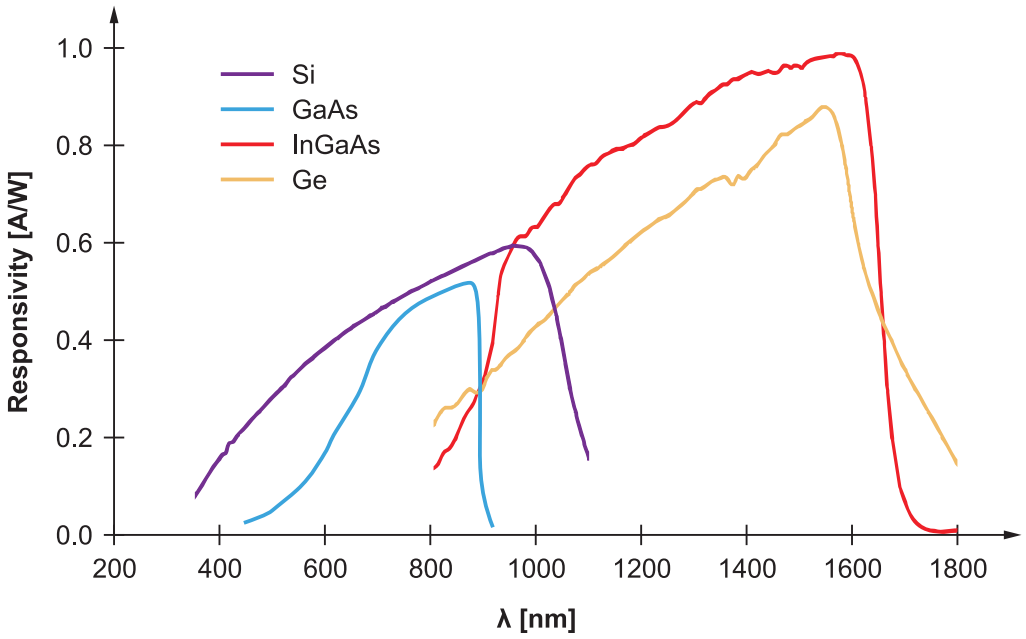

Figure 3.2: Photodiode responsivity versus wavelength for four different material systems.

carriers created due to the absorption of light. The intrinsic region also decreases the capacitance of the photodiode which allows higher operating speeds. Modern p-i-n photodiodes are capable of operating at frequencies of the order of tens of GHz. Increasing the width of the depletion region also increases the area available for capturing light. As the light is mostly absorbed within a certain distance, the thickness of the intrinsic layer is usually fabricated to match this distance. Any increase in intrinsic layer thickness beyond this limit will simply lead to lower speed of operation due to increased capacitance. A schematic diagram of a GaAs p-i-n photodiode is in Figure 3.3. Figure 3.4 then shows a commercial InGaAs p-i-n with a 30 µm diameter active area.

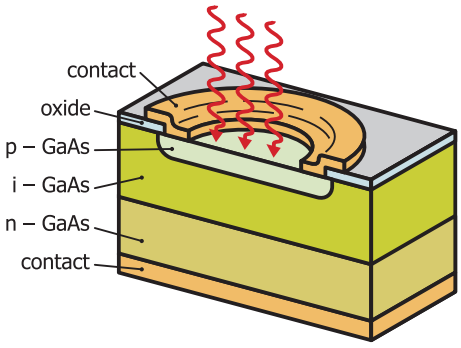

Figure 3.3: Schematic diagram of a top illuminated GaAs p-i-n photodiode.

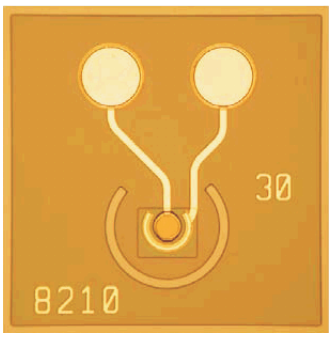

Figure 3.4: Enablence 18 GHz InGaAs photodiode with 30 µm diameter optical aperture, part №: PDCS30T.

3.1.3 Avalanche photodiodes

Avalanche photodetectors (APD) were rather promising semiconductor detectors in the last decade. In a simplified way, they can be described as a solid state version of proportional counters. Their operating principle is the amplification of a photoelectric current via the *avalanche effect*. Charge carriers created by incident optical radiation are accelerated by an electrostatic field to such an extent that their kinetic energy is sufficient to ionize atoms of the material through which they are traveling. The secondary charge carriers thus created are accelerated in turn and ionize further atoms to create the avalanche effect.

The responsivity, thus the sensitivity, of an avalanche diode is about a hundred times higher than that of a p-i-n photodiode. Reverse bias has to be set just below the avalanche breakdown voltage in order to reach the highest possible amplification. Dark currents, as well as the high-frequency properties, are similar to those of a p-i-n photodiode. The biggest disadvantage of APDs is the need for a high bias voltage – of order a hundred volts – for proper operation and this prevented their widespread use in high-speed data transmission systems. However, they still find application as single photon counting devices thanks to their high sensitivity.

3.2 Radiation effects in p-i-n photodiodes

Like lasers, p-i-n photodiodes were tested in the past to qualify them for use in experiments at the LHC. Photodiodes and lasers were tested together in a series of irradiations [36–38, 87]. Conversely to lasers, no high-fluence irradiation tests were performed for photodiodes, the cited tests only going up to the fluences expected at LHC. Apart from HEP experiments, radiation effects in photodiodes are also considered in space and/or solar cells applications [58, 59, 64, 65, 81, 91].

Since the materials of which p-i-n photodiodes are made are similar to those of semiconductor lasers, radiation effects are analogous to those of lasers. Displacement damage is much more important than ionization damage, at least for the fluences and doses typical of LHC. In p-i-n photodiodes, generation of electron-hole pairs at the defects created by displacement damage causes an increase in the dark current, which in turn raises the minimum power level of the optical signal that can be detected. In addition, photo-induced signal charge is trapped in radiation-induced defect states resulting in a reduction of the photocurrent.

3.2.1 Irradiation and annealing

The change in response of a p-i-n photodiode during irradiation is illustrated in Figure 3.5. The large increase in the leakage current and decrease in the responsivity, which is the slope of the curve, is distinctive. However, there is no clear correlation between the leakage current increase and responsivity decrease. The decrease in responsivity is largely affected by the type and the manufacturer of a p-i-n photodiode. Usually it remains within limits of 90 % of the value before irradiation up to a certain fluence after which it drops significantly.

The increase in leakage current together with decrease in responsivity of p-i-n photodiode with fluence is depicted in Figure 3.6. The leakage current increases non-linearly by several orders of magnitude for InGaAs photodiodes.

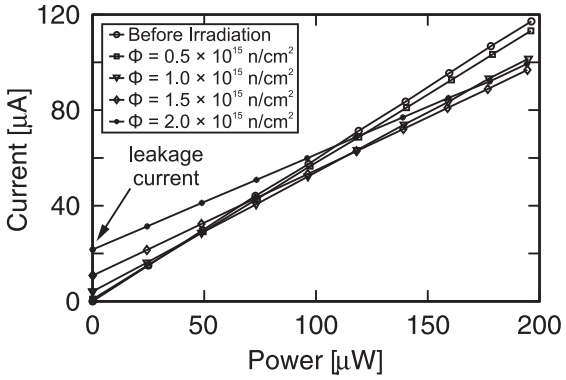

Figure 3.5: Degradation of the light–current characteristics of an InGaAs p-i-n due to 20 MeV neutron irradiation.

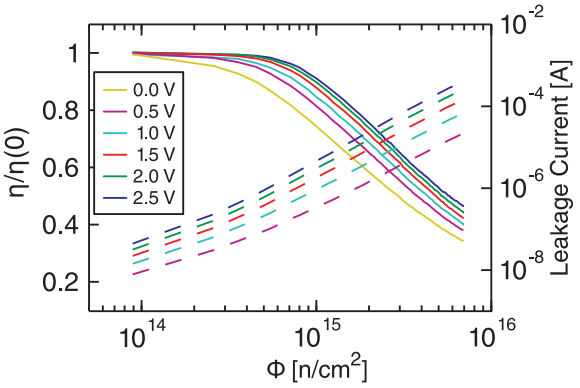

Figure 3.6: Relative responsivity and leakage current for different bias voltages as a function fluence of an InGaAs p-i-n.

Unlike lasers, the p-i-n photodiodes are damaged permanently by radiation. A small annealing of leakage current of 15–25 % during several hundreds of hours is observed; however there is no recovery of the p-i-n responsivity after irradiation. In terms of operation of p-i-n diodes in a digital optical link system, the change in leakage current and responsivity may be acceptable if the ability to distinguish between logical states is unaffected. The link receiver electronics must be able to compensate for higher leakage current and lower amplitude of the post-irradiation p-i-n photocurrent.

The irradiation testing of p-i-n photodiodes to HL-LHC fluence levels is extensively described in Chapter 4. Chapter 6 presents methods of mitigation of radiation induced damage in detector systems.

3.2.2 Single-event effects

Photodetectors used in high data-rate optical readout and control systems of current particle physics experiments unfortunately also serve as good particle detectors [13]. Particles traversing the photodetector may deposit a large fraction of their energy directly in the sensitive volume and cause a so-called *Single Event Upset* (SEU). Such effects are a concern for any modern high-speed electronic circuit operated in a radiation environment [26, 30, 50, 52].

The charge deposited in the sensitive volume of a photodetector, either by direct ionization or indirectly via elastic or inelastic collisions with nuclei of the detector material, is collected by the applied electric field. The resulting current pulse may be mistaken as a data signal by the receiving electronics, generating an SEU. The most sensitive region of a p-i-n diode is its depletion layer where any generated carriers are transported by drift. The resulting electrical signal is not only determined by the photodetector, but is shaped by the attached transimpedance and limiting

amplifiers. These components play an important role in single event effects, therefore the optical receiver chain must be considered as a whole.

Chapter 5 deals with SEU testing in photodiodes in detail and the methods of measuring, as well as simulating, SEUs are presented.

3.2.3 NIEL recapitulation

Since radiation damage in p-i-n photodiodes is caused almost exclusively by displacement damage, as in lasers, the NIEL hypothesis is also valid for photodiodes. This means that the same problems arise as for lasers due to the complexity of semiconductor compounds of which they are made: no radiation hardness scaling; uncertainty in stoichiometry; and difficulty of analytical calculation. The NIEL can thus only be predicted by simulation. Section 4.1.1 presents NIEL simulations for typical p-i-n photodiode materials.

A particular field of industry for which the description of radiation damage effects in terms of absorbed dose proves useful is that of space solar cells. Calculated NIEL values for various, typically *III-V* semiconductor, materials are used to predict the response of a device in the complex space radiation environment.

In a first step, the radiation effects in the solar cells are characterized using mono-energetic particle beams. Results from various sources are then correlated and relative NIEL factors are calculated. With a complete set of NIEL values for different semiconductor materials, sources and energies, radiation hardness of solar cells can be evaluated at a single, readily available particle source, usually 1–10 MeV proton source.

The performance of a solar cell in space is then predicted from the knowledge of the space radiation environment. This approach significantly reduces the amount of experimental data needed to predict solar cell behaviour in the final application, which in turn means that even cell types for which limited test data exist can be considered for particular space missions.

A similar approach can be adopted also for HEP experiments; however readily available sets of experimental NIEL data together with well chosen proxy particle sources are rather limited.

3.3 Summary

The operational principles of lasers and photodiodes were presented with a review of radiation effects in semiconductor optoelectronic components. The influence of radiation on measurable device parameters was outlined. Typical material systems and structures were described and the concept of the NIEL was introduced. In addition to that, laser behaviour was described using rate-equations for both steady-state and small signal analysis which prepared the ground for an extended laser model which is introduced in next experimental chapter.

Chapter 4

Radiation testing of lasers and photodiodes

This chapter reports on extensive exploratory tests of modern 10 Gbps optoelectronic components and their suitability for the HL-LHC trackers is discussed based on thorough device irradiation and annealing models. These high fluence irradiation tests – in excess of 10^{15} particles/cm^2 – took place at UCL, Belgium with 20 MeV neutrons and with 300 MeV/c pions in PSI, Villigen, Switzerland.

4.1 Overview of sources used

Two irradiation sources were used for these exploratory tests as proxies of HL-LHC radiation environment. The first was a neutron source derived from a 50 MeV deuteron beam impinging on a beryllium target via the ^{9}Be(d,n)^{10}B reaction. The neutron beam energy distribution and angular divergence are shown in Figure 4.1 and Figure 4.2, respectively. The energy distribution of the neutron beam exhibits a significant peak at 20 MeV. In the following, this source will be referred to as a 20 MeV mono-energetic source.

The dosimetry for the neutron irradiation was intended to be done using alanine pellets stuck to various places in the setup. Since these pellets were rated only up to a fluence of 1×10^{15} n/cm^2 beyond which they saturate, the total fluence Φ for neutron irradiations had to be calculated solely using the following formula [66]:

$$\Phi(t,d) = \int_{t_0}^{t} I(\tau)\mathrm{d}\tau \times \frac{1 \times 10^{14}}{0.079 \cdot d^{1.902}} \tag{4.1}$$

where I is the measured deuteron current and d is the distance from the target.

The other source was a pion one of an energy of 191 MeV. The total fluence was calculated using the β^- decay of the ^{24}Na isotope in aluminium foil activated by negatively charged pions. This β^- activity was used to calibrate the monitored pion beam current.

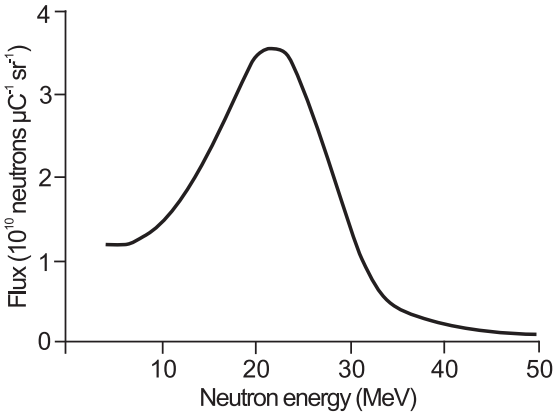

Figure 4.1: Neutron energy distribution, data from [66].

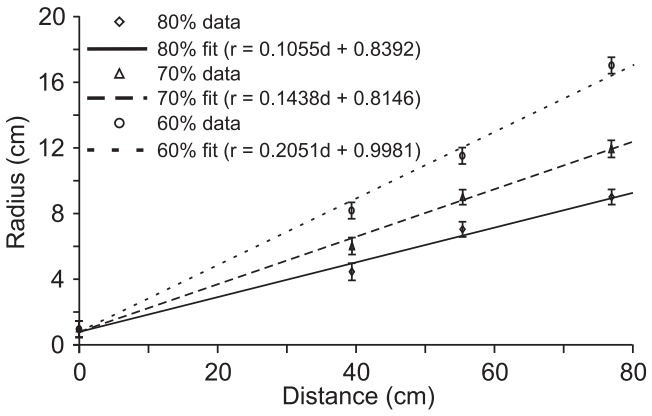

Figure 4.2: Neutron angular divergence as a function of distance from target with radius referring to beam axis, data from [66].

4.1.1 Relative NIEL and relation with HL-LHC environment

As mentioned in previous chapters, the analytical calculation of NIEL for complex semiconductor compounds is rather challenging and has not yet been carried out. In order to compare the destructiveness of irradiation sources used for device testing and put it into the context of the HL-LHC environment relative NIEL factors were calculated for 1 MeV, 20 MeV neutrons, 191 MeV pions and 24 GeV protons for various semiconductor compounds using the FLUKA and GEANT4 simulators.

The NIEL was calculated for the following materials and stoichiometry: GaAs, $In_{0.53}Ga_{0.47}As$, $In_{0.738}Ga_{0.262}As_{0.568}P_{0.432}$, and $In_{0.557}Ga_{0.443}As_{0.950}P_{0.050}$ and for targets of three different thickness of 1, 10 and 100 µm. Densities of these compounds were taken from [51]. This set of materials represents typical semiconductor compounds of which lasers and p-i-n photodiodes are made, refer to Chapters 2, 3. Targets of three different thicknesses were used to confirm the thin target hypothesis, which means that particles are not stopped, nor significantly slowed down inside the material and that the calculated NIEL per particle per cm^3 does not depend on detector thickness. This was not true for the 24 GeV proton case where only the 100 µm target was used. The reason for this is that the 24 GeV proton simulation was run last and the thin target hypothesis had been confirmed.

FLUKA simulations

First simulations were performed using FLUKA. It is a general purpose Monte Carlo simulation tool developed since 1989 for calculations of particle transport and interactions with matter. Among other applications, this simulation package written in the Fortran 77 language is designed for shielding, calorimetry, dosimetry, radiotherapy and detector and target design. Prediction of radiation induced damage is a traditional field of application of FLUKA which makes it suitable for NIEL simulations.

Simulations to high accuracy of about 60 different particles and their associated anti-particles

are possible in FLUKA in an energy range from ≈ 1 keV to hundreds of TeV. Of a great interest is its low-energy neutron model which is able to simulate neutrons with energy lower than 20 MeV down to thermal energies. It uses its own neutron cross section library derived from recent experimental data.

The advantage of FLUKA is that no programming is required from the user for most of the basic applications. The simulation can be run from a graphical user interface. Simple geometries are easily implemented. For more complex geometries FLUKA uses a combinatorial geometry package, which is not needed for this simple NIEL simulation where a target is simply a block of detector material.

In order to reduce the simulation processing time, in every simulation run, 5×10^9 particles were simulated with a so-called mulsopt card option. The mulsopt card was used for activating the single scattering option at boundaries or for too short steps, where the number of single scatterings to be performed when crossing a boundary was set to one. The result is weighted by the probability of interaction, i.e. no further corrections are needed. In other words, the mulsopt card forces the particle to interact at every crossed boundary which makes it very suitable for thin targets where the probability of interaction is very low. In this way transport of a particle without any interaction is completely eliminated and the speed of simulation is increased.

Results of FLUKA simulations are summarized in tables 4.1, 4.2 and 4.3 for three different target thicknesses.

particles	**GaAs**	**InGaAs**	**InGaAsP$_{0.432}$**	**InGaAsP$_{0.050}$**
1 MeV neutrons	10.0	8.5	8.8	8.5
20 MeV neutrons	52.0	44.6	40.7	44.4
191 MeV pions	84.3	82.2	72.0	81.5
ratio	1:5.2:8.4	1:5.2:9.7	1:4.6:8.2	1:5.2:9.6

Table 4.1: NIEL in keV/cm^3/particle for 1 μm thick target in FLUKA. The exact stoichiometry of individual compounds is referenced in text.

particles	**GaAs**	**InGaAs**	**InGaAsP$_{0.432}$**	**InGaAsP$_{0.050}$**
1 MeV neutrons	9.9	8.5	8.7	8.5
20 MeV neutrons	51.6	44.8	40.7	44.4
191 MeV pions	84.5	82.2	72.9	81.2
ratio	1:5.2:8.5	1:5.3:9.6	1:4.7:8.4	1:5.2:9.5

Table 4.2: NIEL in keV/cm^3/particle for 10 μm thick target in FLUKA.

GEANT4 simulations

GEANT4 is a Monte Carlo simulation software framework which provides detector and physics modelling capabilities embedded in an object-oriented structure. This simulation tool, whose development dates back to 1993, is used in a large variety of experimental applications in diverse

particles	GaAs	InGaAs	$InGaAsP_{0.432}$	$InGaAsP_{0.050}$
1 MeV neutrons	10.0	8.6	8.8	8.6
20 MeV neutrons	51.7	45.0	40.8	44.5
191 MeV pions	84.5	82.8	73.7	81.8
24 GeV protons	64.3	80.4	78.3	80.0
ratio	1:5.2:8.5:6.4	1:5.3:9.7:9.3	1:4.6:8.4:8.9	1:5.2:9.6:9.3

Table 4.3: NIEL in keV/cm^3/particle for 100 μm thick target in FLUKA.

experimental domains like high energy physics experiments, space applications and medical applications, to name a few.

GEANT4 includes physical processes starting from optical photons and thermal neutrons to the TeV range used at the LHC. However, its main use is in the high energy range. Models for low energy particles are still being pioneered and need quite often to be fine tuned by the user.

Curiously, one of the drawbacks of GEANT4 when used for simple applications is its general purpose nature. A lot of effort is needed even for running a basic simulation. It starts with a cumbersome definition of geometry, material specification, physics processes and continues to management of individual events and run configuration. On the other hand, the GEANT4 toolkit comprises various examples and training kits.

Similar simulations to the ones carried out using FLUKA were performed using GEANT4 in order to compare and gain confidence in the results. The QGSP_BIC_EMY reference physics list (version 1.1), which should incorporate low-energy neutrons physics, was used to model the NIEL deposit in the material as suggested by the GEANT4 collaboration. Due to obvious discrepancies in the obtained values of NIEL, these simulations were run only for GaAs and InGaAs $1 \times 1 \times 1$ mm targets. This failure can be attributed to the physics list which is not obviously mature for this kind of application. The results of simulations are summarized in Table 4.4.

particles	GaAs	InGaAs
1 MeV neutrons	0.67×10^{-3}	0.65×10^{-3}
20 MeV neutrons	3.75	2.07
191 MeV pions	0.14	0.11
ratio	1:5 597:209	1:3 185:169

Table 4.4: NIEL in keV/cm^3/particle for 1 mm thick target simulated in GEANT4.

Results discussion

As can be seen from tables 4.1, 4.2 and 4.3 the NIEL does not depend on detector thickness and the assumption of a thin target is thus valid. The factor between 20 MeV neutrons and 191 MeV pions is 1.6 for GaAs, and 1.8 for InGaAs and both InGaAsP materials, whereas the ratio between 1 MeV and 20 MeV neutrons has the same value of 5.2 for GaAs, InGaAs and $In_{0.557}Ga_{0.443}As_{0.950}P_{0.050}$ and 4.6 for $In_{0.738}Ga_{0.262}As_{0.568}P_{0.432}$.

When comparing these simulated ratios to previously measured values [40] of 1:4.4:8.3 of InGaAsP laser for 0.8 MeV, 20 MeV neutrons and 191 MeV pions a reasonable match is obtained.

The stoichiometry of compounds does not play a significant role for a relative NIEL factors between the beams, 20 MeV neutrons and 191 MeV pions, in the two irradiation facilities but has a slight impact on 1 MeV neutron scaling.

Using the NIEL simulations, the scaling of measured radiation damage either in a neutron or pion beam to 1 MeV neutron equivalent is possible. The precision is higher when the exact stoichiometry of compounds in question is known but even taking generic stoichiometry values a satisfactory estimation is obtained.

To confront the absolute values of the simulated NIEL with literature is not feasible since most of the published work is with simpler semiconductor compounds, mainly silicon. There are few exceptions for GaAs material like [22] whose simulated NIEL values for 1 MeV neutrons, 191 MeV pions and 24 GeV protons are generally four-times lower than values obtained by FLUKA simulations. However, this does not represent a significant issue since it is only the ratio between the different sources which is of interest for this work and this is in accordance with measured data.

Unfortunately, the GEANT4 simulations with the reference physics list do not provide meaningful results, thus only FLUKA simulations should be considered for the source comparison. Apparently, some low energy transfers processes are missing in the current reference physics list which could be possibly rectified in future releases.

The measured and scaled radiation damage of a tested device in a 1 MeV neutron equivalent flux can be linked together with a radiation map of a HL-LHC tracker mentioned in a section 1.3.3 and thus its suitability for a given placement can be determined.

4.2 Devices tested

A large quantity of modern devices– capable of 10 Gbps – was tested during two neutron and one pion irradiation tests. The radiation resistance of 56 prototype semiconductor lasers from nine different manufacturers and of 39 p-i-n photodiodes from five different manufacturers was evaluated for total fluences in excess of 10^{15} particles/cm^2. Devices using various technologies, like 1310 nm Fabry-Pérot lasers as well as 1310 nm and 850 nm VCSELs with both 1310 nm InGaAs and 850 nm GaAs p-i-n photodiodes, were tested together with devices currently used in CMS which were included for comparison to previous tests. The parameters of the neutron and pion tests are given in Table 4.5. The overview of all lasers and p-i-ns tested is summarized in Table 4.6 and Table 4.7, respectively.

	Neutrons 1	Neutrons 2	Pions
Mean energy:	20 MeV	20 MeV	191 MeV
Irradiation time:	3 days	24 h	17 days
Particle flux [p/cm^2/s]:	$1.4–2.4 \times 10^{10}$	$2.3–8.1 \times 10^{10}$	$0.6–1.2 \times 10^{9}$
Annealing time:	1 month	3 months	2 weeks
Lasers irradiated:	19	24	13
p-i-ns irradiated:	27	8	4

Table 4.5: The main parameters of all neutron and pion tests.

Manufacturer	# devices	Type	λ [nm]	Neutron 1 Φ [$\times 10^{15}$/cm^2]	Neutron 2 Φ [$\times 10^{15}$/cm^2]	Pion Φ [$\times 10^{15}$/cm^2]
Alight	2	VCSEL	1310	–	–	1.6
BeamExpress	2 + 2	VCSEL	1310	–	2.0	0.9
Binoptics	2	Fabry-Pérot	1310	4.4	–	–
Cyoptics	2	Fabry-Pérot	1330	–	2.1	–
Finisar	3 + 2 + 2	Fabry-Pérot	1310	4.8	2.0	1.2
Finisar	3 + 6 + 2	VCSEL	850	4.7	2.1	1.5
JDSU	3 + 4 + 2	VCSEL	850	4.4	2.0	1.5
Mitsubishi	8 + 1	Fabry-Pérot	1310	–	2.3	1.3
QD	3	Quantum dot	1310	4.8	–	–
Vertilas	3	VCSEL	1310–1550	5.0	–	–
CMS ref.	2 + 2	Fabry-Pérot	1310	6.3	–	1.7

Table 4.6: List of all irradiated lasers with fluences reached in individual irradiation campaigns – all devices except CMS reference are rated at 10 Gbps.

4.3 Radiation testing setup

A modular measurement setup and individual instruments controlled by LabView software were used to measure both lasers and p-i-n photodiodes. Figure 4.3 shows a picture of the whole setup.

Manufacturer	# devices	Type	λ [nm]	Neutron 1 Φ [$\times 10^{15}$/cm^2]	Neutron 2 Φ [$\times 10^{15}$/cm^2]	Pion Φ [$\times 10^{15}$/cm^2]
Enablence	8 + 6 + 2	InGaAs	850, 1310	3.5	5.2–7.0	1.3
Finisar	3	InGaAs	1310	3.9	–	–
Finisar	3	GaAs	850	3.9	–	–
Hamamatsu	6	InGaAs	1310	4.2	–	–
Hamamatsu	3	GaAs	850	4.2	–	–
JDSU	2 + 2	GaAs	850	3.9	–	1.5
CMS ref.	2 + 2	InGaAs	1310	6.2	1.6	–

Table 4.7: List of all irradiated p-i-n photodiodes with fluences reached in individual irradiation campaigns – all devices except CMS reference are rated at 10 Gbps.

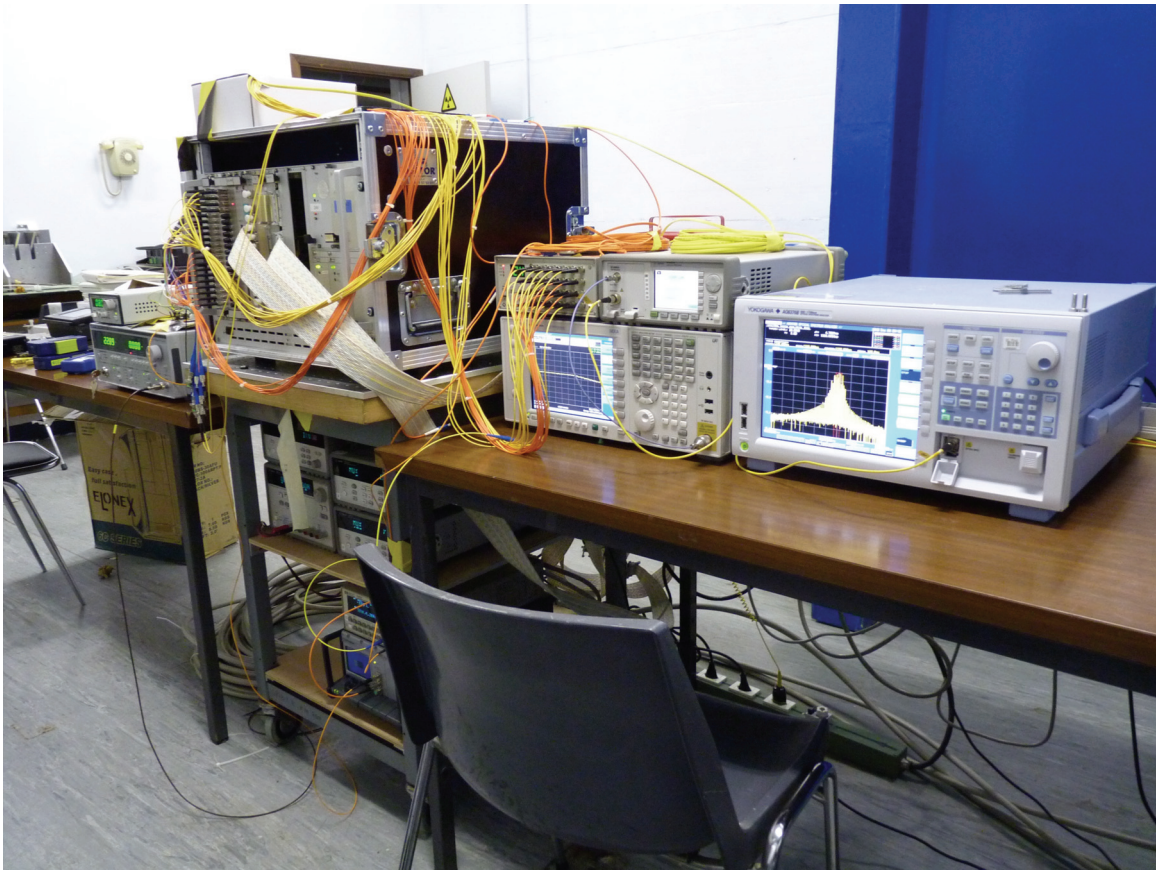

Figure 4.3: Picture of a complete measurement apparatus. From right to left: optical spectrometer followed by an electrical spectrometer with an optical-to-electrical converter and a switch on top of it, measurement rack with data loggers and optical attenuators below it, and laser current drivers on the far left.

4.3.1 Laser measurement setup

A schematic of the measurement setup for lasers used for both neutron and pion irradiations is shown in Figure 4.5. The *L-I-V* characteristics of all lasers were continuously measured at approximately 20 minute intervals. Between the measurements lasers were biased at a constant current above threshold. The optical and electrical spectra were also recorded. A measurement cycle diagram with a laser current curve is shown in Figure 4.4.

4.3.2 Photodiode measurement setup

The dependence of the photodiode current on input light power for different bias voltages was measured with a setup shown in Figure 4.6. This measurement was performed after the scanning of laser *L-I-V* characteristics.

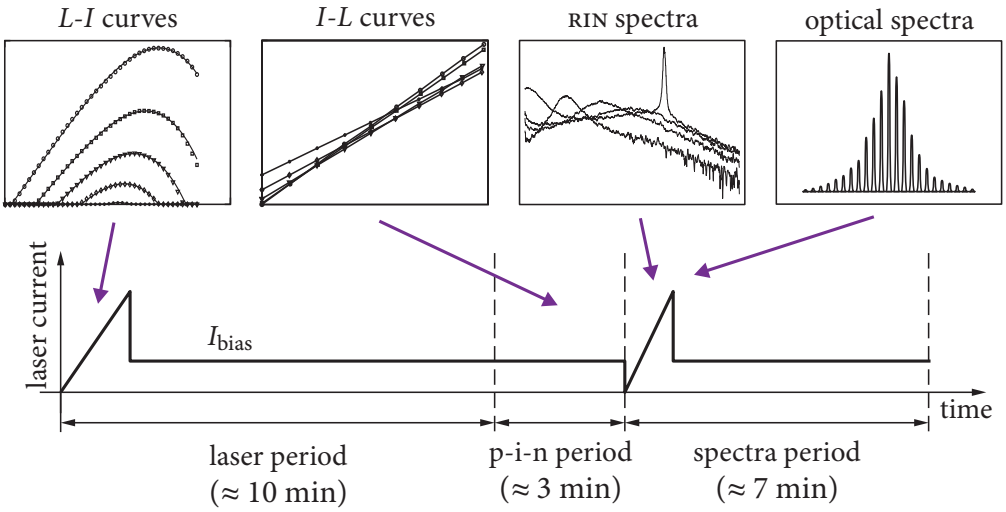

Figure 4.4: The device measurement cycle with durations of individual measurement cycles and laser biasing profile.

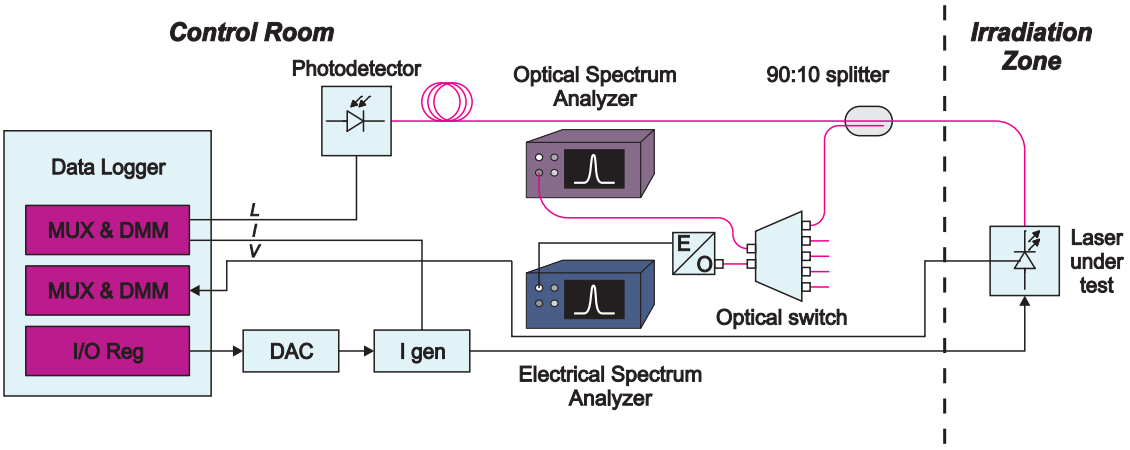

Figure 4.5: The laser measurement setup. Lasers are individually biased by a current driver and the intensity of emitted light is measured by a photodetector with the recording of optical and RIN spectra.

4.3.3 Control software

The measurement setup was controlled by a National Instruments LabVIEW application. This application allowed to set individual instruments, temperature sensors and other environmental parameters. Measurement of individual devices could be turned on or off and laser and p-i-n diode results displayed for a quick check of device operation.

4.4 Neutron results

The raw results with extracted trends of lasers and photodiodes are presented in this section for two 20 MeV neutron tests at Université Catholique de Louvain (UCL), Louvain-la-Neuve, Belgium.

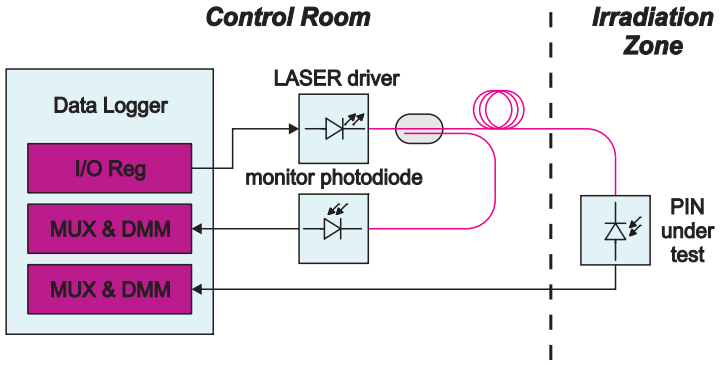

Figure 4.6: The p-i-n measurement setup. Two lasers of 850 and 1310 nm were used as a light source for p-i-n photodiodes under test. Laser drivers were ramped up and a corresponding current flowing through the p-i-n photodiode was recorded. The emitted intensity of the light was monitored by a photodiode placed close to the laser driver.

4.4.1 Louvain test 2009

This first test, which lasted for about three days of irradiation from 18/08/2009–22/08/2009 followed by one month of annealing, was the first exploratory test. It aimed mainly to survey new fast optoelectronic devices from various manufacturers and to observe their ultimate limits. Despite two beam failures which occurred during the test, a ten times higher fluence, 4×10^{15} n/cm^2, was reached than in previous tests used to qualify devices for the LHC. This test was also the first one in which edge-emitting lasers were irradiated together with VCSELs.

Device assembly

A schematic diagram of a device stack is in Figure 4.7. All lasers were placed closer to the beam, i.e. in higher flux, than p-i-n photodiodes. Lasers of the same type were connected in series, typically in groups of three, and ramped up simultaneously.

Laser results

Some of the raw laser results are presented in this sub-section together with extracted trends of all irradiated lasers.

In Figure 4.8 a set of *L-I* and *V-I* plots versus fluence is shown for a reference Mitsubishi device. This device, which is currently used in CMS did not last for a long time and was destroyed by radiation at a fluence of 2×10^{14} n/cm^2. In this test, the maximum fluence reached for lasers was 6.3×10^{15} n/cm^2. The colour code in Figure 4.8, which is the same for all *L-I-V* curves of lasers irradiated in this campaign, corresponds to this value.

In contrast to the reference device, a newer 10 Gb/s capable edge-emitting device reached a higher fluence. Results are shown in Figure 4.9.

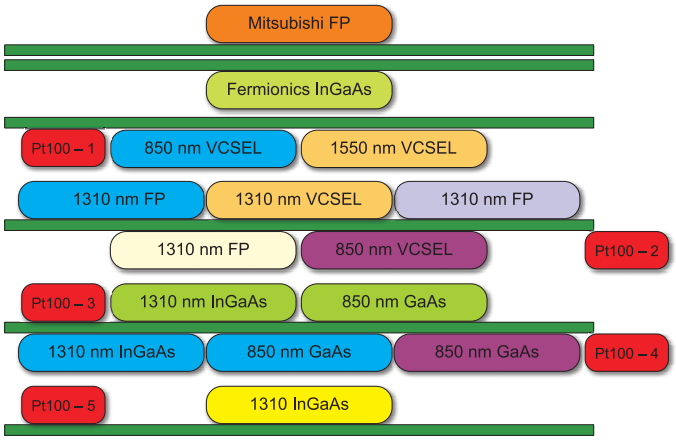

Figure 4.7: The device stack. The beam is coming from the top. Closest to the target were CMS reference devices followed by lasers and p-i-n photodiodes.

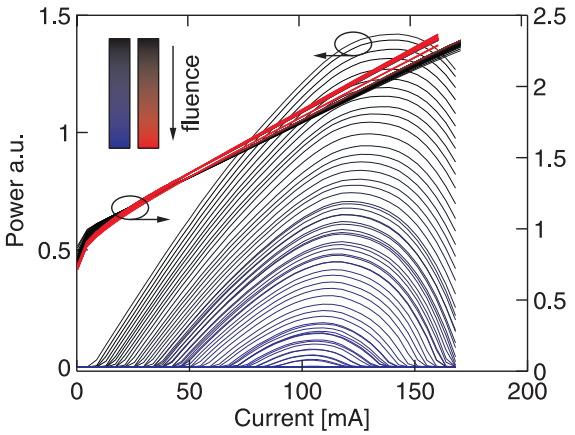

Figure 4.8: Set of *L-I* and *V-I* curves of a reference Mitsubishi device with a common colour code corresponding to a maximum fluence of 6.3×10^{15} n/cm^2

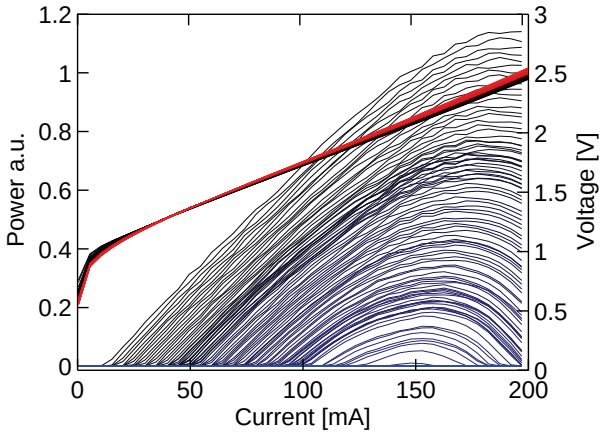

Figure 4.9: Set of *L-I* and *V-I* curves of a 10 Gb/s Finisar 1310 nm edge-emitting laser.

A few lasers which survived the whole irradiation were solely VCSELs. Figure 4.10 and Figure 4.11 show a short and long wavelength VCSELs, respectively.

Comparative plots of relative threshold increase, efficiency and maximum power versus fluence with annealing are in Figures 4.12, 4.13 and 4.14, respectively.

Photodiode results

Some malfunctioning was registered for certain p-i-n photodiodes, mainly due to a bad optical fibre contact with a device can.

Figure 4.15(a) shows relative responsivity and leakage current for different bias voltages of a reference Fermionics p-i-n photodiode. The kink in the responsivity trend is typical for this

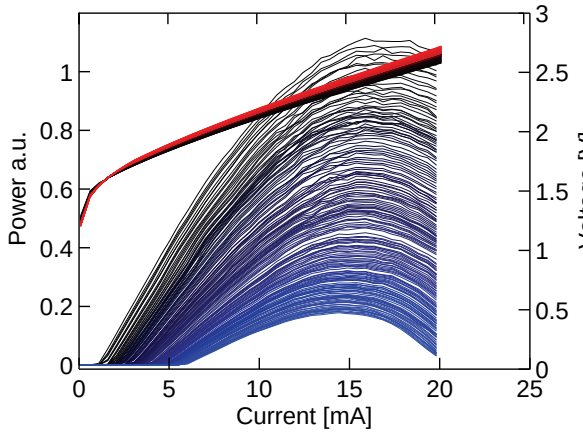

Figure 4.10: Set of *L-I* and *V-I* curves of a Finisar 850 nm VCSEL.

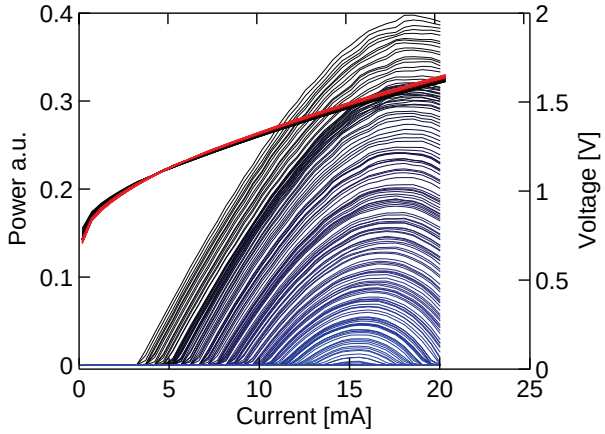

Figure 4.11: Set of *L-I* and *V-I* curves of a Vertilas 1550 nm VCSEL.

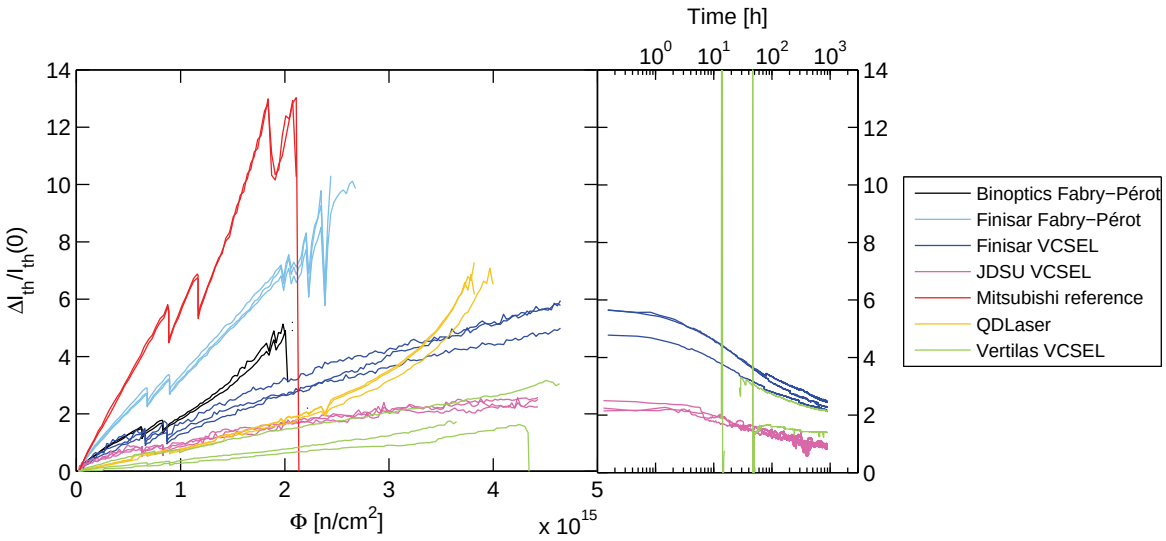

Figure 4.12: Relative laser current threshold shift versus fluence with annealing.

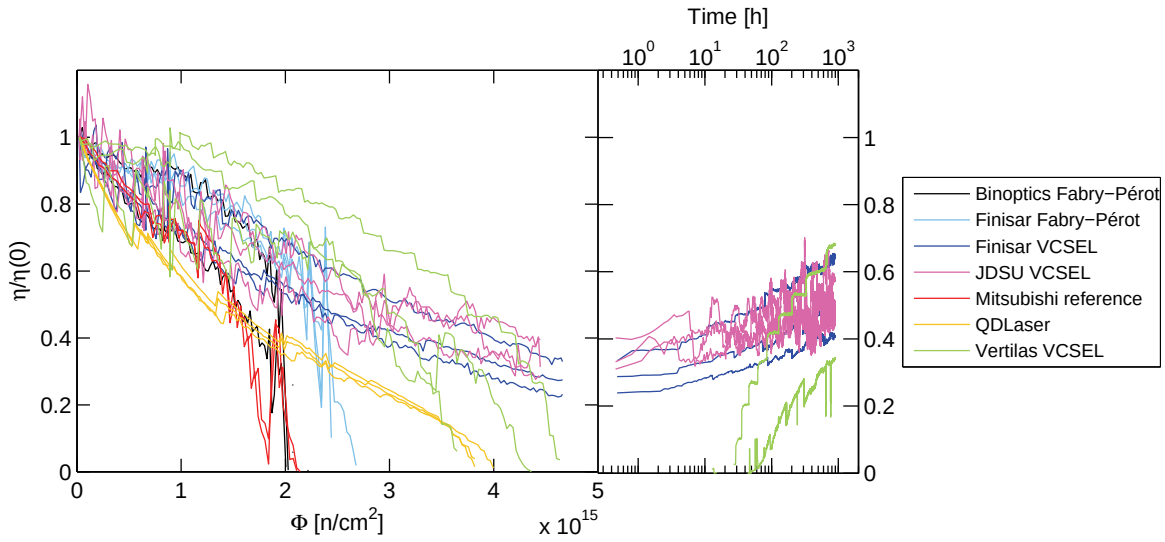

Figure 4.13: Relative laser efficiency versus fluence with annealing.

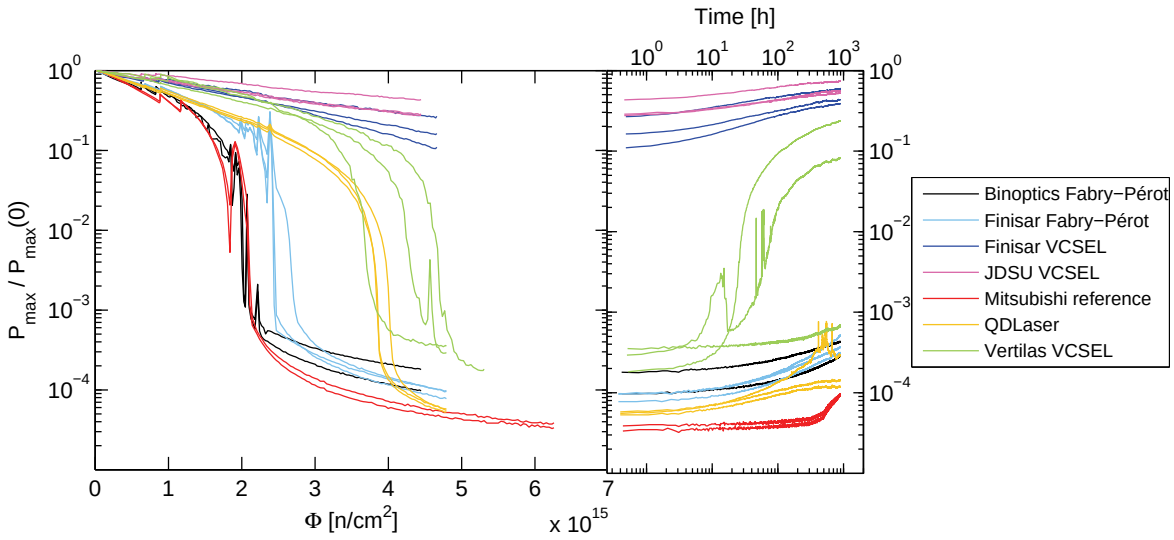

Figure 4.14: Normalized maximum laser output power versus fluence with annealing.

particular device.

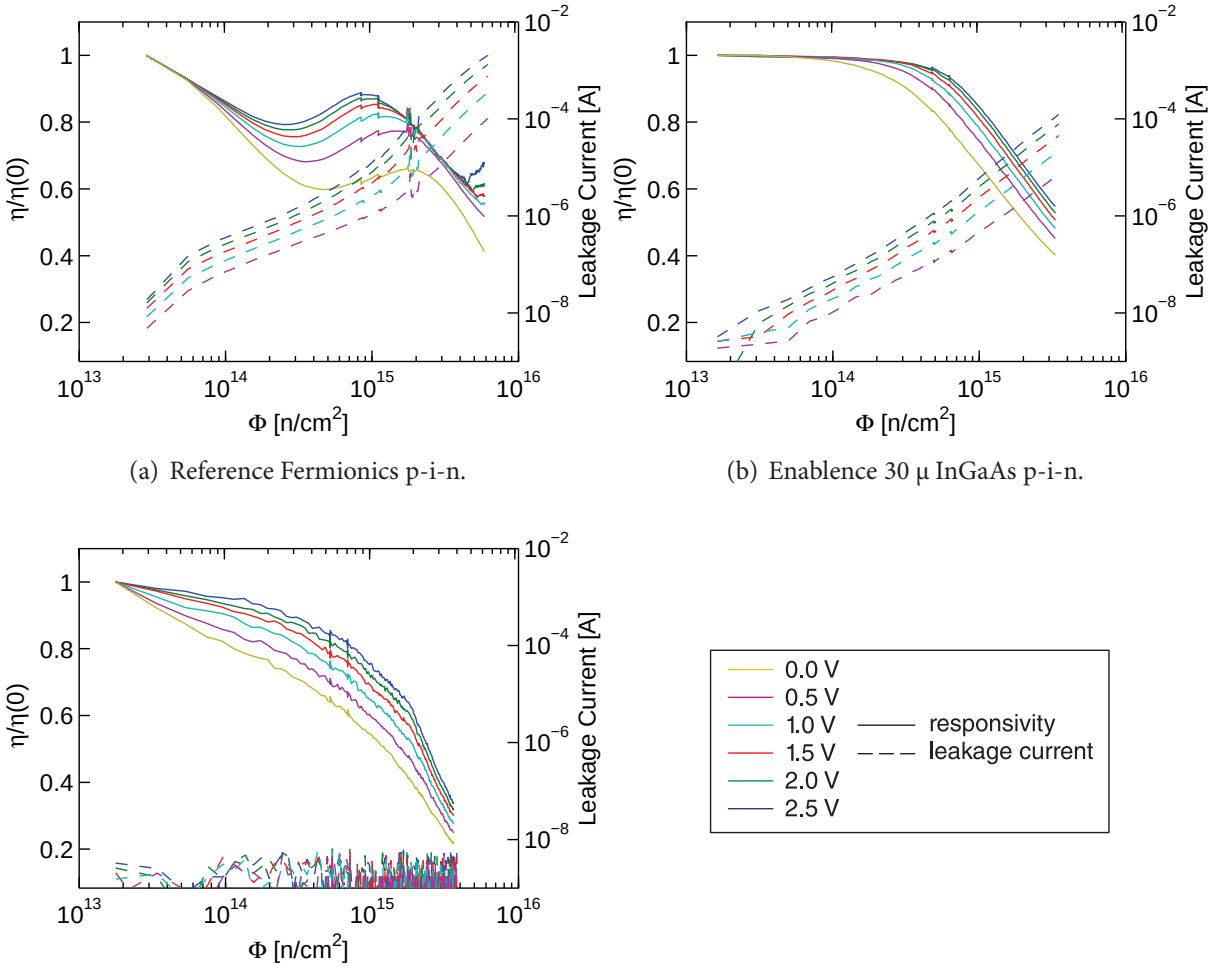

(a) Reference Fermionics p-i-n.

(b) Enablence 30 μ InGaAs p-i-n.

(c) JDSU GaAs p-i-n.

(d) Legend.

Figure 4.15: Relative responsivity and leakage current for different bias voltages of selected p-i-n photodiodes.

Results on relative responsivity and a leakage current for different bias voltages for modern fast Enablence 30 μ 1310 nm InGaAs and JDSU 850 nm GaAs photodiodes are in Figures 4.15(b) and 4.15(c), respectively.

Plots comparing the leakage current and relative responsivity for all p-i-n devices are in Figures 4.16 and 4.17, respectively.

Discussion

Despite some problems with the beam stability, this test was successful and demonstrated on a representative sample of data that modern and fast devices are more radiation hard than older devices currently used in CMS.

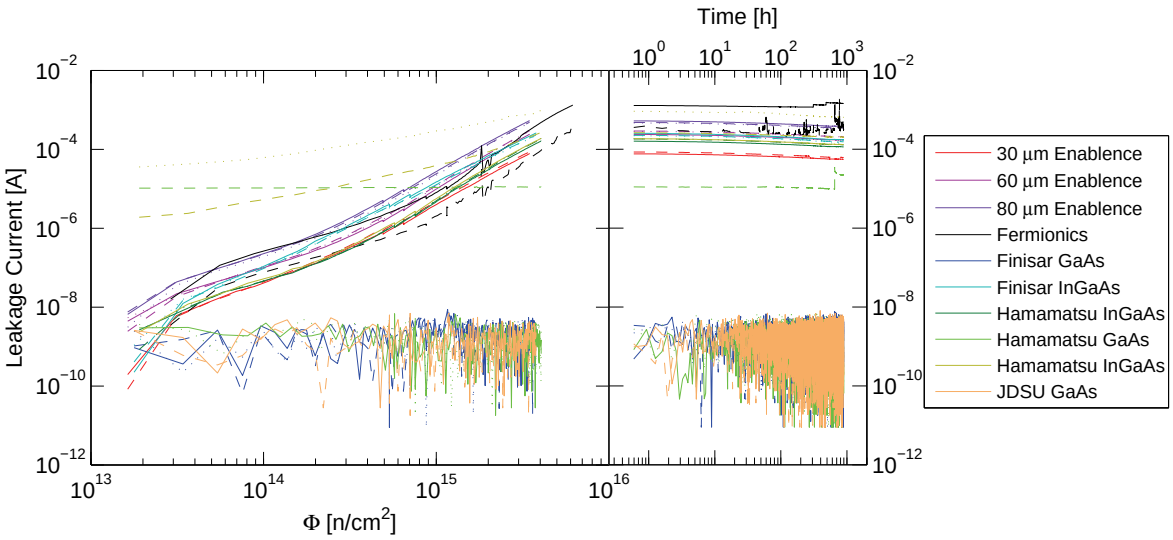

Figure 4.16: Leakage current versus fluence at 2.0 V bias with annealing.

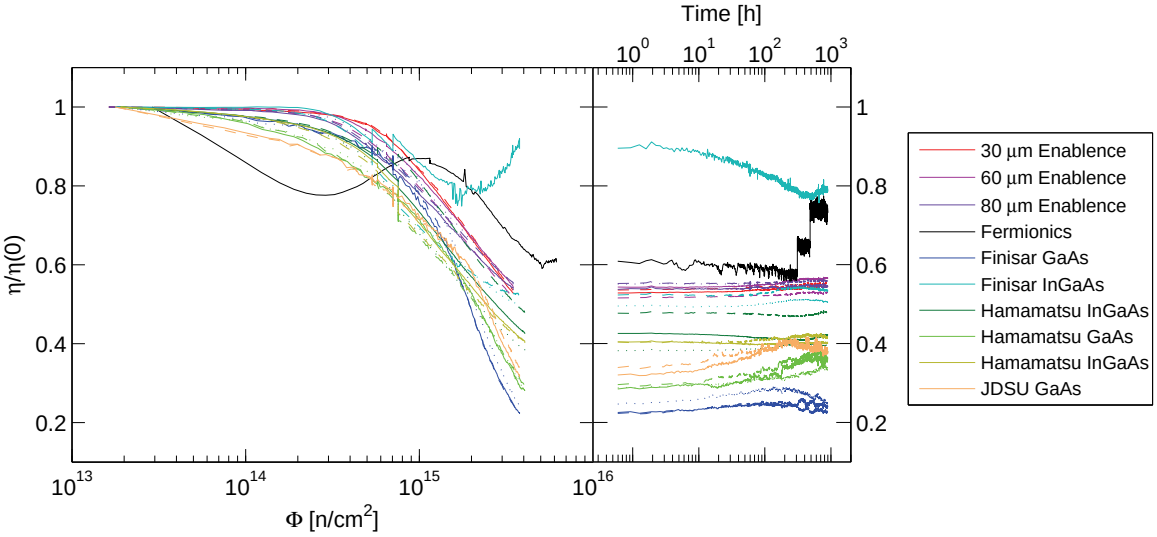

Figure 4.17: Relative responsivity versus fluence at 2.0 V bias with annealing.

Laser results confirmed the assumption that VCSELs are more radiation hard than edge-emitting lasers. The limit for edge-emitting lasers in this test was 2×10^{15} neutrons/cm^2 whereas for VCSELs it was higher than 4×10^{15} neutrons/cm^2. The importance of laser annealing was also manifested. Some lasers which were killed by radiation started lasing again after some period of time. Due to a large number of laser types, only three devices of the same type were irradiated but even from this limited number of samples one can state that similar behaviour was observed across device families.

Another fact that is evident from laser *L-I-V* curves is that while *L-I* curves are hugely affected by radiation, *V-I* curves are not. Defects which are created in the crystal lattice by radiation have a large impact on band-to-band transitions, thus affecting the lasing, but from the electrical point of view it does not matter whether the transition is radiative or non-radiative. This could explain the observed behaviour of *L-I* and *V-I* curves of irradiated lasers.

Unlike the lasers, all p-i-n photodiodes survived the irradiation. This fact is thanks both to a lower total fluence and also higher radiation resistance. Unfortunately, p-i-n photodiodes do not anneal significantly, thus the radiation damage is permanent. Only a small fraction of photodiode leakage current anneals. Several differences between 850 nm GaAs and 1310 nm InGaAs devices were observed. Most noticeable is very low leakage current for GaAs photodiodes which remained below the resolution of the measuring apparatus throughout the test. The other difference is a faster drop in responsivity with fluence for GaAs devices and also their lower sensitivity. The increased noisiness in trends for 850 nm devices is caused by a modal instability of a combination of a VCSEL laser and a multi-mode splitter which were used for light feeding.

4.4.2 Louvain test 2010

The purpose of this 24 h long test, 06/12/2010–07/12/2010, followed by two and half months of annealing, was to investigate the influence of the laser bias current on radiation damage and rate of annealing. This was also the reason for the extremely long period of annealing. To see if there is a significant dependence of radiation damage on laser bias current, some of the devices were biased at different currents, always in a group of two. As in the pion test, the spectra were also measured, but only every fourth cycle due to a large number of devices.

Device assembly

Contrary to the previous neutron test in 2009, p-i-n photodiodes were placed closer to the beryllium target in order to be in a higher neutron flux. Lasers were thus exposed to a lower flux and since none of them was destroyed during the test, it was possible to measure the annealing. The schematic of the device stack is in Figure 4.18.

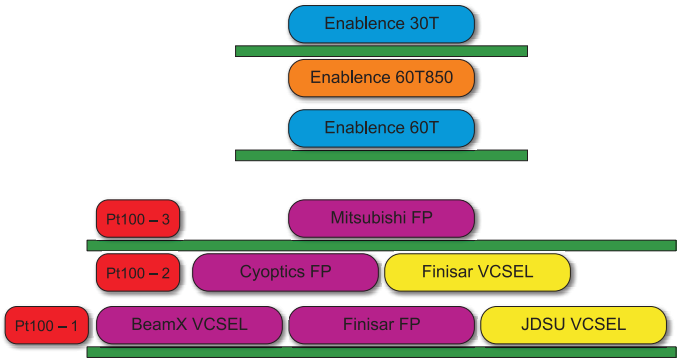

Figure 4.18: The device stack. The beam is coming from the top. Contrary to the 2009 neutron test, closest to the target were p-i-n photodidodes followed by lasers with platinum temperature sensors (PT100).

Laser results

Figure 4.19 shows measured *L-I* and *V-I* curves for a Mitsubishi 1310 nm Fabry-Pérot laser, Finisar 1310 nm Fabry-Pérot laser, Finisar 850 nm VCSEL and BeamExpress 1310 nm VCSEL. The colour code in Figure 4.19(a) corresponds to the maximum fluence of 2.3×10^{15} n/cm^2 and is the same for all plots of irradiated lasers in this campaign. Unlike in the previous neutron test, none of the lasers was seriously damaged by radiation, thus they had a measurable annealing period.

The fraction of remaining defects, proportional to threshold current change, versus time for different bias currents above laser threshold for the same device types as in Figure 4.19 is shown in Figure 4.36. It is clearly demonstrated that the annealing rate does not depend on bias current and that part of the induced damage is permanent.

As for the previous test, comparative plots of relative threshold increase and efficiency versus fluence with annealing are in Figures 4.20 and 4.21, respectively.

Photodiode results

Only six InGaAs p-i-n photodiodes of two different types were irradiated in this test. Two of the InGaAs photodiodes had a 850 nm light source. The measured characteristics are shown in Figure 4.22. A drop of a relative responsivity and the flat part of the leakage current curve for the highest bias voltages for some devices at the end of measurement is due to a saturation of a current-to-voltage converter which was used during measurement.

A comparison of the leakage current and relative responsivity for all p-i-n devices are in Figures 4.23 and 4.24, respectively.

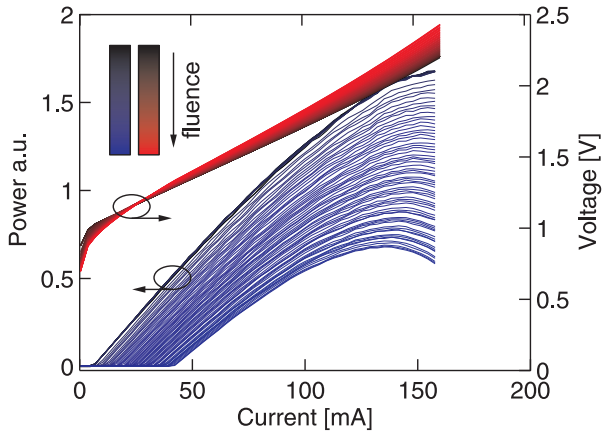

(a) Mitsubishi Fabry-Pérot laser with a common colour code corresponding to a maximum fluence of 2.3×10^{15} n/cm^2

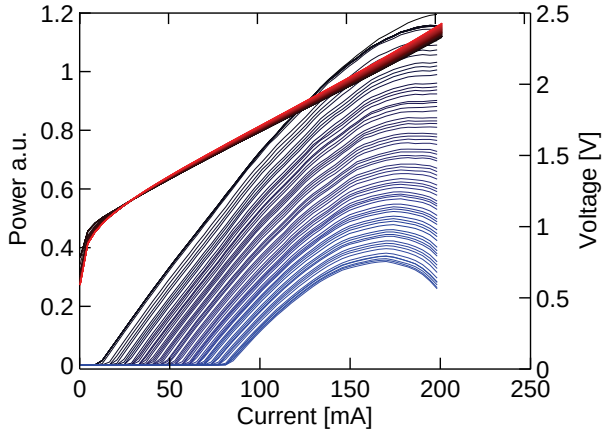

(b) Finisar Fabry-Pérot laser.

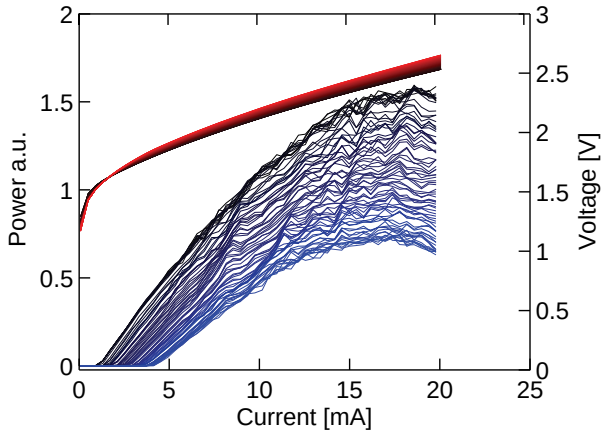

(c) Finisar VCSEL.

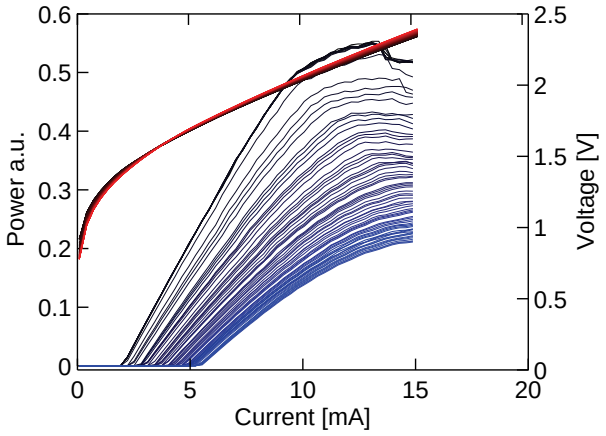

(d) BeamExpress VCSEL.

Figure 4.19: Set of *L-I* and *V-I* curves of neutron irradiated lasers.

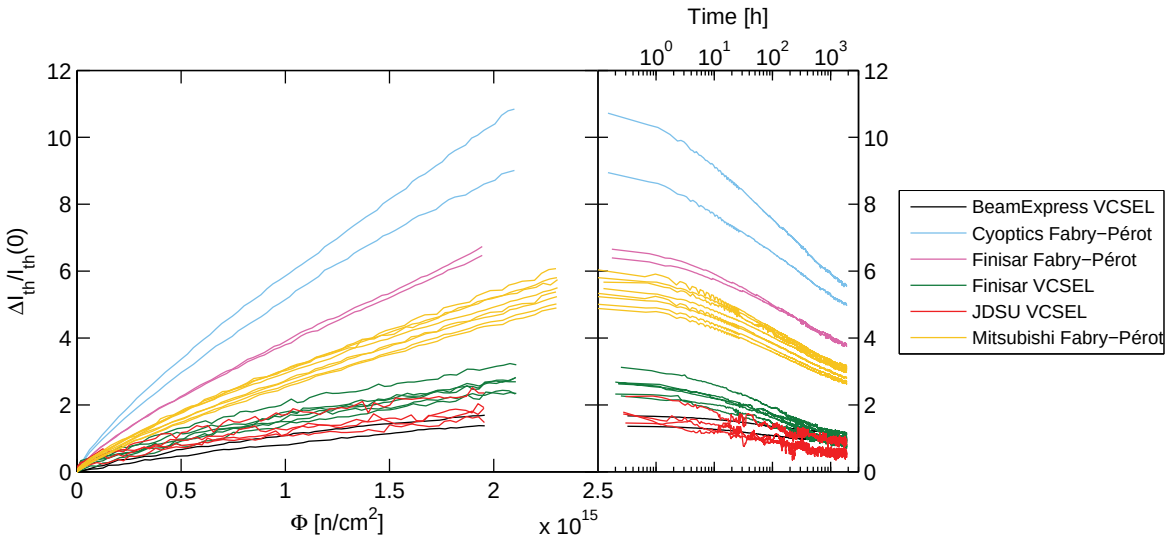

Figure 4.20: Relative laser current threshold shift versus fluence with annealing.

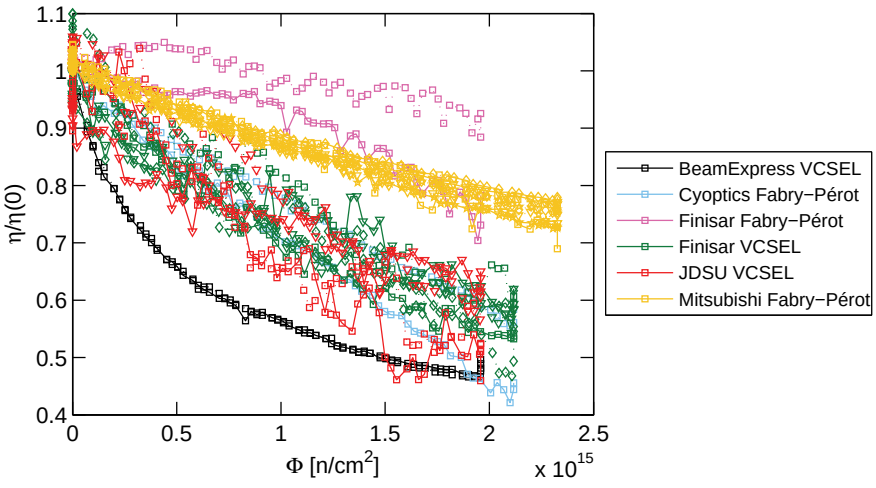

Figure 4.21: Relative laser efficiency versus fluence.

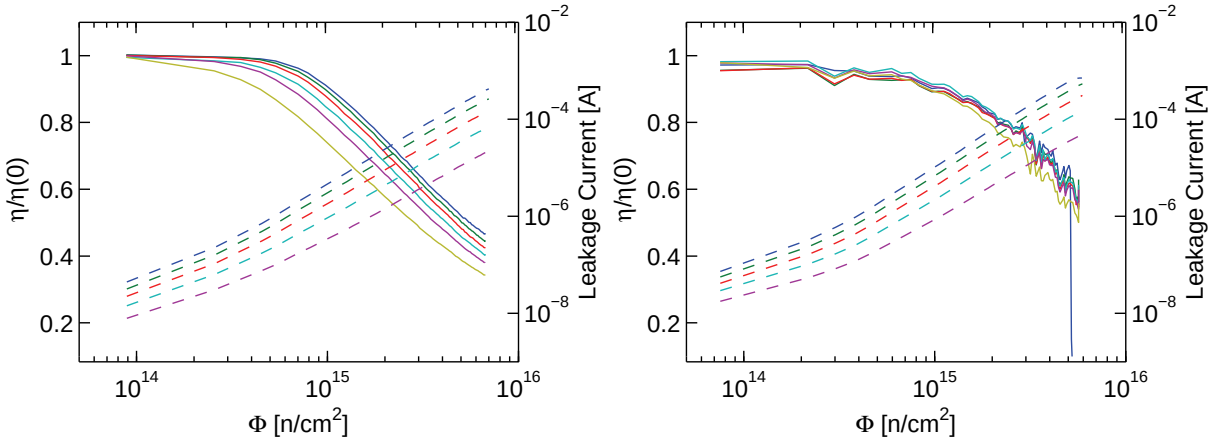

(a) Enablence 30 µ 1310 nm InGaAs p-i-n.

(b) Enablence 60 µ 850 nm InGaAs p-i-n.

Figure 4.22: Relative responsivity and leakage current for different bias voltages of selected p-i-ns with the same legend as in 4.15(d).

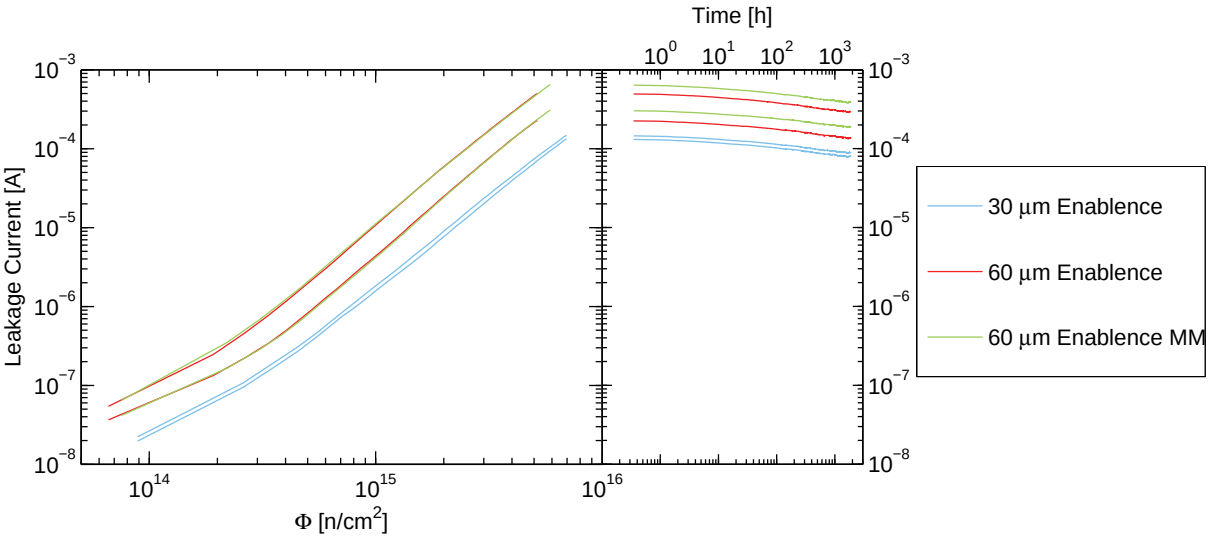

Figure 4.23: Leakage current versus fluence at 1.5 V bias with annealing.

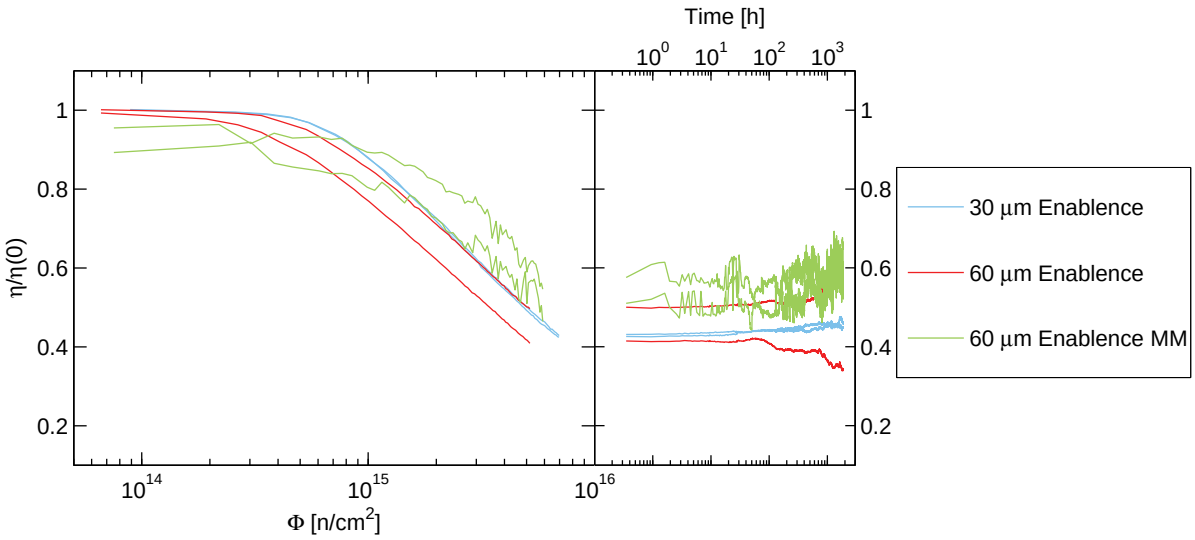

Figure 4.24: Relative responsivity versus fluence at 1.5 V bias with annealing.

Discussion

The most important outcome of this test is the discovery that only a fraction of total laser damage anneals and that the bias current does not affect the rate of the annealing. This topic is discussed more in detail in section 4.7.1 of this chapter. Concerning the p-i-n photodiodes, 60 µm Enablence InGaAs device which is capable of both 850 nm and 1310 nm was identified. Despite the higher leakage current than GaAs devices, it still looks promising due to a better radiation hardness of responsivity.

4.5 Pion results

The raw results with extracted trends of lasers and photodiodes are presented in this section for a 300 MeV/c pion test at Paul Scherrer Institut (PSI), Villigen, Switzerland.

4.5.1 PSI tests

This was the second irradiation test, much longer than the first neutron test, and lasted for about three weeks from 13/08/2010–30/08/2010 followed by two weeks of annealing. It aimed to compare the pion damage factor with respect to neutrons. As in the first neutron test, optical and electrical spectra were measured in-situ in addition to laser and photodiode parameter measurements.

Device assembly

A completely different device arrangement was used in this test as the beam time was shared with other users. A schematic view of the stack is in Figure 4.25. All the devices were placed on a moving *x*-*y*-*z* table which resulted in loose optical contacts for some devices and thus much noisier measurement in comparison to neutron tests.

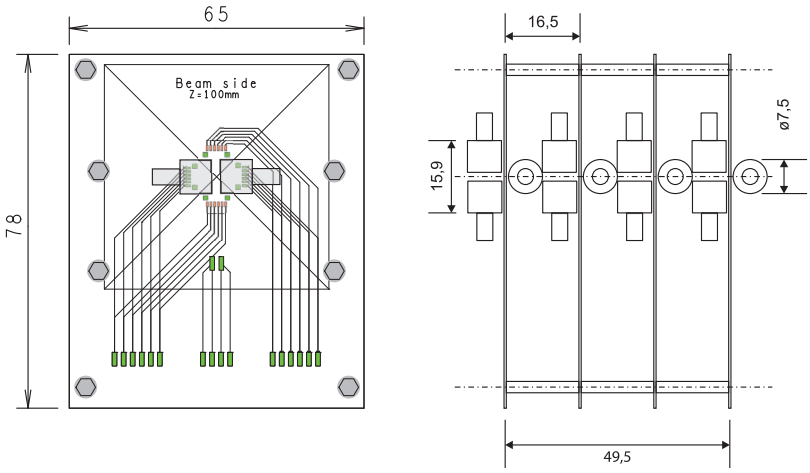

Figure 4.25: The schematic of a device stack. Due to the small beam cross section, only two devices were placed on one side of a PCB. In order to put individual boards closer together, any subsequent layer was tilted by 90° with respect to the previous one.

Laser results

A reference Mitsubishi edge-emitting laser was used also in this test. It was also one of the few devices which was destroyed by radiation. A new fast Mitsubishi 1310 nm edge-emitting laser and BeamExpress 1310 nm VCSEL with good radiation hardness were identified in this campaign. Plots of *L*-*I* and *V*-*I* curves for these three devices and a Finisar 850 nm VCSEL are in Figure 4.26. The colour code in Figure 4.26(a) corresponds to the maximum fluence of 1.7×10^{15} π/cm^2 and is the same for all plots of irradiated lasers in this campaign. The very fast drop and annealing of efficiency of the BeamExpress VCSEL is due to a lens which is used inside a laser can. This lens darkens very quickly in ionizing radiation which explains the huge drop in laser efficiency.

Comparative plots of relative threshold increase and efficiency versus fluence with annealing are shown in Figures 4.27 and 4.28, respectively.

Photodiode results

In contrast to a first neutron test, only few p-i-n photodiodes were irradiated this time. One of them was the reference Fermionics photodiode. Plots of the leakage current and relative responsivity for all p-i-n devices are in Figures 4.29 and 4.30, respectively.

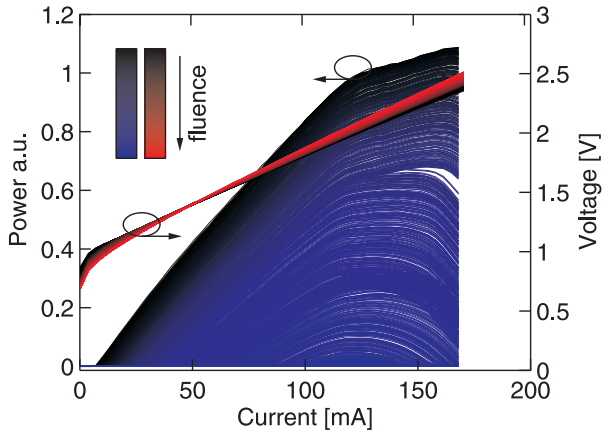

(a) Mitsubishi reference Fabry-Pérot laser with a common colour code corresponding to a maximum fluence of 1.7×10^{15} π/cm^2

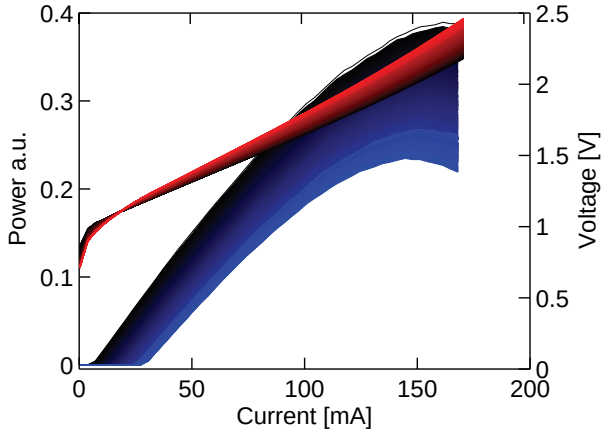

(b) Mitsubishi Fabry-Pérot laser.

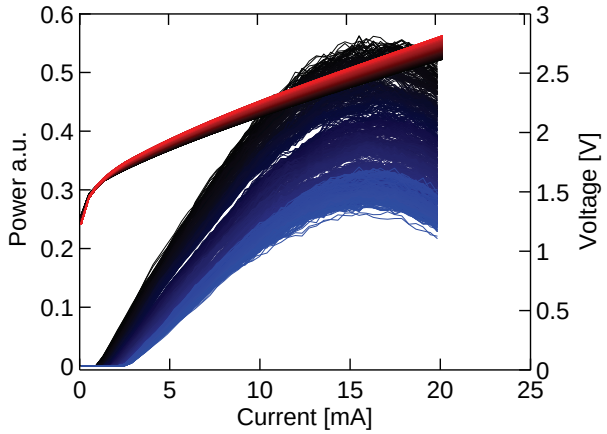

(c) Finisar VCSEL.

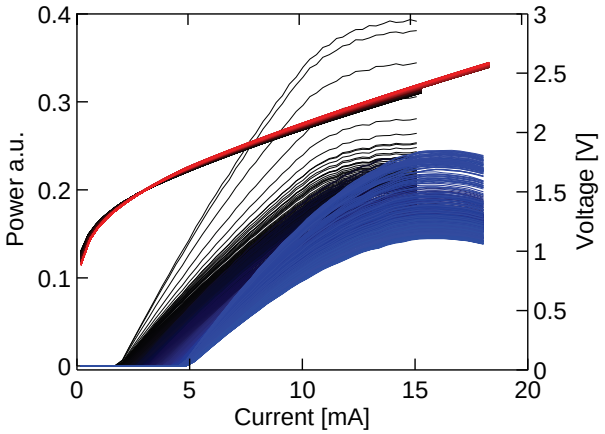

(d) BeamExpress VCSEL.

Figure 4.26: Set of *L-I* and *V-I* curves of pion irradiated lasers.

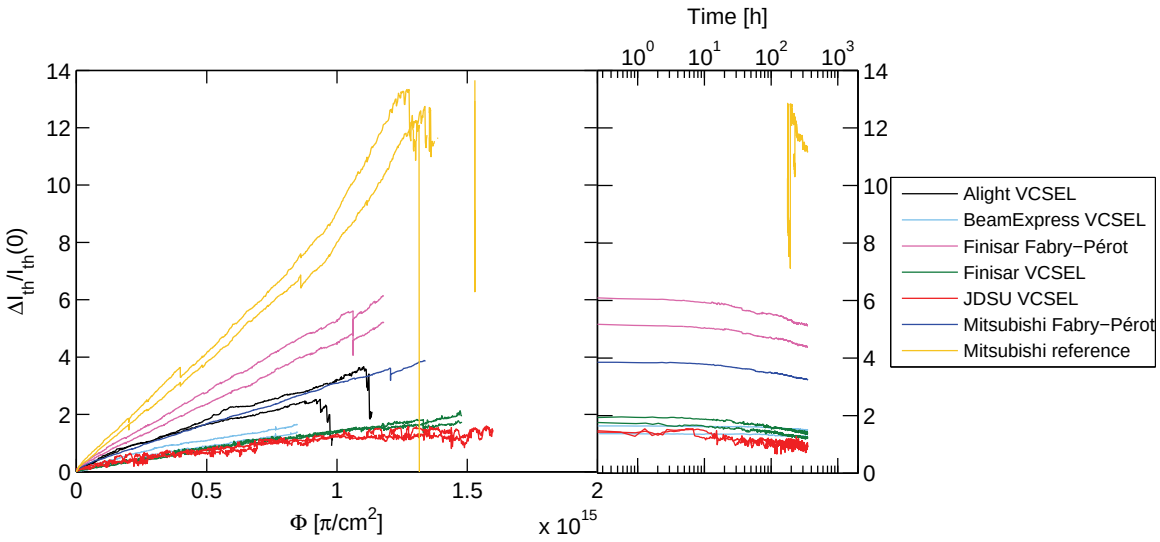

Figure 4.27: Relative laser current threshold shift versus fluence with annealing.

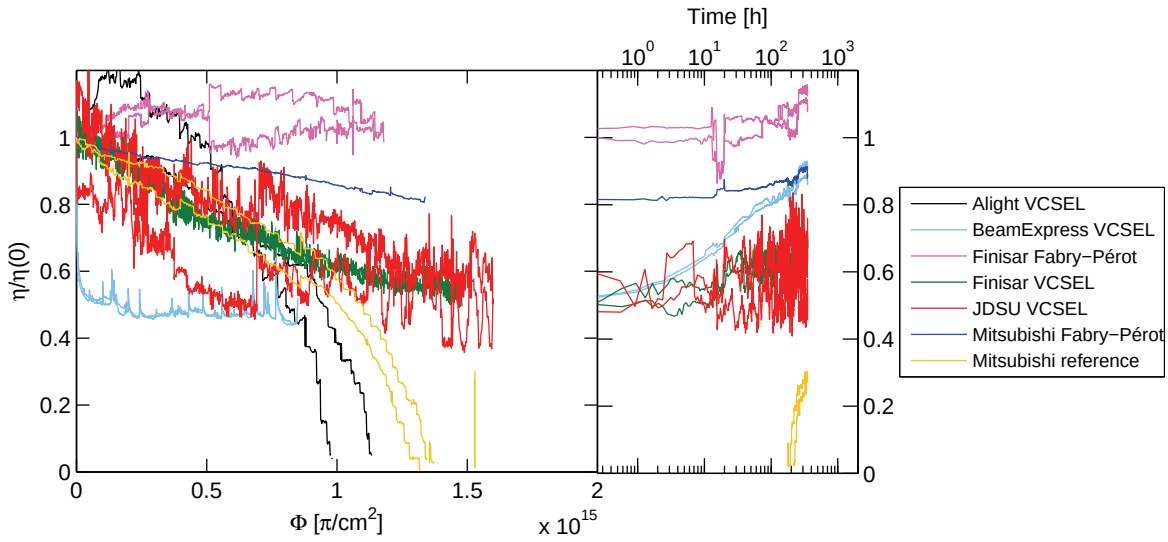

Figure 4.28: Relative laser efficiency versus fluence with annealing.

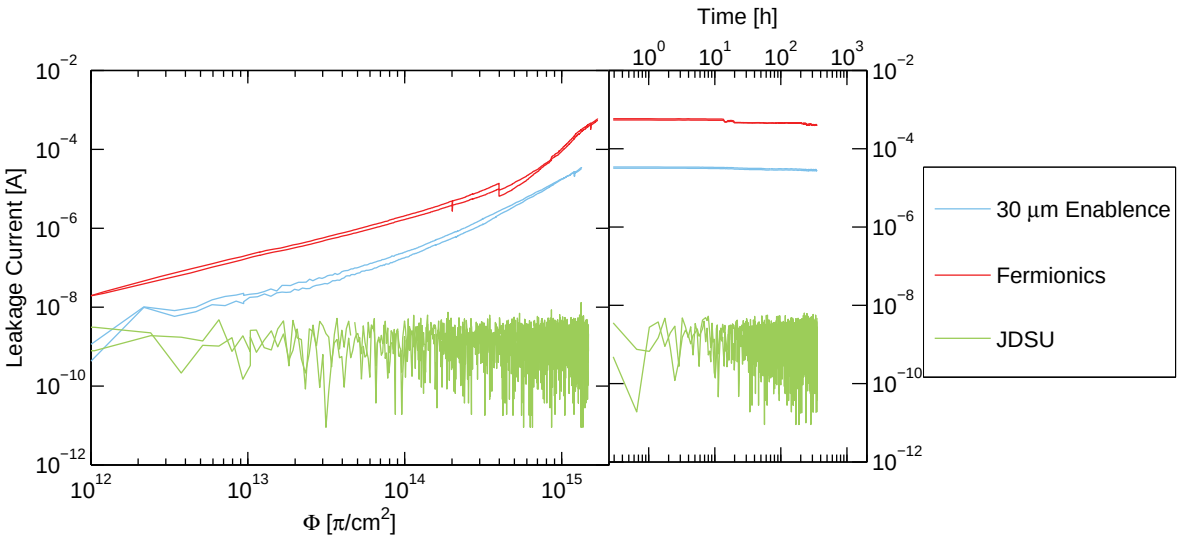

Figure 4.29: Leakage current versus fluence at 2.0 V bias with annealing.

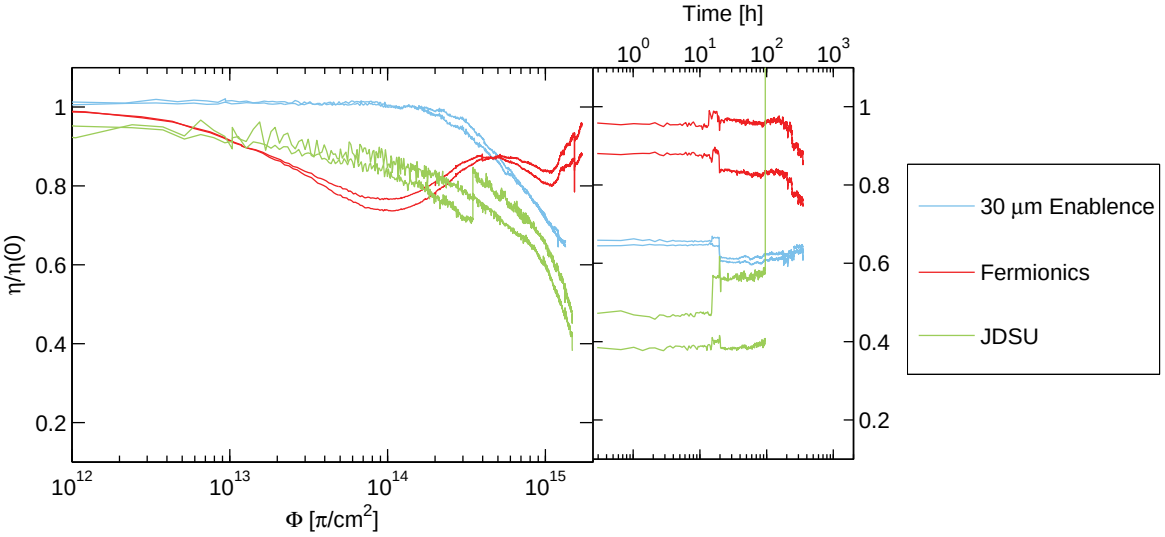

Figure 4.30: Relative responsivity versus fluence at 2.0 V bias with annealing.

Discussion

This test served as source comparison between 20 MeV neutrons and 191 MeV pions. Despite the connection problems due to a moving table and frequent beam interruptions, a representative set of data both for lasers and p-i-n photodiodes was obtained.

Optical and RIN spectra were measured for the first time in this campaign. Optical spectra results were meant to be used for a temperature characterisation of the lasers [10]. For this reason the whole laser stack was put into an oven with controllable temperature prior the test. Unfortunately, probably due to a bad handling and a subsequent ESD almost all the lasers were destroyed just before the test. This oven test was never attempted again. The purpose of the RIN spectra measurement was to determine the degradation of the bandwidth of the laser with irradiation. It was found that the bandwidth is preserved as long as enough current is injected above the laser threshold. Section 4.6 deals with spectra measurement more in detail.

4.6 Spectral measurements

As mentioned in previous sections, spectra were measured during the pion and the last neutron test. Spectra measurement always took place after the p-i-n photodiode scan. Due to a large number of devices, spectra were recorded only at four different laser currents. These currents were equidistant points between 10 % and 90 % of the output light power. The routing of light to a spectrum analyser was done by a single-mode switch, see Figure 4.5. For multi-mode fibres, an attenuation of ≈ 23 dB was observed.

4.6.1 Optical spectrum measurement

Optical spectra were recorded for all lasers in order to characterize thermal effects. The output of this measurement was a wavelength shift versus the input power. A wavelength shift of a gain envelope was measured for the edge-emitting lasers and VCSELs. The resulting slope of this trend is constant for all lasers, Figure 4.32, which suggests that the thermal resistance of the lasers did not change. Since the thermal characterisation of lasers was not performed in the lab prior the test, the absolute junction temperature cannot be determined. The method of the thermal correction of lasers is discussed in section 4.8.1.

4.6.2 Relative intensity noise measurement

The measurement of laser intensity noise was performed only for 1310 nm lasers. The attenuation of 850 nm lasers was too big as the signal was well below the noise floor of the instruments. The bandwidth of the measurement was limited to 12.5 GHz which was the cut-off frequency of an optical-to-electrical converter. All newly tested lasers except BeamExpress 1310 nm VCSEL were

much faster than the bandwidth limit of the instruments, thus any intensity noise peak was not registered.

The aim of the RIN measurement was the laser parameter extraction, as described in section 2.2.2. Due to the bandwidth problems and wavelength restrictions this was not realized after all.

Recorded intensity noise for the BeamExpress 1310 nm VCSEL for four different currents before and after neutron irradiation is in Figure 4.31. The origin of the peak for a 9 mA curve is probably some disturbance as it was not observed in subsequent measurements. Resonance frequency for higher currents above threshold is attenuated by the insufficient bandwidth of optical-to-electrical converter.

A plot of the position of the intensity noise peak during irradiation is in Figure 4.33. Since the peak remains at the same frequency during irradiation, the bandwidth of the laser does not decrease during irradiation as long as enough modulation current can be injected above threshold.

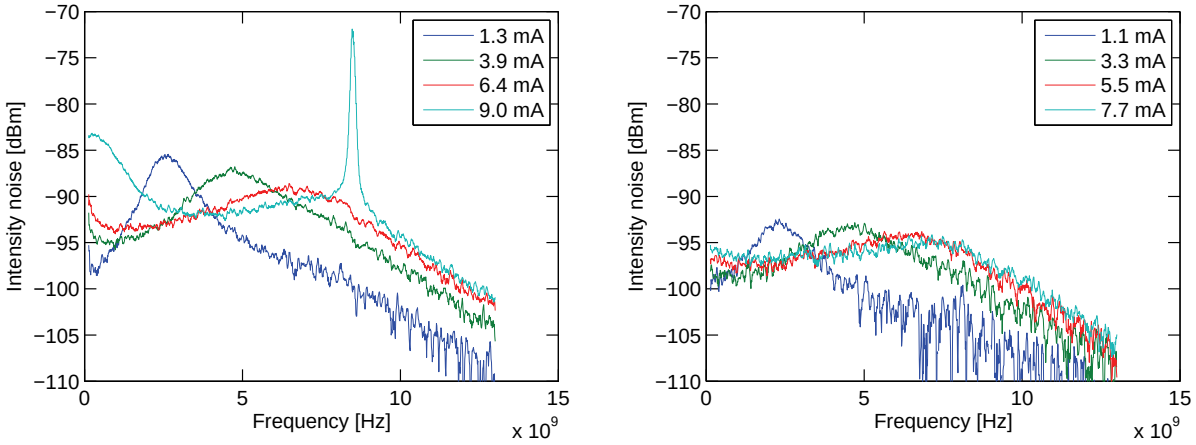

(a) before irradiation

(b) after irradiation

Figure 4.31: Intensity noise of a BeamExpress VCSEL for four different currents above threshold.

4.7 Laser modelling and parameter extraction

Rate-equations were chosen for a description of measured *L-I* curves of a laser during irradiation due to their relative simplicity and also efficiency. They have been described in chapter 2. The modified rate-equation which models even a non-linear part of a *L-I* curve is derived in this section. Its robustness is tested on experimental data measured during the first neutron test.

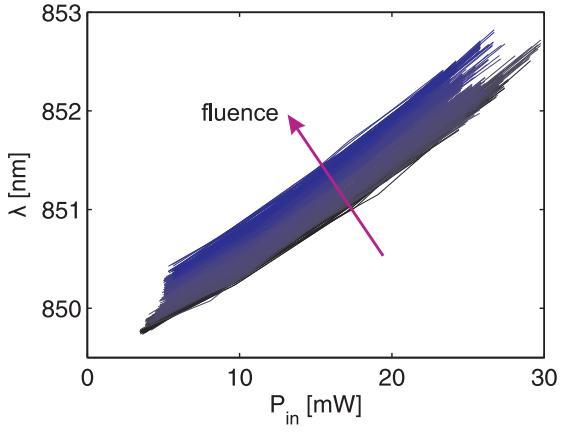

Figure 4.32: Peak wavelength versus input electrical power of a 850 nm VCSEL during irradiation.

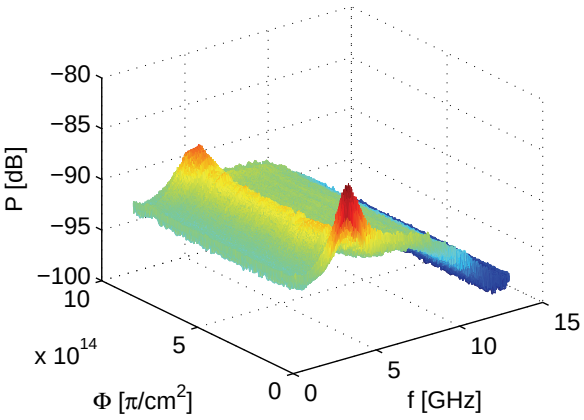

Figure 4.33: Intensity noise of a BeamExpress 1310 nm VCSEL for 3.7 mA bias during irradiation.

4.7.1 Rate-equation Model

As stated in section 2.2, single-mode steady-state operation rate-equations are often used to model semiconductor laser characteristics. They are also applicable to multi-mode operation with a limited number of modes with relatively similar properties. The model describes the spontaneous- and stimulated-emission regions of laser operation and takes into account thermal rollover effects. In order to minimize the number of free parameters and to facilitate numerical solving of the equations, these are normalized and new dimensionless quantities are introduced instead of real physical constants, which are unknown and can differ by several tens of orders of magnitude.

Theory

Rate-equations in normalized form (2.12) and (2.13) were introduced in section 2.2. In order to model the thermal roll-over of semiconductor lasers, the linear gain term $G(n) = kn$ was modified to:

$$G(n,J) = G_0\left(n - n_0 J^l\right), \tag{4.2}$$

where G_0, n_0 and l are constants. The current dependency J^l in the gain term takes into account non-linear effects such as Auger recombination and the leakage of carriers out of the active region. The modified rate-equations become:

$$j - N - p\left(\frac{N}{1-a} - \frac{aj^l}{1-a}\right) = 0 \tag{4.3}$$

$$p\left(\frac{N}{1-a} - \frac{aj^l}{1-a} - 1\right) + \beta_{sp}N = 0, \tag{4.4}$$

where $a = n_0\gamma_e J_{th}^{l-1}$. Setting $l = 0$, the same *L-I* curves without a thermal rollover are obtained as from the equations (2.12) and (2.13).

Comparison with experimental data

In order to verify the applicability of the rate-equation model, the calculated operating characteristics of a semiconductor laser are compared to experimental data obtained during the first high-fluence 20 MeV neutron test.

A fluence-dependent set of model parameters can be calculated using a two-step fitting of measured light-current (*L-I*) characteristics of a laser that underwent irradiation. Trends like laser threshold, quantum- and slope-efficiency are extracted and based on their behaviour the device operation during extended irradiation can be predicted. Good agreement between the calculated and measured values was reached for different technology devices in both spontaneous and stimulated emission regions of operation. Figure 4.34 shows the fitted data of a Mitsubishi CMS reference laser.

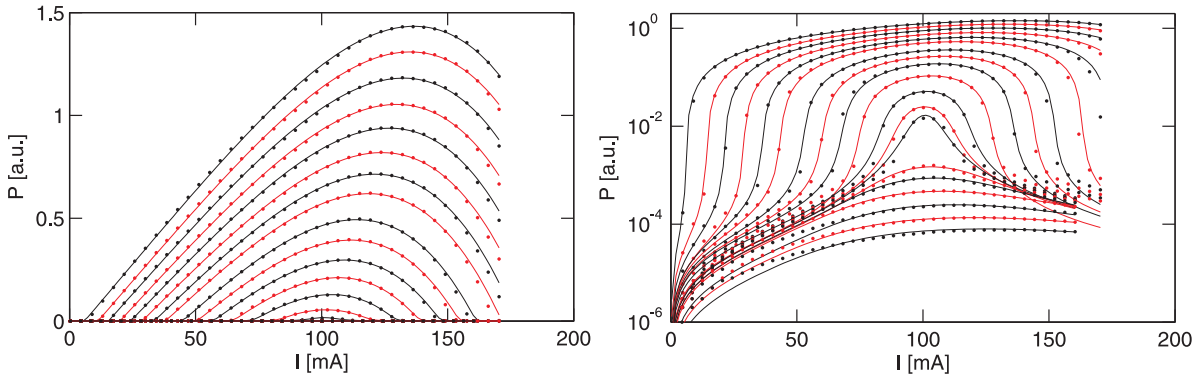

(a) linear scale (b) log. scale

Figure 4.34: Fitted curves for 1310 nm Mitsubishi CMS reference laser in linear and log. scale.

The introduction of a gain term in the form of equation (4.2) is purely empirical. The addition of only two extra parameters into the rate-equations describes the whole operating region of a laser, even when the laser stops lasing due to radiation damage. This approach is more convenient than others mentioned in chapter 2.2 as it uses a minimum set of parameters which facilitates fitting of measured *L-I* curves. More complex models could be employed, but they would require at least some insight into the device composition which is not the case for the commercial devices that are used in the irradiation tests.

4.8 Comparison of neutron and pion sources

Thanks to the three irradiation tests that were performed, the comparison between neutron and pion sources is possible. As mentioned in the beginning of this chapter, it is very difficult to analytically compare the radiation damage factors of these two sources for complex semiconductor compounds; it was thus measured. The measured damage factors are compared to the simulated ones.

4.8.1 Laser results

Since the environmental parameters were not the same in both tests, some corrections have to be made prior to the fluence scaling. Due to a different board occupancy in pion and neutron tests, the temperature profile was not the same. As can be seen from Table 4.5, the beam flux was also very different.

Temperature correction

None of the devices which underwent the test were cooled; the temperature thus increased during irradiation as more heat was dissipated. The threshold current of an edge-emitting laser varies with temperature T as:

$$I_{\mathrm{th}}(T) = I_0 \, \mathrm{e}^{T/T_0} \tag{4.5}$$

where I_0 is a constant and T_0 is a characteristic temperature. Writing the equation (4.5) for two different temperatures T_1 and T_2 and dividing them, laser threshold current scales with temperature as:

$$I_{\mathrm{th}}(T_2) = I_{\mathrm{th}}(T_1) \, \mathrm{e}^{(T_2 - T_1)/T_0} \tag{4.6}$$

The equation (4.6) was used to scale all data to a room temperature of 300 K.

One of the issues that remains to be solved is the exact value of T_1. In the first approximation, this temperature correction was made to devices which were close to the ambient temperature sensors. If the junction temperature, measured from the optical spectrum, scales with the ambient temperature, i.e. thermal resistance of the laser device remains the same during the irradiation, the obtained threshold trend is just a multiple of the true value. In other words, this correction does not affect the shape of the trend. The error of this correction factor is estimated to be less than the error of the fluence measurement.

The temperature correction for VCSELs was not done for two reasons. First, measured data were quite noisy, which would make any temperature correction impossible by itself, and second, the injected current is basically ten-times smaller than in edge-emitting lasers, thus the internal heating is not noticeable.

Figure 4.35 shows the temperature correction applied to one of the lasers which were placed close to the platinum PT100 sensor. The temperature resistance of this particular device was not changing during irradiation which means that the junction temperature is just a multiple of a measured temperature. The direct proportion between measured temperature and junction temperature is demonstrated in Figure 4.37. The regression of the peak wavelength λ determined from the optical spectra measurement is linear with measured temperature T for different input powers.

The correct value of the junction temperature can be obtained by a measurement of the thermal resistance of the lasers, which was meant to be done prior to the pion test, or possibly even by a simulation. Since the measured data can be corrected even without this knowledge, it turns out that the exact value of the junction temperature is redundant.

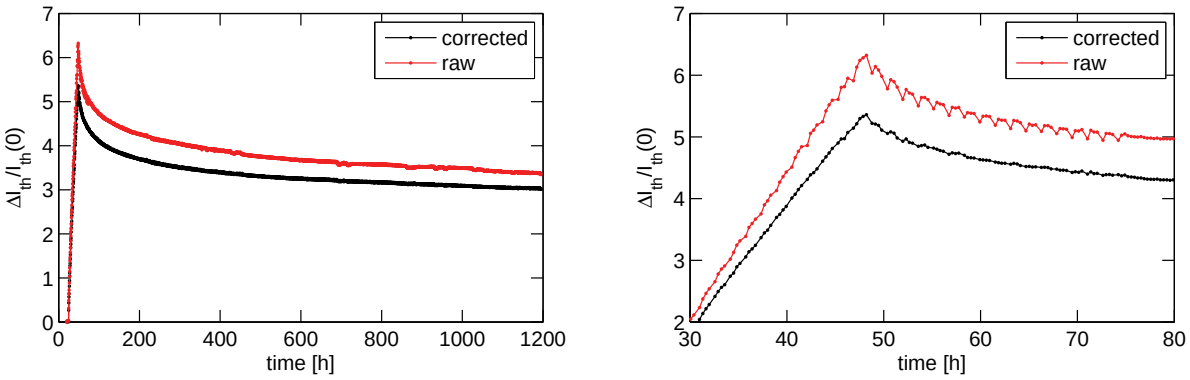

(a) full-scale view (b) zoomed view

Figure 4.35: Relative threshold increase versus time with temperature correction of the Mitsubishi 1310 nm laser.

Applying the temperature correction to the laser threshold trends, the effect of different bias current can be investigated. As can be seen from Figure 4.36, the bias current does not affect the rate of the annealing.

This surprising result can be explained by the assumption that the rate of annealing depends only on temperature and not on current density. If a change of the rate of annealing on bias current is indeed observed, it is probably due to internal heating caused by excessive current injection and not by the current itself. Since the heat transfer between the laser junction and the laser can was adequate in the irradiation tests in question, as can be seen from optical spectra measurements, no change of the rate of annealing is observed.

Flux correction

Another correction that has to be made prior to the comparison of neutron and pion radiation damage is the scaling of the flux. The reason for this correction is that the lasers are constantly annealing. From the measured data it is obvious that only a fraction of the total damage anneals. This saturation of laser annealing can be described by the following exponential equation:

$$A(t-t_0) = (1-c)\,\mathrm{e}^{-\lambda(t-t_0)} + c, \quad t \geq t_0, \tag{4.7}$$

where λ is a decay constant and c a saturation fraction.

Supposing that defects created by irradiation decay independently, the irradiation period can be divided into infinitesimal time steps during which defects are created and then anneal. For a discrete defect creation rate $q(t_i)$ and the annealing function $A(t)$, the threshold current increases and anneals in time as:

$$I_{\mathrm{th}}(t-t_0) = I_{\mathrm{th}}(t_0)\left(1 + \sum_{i=0}^{n} q(t_i)(t_{i+1}-t_i)A(t-t_i)\right), \quad t \geq t_0. \tag{4.8}$$

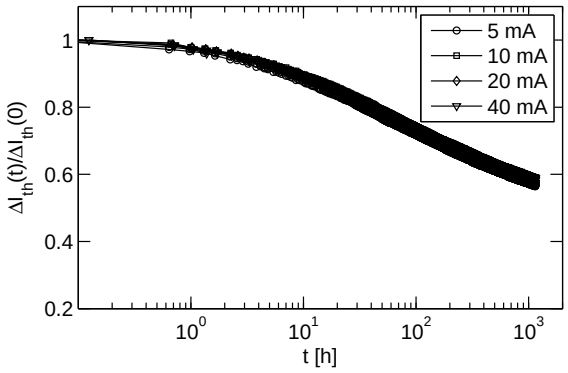

(a) Mitsubishi Fabry-Pérot laser.

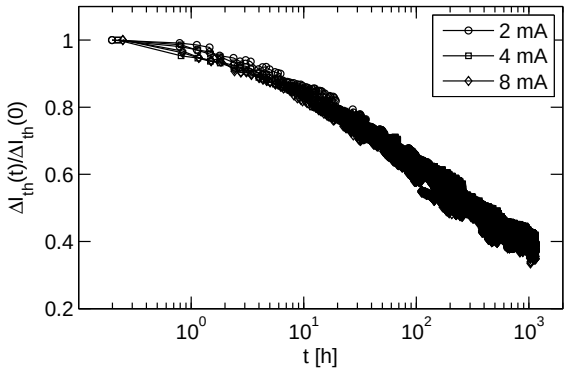

(b) Finisar VCSEL.

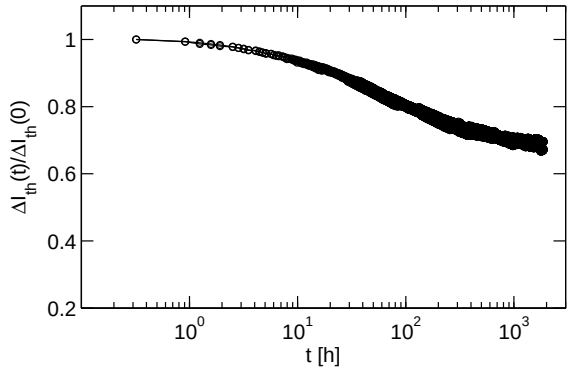

(c) BeamExpress VCSEL.

Figure 4.36: Fraction of remaining defects versus time for different bias currents above laser threshold (two devices per bias current group).

Equation (4.8) with the annealing function (4.7) describes the irradiation period quite well but when the beam is turned off, $q(t) = 0$, it predicts a faster decay than observed. Adding at least three terms (4.7) with different decay constants partially solves this problem, but still a sufficient match to the measured data is not achieved.

Another possibility is that defects do not anneal by a simple exponential law, or they do but with an infinite number, or rather a spectrum, of decay constants, and the annealing should be modelled differently. The easiest way which also produces the best results is to use a so-called *hill function* as the annealing function:

$$A(t-t_0) = 1 - \frac{(1-a)(t-t_0)^k}{c+(t-t_0)^k}, \quad t \geq t_0, \tag{4.9}$$

where a, c and k are constants. This function is often used in mathematical modelling of processes which exhibit an S-shaped curve. It fits measured data perfectly, however it does not have any physical meaning.

Figure 4.38 compares fitting measured annealing data of a Mitsubishi laser after temperature correction with equations (4.7), (4.9) and a simple exponential decay. The advantage of the hill

equation is evident.

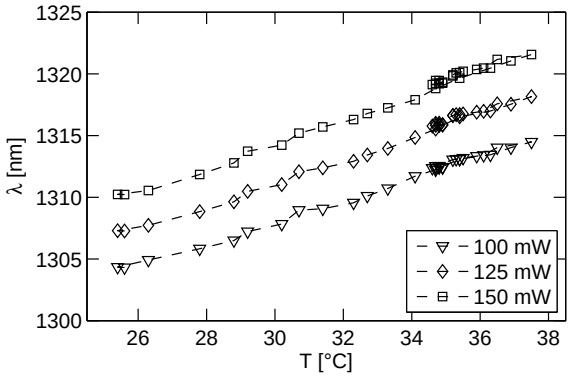

Figure 4.37: Peak wavelength shift versus measured temperature for three different input powers of a Mitsubishi laser.

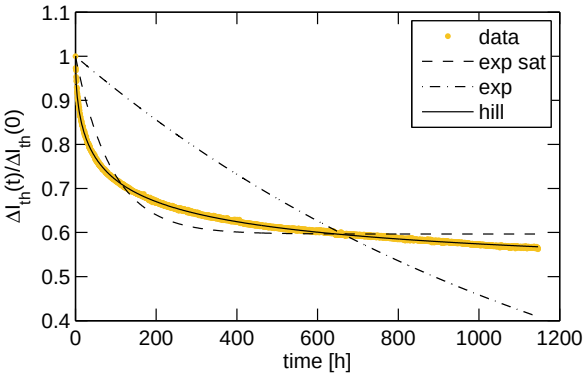

Figure 4.38: Comparison of three fitting methods using equations (4.7), (4.9) and a simple exponential denoted 'exp sat', 'hill' and 'exp', respectively.

Using equation (4.9) instead of equation (4.7) for a description of the annealing formalism (4.8), a fit of measured data of the relative threshold increase for both irradiation and annealing periods is obtained, as illustrated in Figure 4.39.

Knowing the fitting constants of the fit in Figure 4.39, the relative threshold increase can be modeled for any beam flux $q(t)$. Taking the beam characteristics from the pion irradiation and putting them together with the fitting parameters, the relative threshold increase versus fluence for a neutron beam with the same flux as the pion case can be calculated.

Figure 4.40 shows the comparison of a neutron and pion damage for the same beam flux for several laser devices. The scaling factor between neutrons and pions is summarized in Table 4.8.

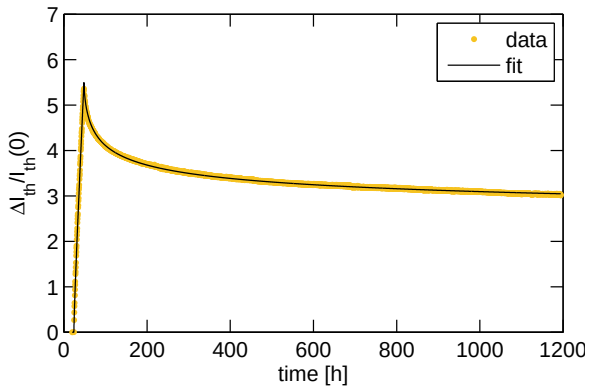

Figure 4.39: Fitted measured data of a relative threshold increase versus time of a Mitsubishi laser.

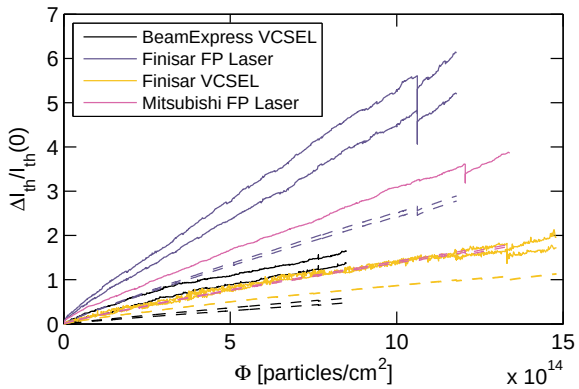

Figure 4.40: Comparison of a relative threshold increase of various laser devices for neutrons, dashed line, and pions, solid line, with the same beam flux.

Comparing these values with the simulated ones in section 4.1.1 a reasonable match is obtained. This match could be possibly further improved by knowing the exact stoichiometry and by reducing the spread in measured trends across device families. However, to accomplish this a close contact with a manufacturer and a test with much larger device quantities would be required.

To illustrate the prediction capabilities of this method, Figure 4.41 shows measured and calculated remaining fraction of damage of a Mitsubishi laser. The fitting parameters are taken from neutron test data and are put into an equation with the pion beam flux profile. The slower annealing, which was measured during the pion test, is well modelled and there is a match between calculated and measured data.

Device	Factor
BeamExpress VCSEL	2.8
Finisar FP laser	2.1
Finisar VCSEL	1.9
Mitsubishi FP laser	2.4

Table 4.8: The scaling factor between neutrons and pions for different laser devices.

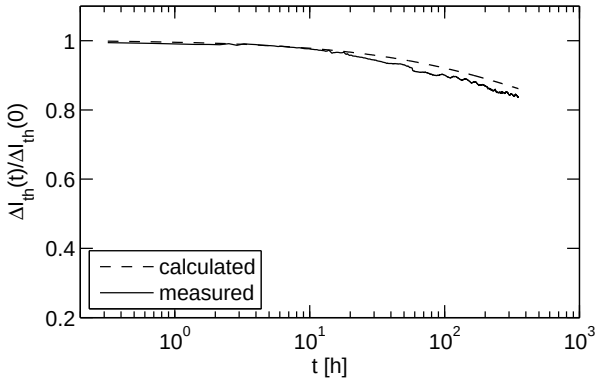

Figure 4.41: Fraction of remaining damage versus time for measured and calculated trends.

4.8.2 Photodiode results

As mentioned previously, photodiodes do not recover significantly, i.e. the radiation damage is permanent. Only a small fraction of photodiode leakage current anneals. This fact also facilitates the comparison between the two sources, which can be direct. As the photodiodes are passive devices, temperature correction is not needed either.

The comparison of photodiode leakage current and relative responsivity for one device which underwent both tests is in Figures 4.42 and 4.43, respectively. The scaling factor for both leakage current and relative responsivity is 2.2.

4.9 Prediction of radiation damage in-system

Combining the laser device modelling with the laser annealing description, the prediction of laser behaviour becomes possible, provided that the beam intensity is known. Since all measured parameters of the lasers anneal uniformly, as is demonstrated on measured *L-I* curves which

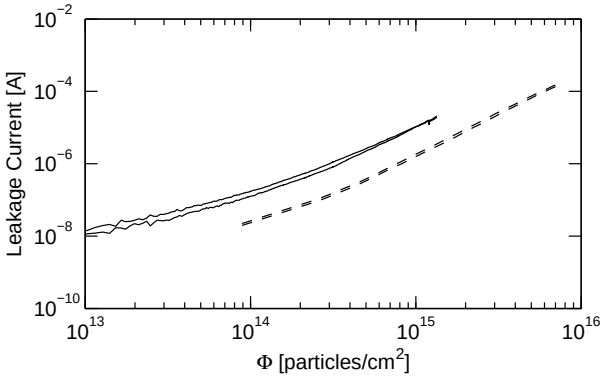

Figure 4.42: Comparison of a leakage current versus fluence for pions, solid line, and neutrons, dashed line, of an Enablance 30 µm device at 1.5 V bias.

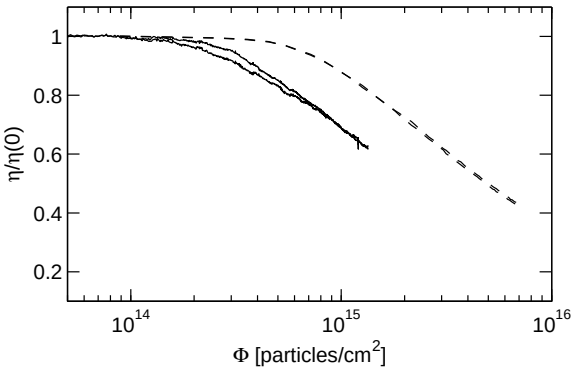

Figure 4.43: Comparison of a relative responsivity versus fluence for pions, solid line, and neutrons, dashed line, of an Enablance 30 µm device at 1.5 V bias.

during the annealing period simply follow the curves measured during irradiation but in the reverse direction, one set of laser parameters is sufficient. Given the flux time profile, it is thus sufficient to predict just one laser parameter. This parameter is usually the laser threshold.

4.9.1 Laser End-of-Life Prediction

Using the rate-equation model, it is possible to predict the device behaviour from low-fluence data. Data from a Finisar 1310 nm Fabry-Pérot laser in the first neutron test are used as a demonstration. Fitted rate-equation model parameters from low-fluence data (below 5.0 × 10^{14} n/cm^2) were extrapolated and then used to predict laser *L-I* curves as depicted in Figure 4.44. The fitted curves were extrapolated to a point where a laser stops lasing due to thermal rollover, denoted I_{ro}. The end-of-life of a laser is predicted as an intersection of I_{th} and I_{ro}. Measured values of I_{th} and I_{ro} with predicted I_{th} and calculated I_{ro} are in Figure 4.45.

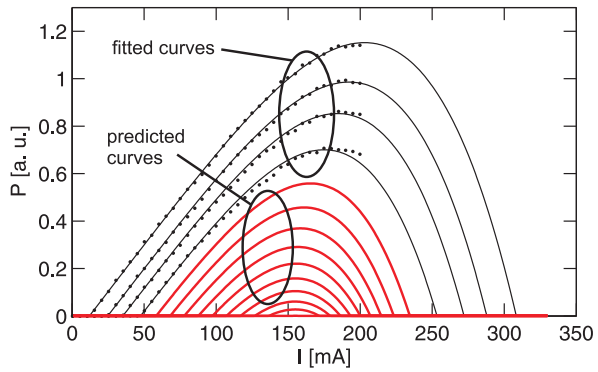

Figure 4.44: Fitted and predicted *L-I* curves of a Finisar 1310 nm Fabry-Pérot laser.

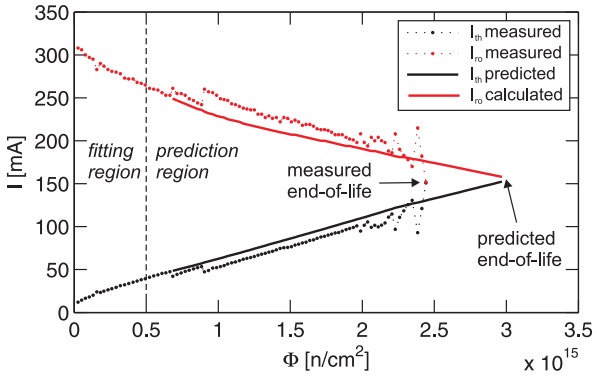

Figure 4.45: Measured and predicted I_{th} with calculated I_{ro} for a Finisar 1310 nm Fabry-Pérot laser.

4.9.2 Radiation damage prediction in p-i-n photodiodes

Unlike lasers, damage to p-i-n photodiodes cannot be predicted from low fluence measurements. This is due to an unpredictable decrease in responsivity occurring at certain fluence which varies from type to type. However, after this dramatic change the responsivity of a p-i-n photodiode decreases exponentially (linearly in logarithmic scale) for most photodiode types. The damage prediction is made by simple linear extrapolation on a log. scale. This is well demonstrated in Figure 4.46. This method cannot be employed for every device, unfortunately. One example is the Fermionics photodiode (Figure 4.47) currently used in CMS which was also used as a reference device in radiation tests described in Chapter 4.

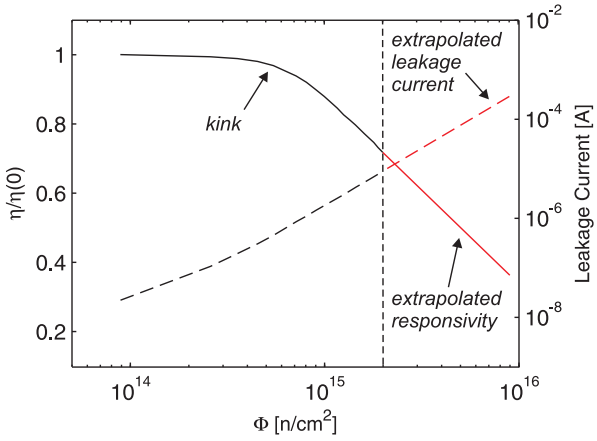

Figure 4.46: Linear extrapolation of relative responsivity and leakage current of InGaAs p-i-n to higher fluences.

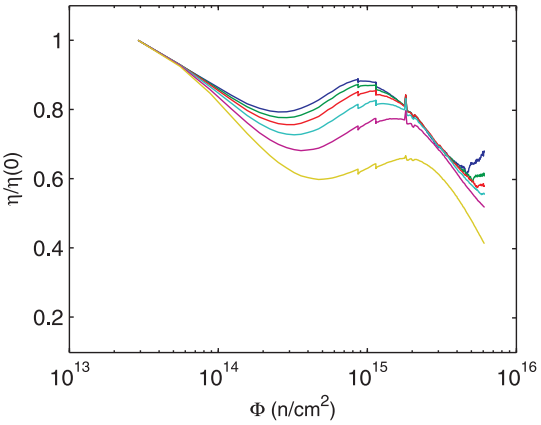

Figure 4.47: Relative responsivity for different bias voltages versus fluence of a reference Fermionics p-i-n.

4.10 Discussion

A large number of devices were tested in three different irradiation campaigns. Several candidate devices, operating at both 850 and 1310 nm wavelengths, for the Versatile transceiver were identified. The results of all tests confirmed the assumption that VCSELs are more radiation hard than edge emitting lasers. Globally, modern fast devices perform better than their predecessors which are currently used by the LHC experiments.

The irradiation of p-i-n photodiodes showed that the responsivity of InGaAs photodiodes is less affected by radiation than that of GaAs photodiodes. Concerning the leakage current, the situation is completely different. An increase in leakage current was not observed for any GaAs photodiode.

In terms of annealing, lasers are able to recover a substantial part of the induced damage. This will be significant in the final application where the irradiation to maximum fluence takes place over the system lifetime that is typically measured in years. A surprising result is that the

rate of annealing is not affected by a laser bias current which contradicts some results found in literature [11, 41]. Contrary to lasers, p-i-n photodiodes do not exhibit any significant annealing.

The proposal of using a rate-equation model to describe semiconductor laser *L-I* curves during irradiation was presented. Good agreement between the calculated and measured values was achieved for all irradiated devices in both neutron and pion tests. A compact rate-equation based laser degradation model was devised to describe both the laser degradation and the annealing period. This model has wide applicability in future irradiation test refinements as the time spent in irradiation facilities, and thus the cost, can be significantly reduced.

Scaling factors between two different particle species were obtained despite the lack of statistics, caused by the limited number of devices tested, and the uncertainty in the fluence measurement. Simulations and experimental results show that 191 MeV pions are approximately twice as damaging as 20 MeV neutrons.

One possible explanation of this fact is that neutrons, being uncharged, lose their energy in elastic collisions which are not so efficient at energy transfer unless with an equal mass particle. As a result, neutrons are not slowed down too much in the devices, hence they do less bulk damage than charged pions which can also interact electromagnetically, i.e. transfer more of their energy to the target as the electromagnetic interaction is more probable. In other words neutrons have to hit the tiny nucleus in order to interact whereas pions, being charged, interact at a longer distance.

In addition to that, pions may form resonance state with protons from the nucleus which immediately decay into a pion and proton sharing the energy of the incident pion. These two particles having lower energy than the incident pion may interact with the material. However, as tested devices are usually very thin this additional multi-scattering process will be rather unlikely.

Chapter 5

Single-Event Effects in photodiodes

This chapter deals with measuring and simulation of SEUs in photodiodes. It starts with a description of an SEU test and then proceeds to methods of SEU simulation. At the end of the chapter, simulated data are compared to measured results.

Mechanisms causing single event effects in photodiodes were briefly described in chaper 3. Concerning the prediction of SEU rates in semiconductor photodiodes, it is not well established, hence an extensive testing programme for the devices in question is usually required. The testing is typically performed in irradiation facilities using a well characterised beam of particles or ions [52, 54]. In particular, the dominant particle species of the target environment may not be readily available for testing, resulting in the need to verify the validity of the use of proxy particles that are readily available at beam facilities. Such SEU testing is rather expensive and time consuming. A complementary approach based on detailed simulation of SEU effects is presented in section 5.2.

5.1 Single-Event Effect test review

The SEU test described in this section was performed by the CERN PH-ESE-BE group at Paul Scherrer Institute (PSI) irradiation facility, Villigen, Switzerland in 2007 [52]. The SEU test was carried out at a 63 MeV proton flux of 8×10^8 p/cm^2/s in order to simulate the expected radiation environment at HL-LHC.

This test method is a further development of the original SEU test performed by F. Faccio et al. at an irradiation facility in Louvain-la-Neuve in 2000 [30], where the *Device Under Test* (DUT) was a Fermionics InGaAs photodiode of the type used in the CMS Tracker. The photodiode was irradiated by 59 MeV protons followed by 32 MeV and 62 MeV neutrons. For comparison, the proton-induced SEUs were simulated using a modified version of FLUKA code. Despite some disagreements between simulated and measured data, the authors claim that the simulation confirmed their understanding of a contribution of direct and secondary ionization to the measured bit-error cross-sections for different angles of incidence.

The irradiation setup of the recent SEU test is shown in Figure 5.1. A stream of pseudo-random data generated in a dedicated FPGA was fed to a laser driver for conversion to an optical signal. This optical signal was attenuated and sent to DUTs placed on an irradiation board, while its optical power was measured by a power-meter. The electrical signal from the photodiodes was amplified by a *Transimpedance Amplifier* (TIA) and sent back to the FPGA. The incoming data stream from the photodetectors was compared to the original signal and if a mismatch was detected, the error pattern was recorded. The SEU test was carried out for three data-rates of 1.5, 2.0 and 2.5 Gb/s and four angles of incidence of 0°, 10°, 80° and 90°, where 0° corresponds to normal incidence and 90° to grazing incidence.

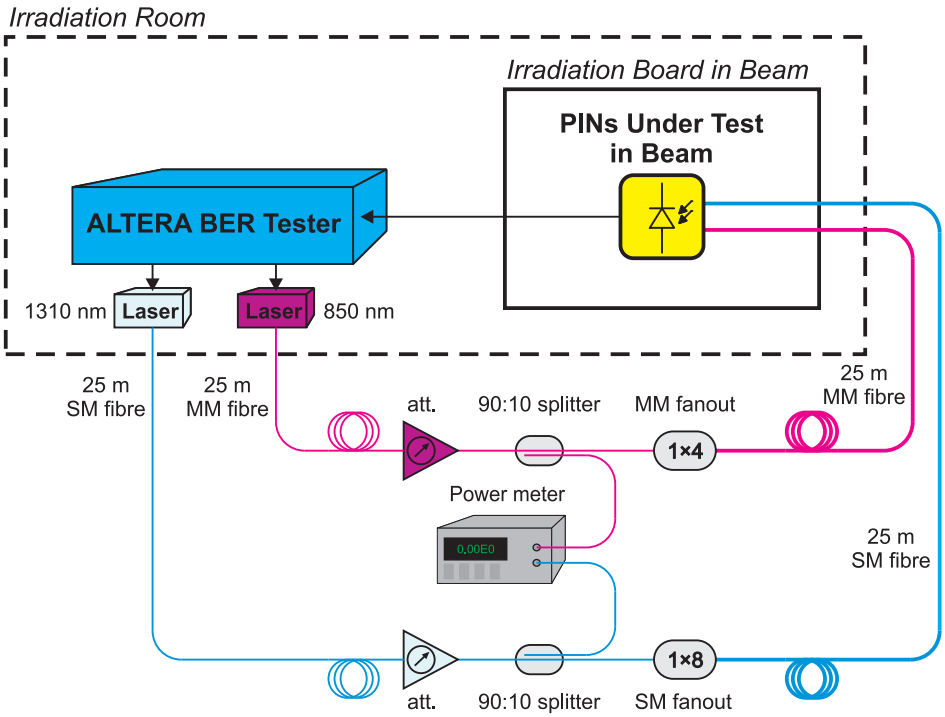

Figure 5.1: Setup for the proton irradiation test in PSI. Two lasers of 1310 and 850 nm were used as a source for p-i-n photodiodes. The intensity of both lasers was measured by an optical power meter.

For every combination of the selected data rates and angles of orientation, attenuation scans monitoring the *Bit-Error Rate* (BER) were systematically performed both with the beam on and off, to be able to distinguish errors caused by SEUs from those due to electrical and environmental noise.

The measured BER of one of the devices versus the *Optical Modulation Amplitude* (OMA) of the signal for two different angles of incidence is shown in Figure 5.2. There are two clearly distinguishable regions: one for the lower OMA, which is noise dominated and which corresponds to a beam-off measurement, and another which is dominated by radiation induced errors. The higher BER for grazing angle incidence is caused by the longer interaction length of the proton traversing the sensitive region of the photodiode. These two curves for different incidence angles are expected to merge into one for higher OMA, where the high energy loss due to nuclear interactions occurs. This process is essentially independent of angle for a thin target, which is the case for a photodetector.

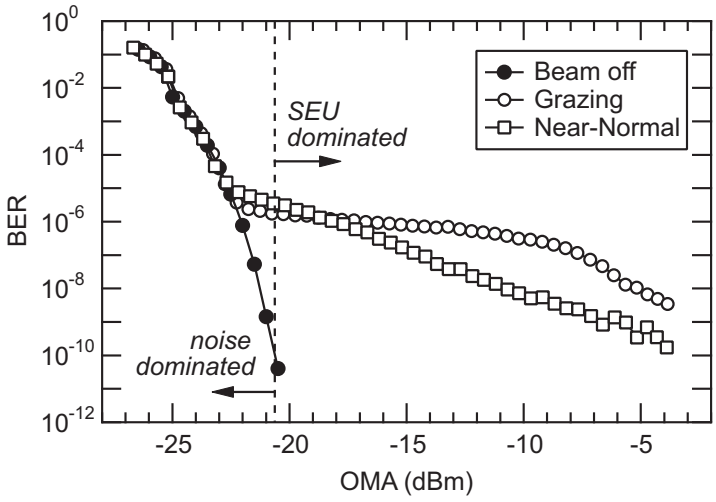

Figure 5.2: Illustration of the effect of the proton beam for two different incident angles of 10° and 90° on the observed BER with respect to beam-off data (picture taken from [52]).

The plots similar to that of Figure 5.2 were measured for all devices at all incidence angles and data-rates. The *bit-error cross-section*, which is simply a measure of the probability that an interacting particle causes an upset, was determined together with the statistics of the error bursts. Using the following relationship:

$$\text{BER} = \frac{\sigma \times \varphi}{R} \tag{5.1}$$

between bit-error cross-section σ, average particle flux φ and data-rate R, one can easily calculate the BER of the system directly from the bit-error cross-section curves for any flux of interest.

The outcome of the test was the detailed characterization of bit-error cross-section for various devices and confirmation of higher error cross-sections for angles near grazing incidence. From recorded error pattern statistics one can show that multiple bit errors can occur in optoelectronic receivers even with transitions from logical '1' to logical '0'. The error bursts could originate in the attached circuitry, mainly by the response of the TIA and limiting amplifier. The detailed knowledge of these error bursts will allow design of robust *Forward Error Correction* (FEC) codes to mitigate errors in a data transmission chain.

5.2 Simulating Single Event Upsets in Photodetectors

A method to estimate Single Event Upset effects in photodetectors using GEANT4 is presented in this section. Individual interactions of protons, π^+ and neutrons with matter in the sensitive volume of a p-i-n diode are simulated with GEANT4 for various angles of incidence. The total energy deposit in the sensitive volume, as output by GEANT4 simulation, is related to an equivalent optical pulse and the bit-error cross-section is calculated. Comparison of the proton, π^+ and neutron bit-error cross-sections demonstrates that protons are appropriate candidates as proxies for Single Event Upset tests to determine the SEU-rate in HL-LHC environments. The simulated proton bit-error cross-section is compared to the measured data.

5.2.1 Energy deposition model

For the sake of calculations, one can assume that the SEU occurrence depends on two parameters of the device: the *sensitive volume* in which the energy must be deposited, and the *critical energy*, E_{crit}, that must be exceeded in order to upset the device for a given amplitude of optical signal. The sensitive volume was assumed to have sharp boundaries and E_{crit} was determined by a dedicated *Pulse Injection Test*, described below.

The distribution of total energy deposited in the sensitive volume of the photodiode was simulated using GEANT4 [3] for 60 MeV protons and 300 MeV π^+ with a $\varnothing 60 \times 4$ µm InGaAs sensitive volume in a $300 \times 150 \times 50$ µm InP substrate used as a photodiode model. The simulation was run for three different angles of incidence: 0°, 80° and 90°, where the 90° orientation corresponds to particles incident parallel to the plane of the sensitive volume diameter and 0° is orthogonal to that plane, as illustrated in Figure 5.3.

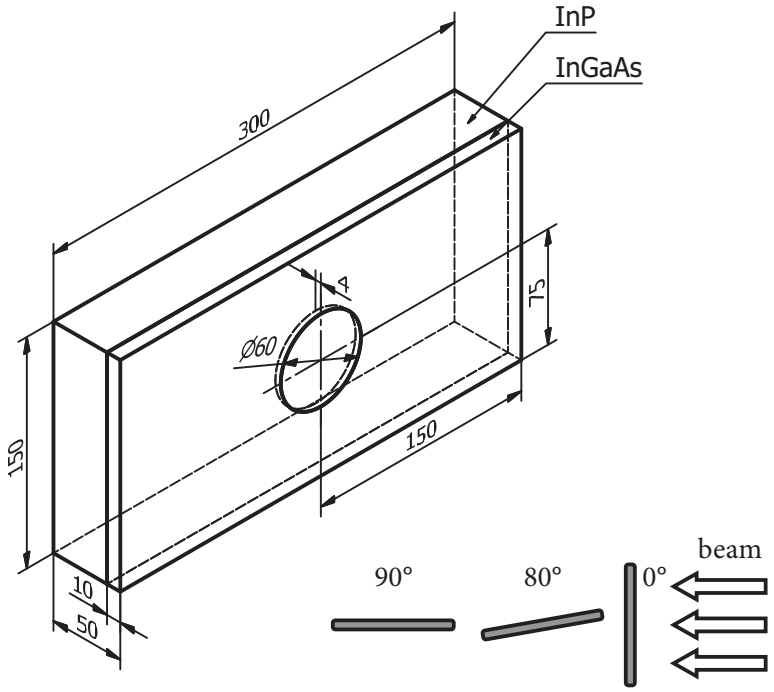

Figure 5.3: Photodiode model and its orientation to the beam (dimensions in µm).

The complete QGSP_BIC_HP physics list, which includes both ionising and non-ionising energy loss processes and high precision neutron package to transport neutrons below 20 MeV down to thermal energies, as recommended by the GEANT4 collaboration [34], was used to simulate low energy particle interactions with matter. To achieve a sufficiently high level of statistics, every simulation was run for at least 1 million hits – i.e interactions in the sensitive volume. The interaction cross-section σ_{i} was calculated as:

$$\sigma_{\text{i}} = \sigma_{\text{b}} \frac{N_{\text{h}}}{N_{\text{p}}}, \tag{5.2}$$

where σ_b is the beam cross-section, N_h the number of the hits and N_p is the total number of particles. The calculated value corresponds to the physical dimensions of the sensitive volume.

The results of simulations of energy deposited in the sensitive volume of the photodiode for 90° and 0° orientation are shown in Figure 5.4(a), 5.4(b), respectively. The π^+ have a lower energy deposit than protons for both orientations, as expected because of their lower mass and higher kinetic energy.

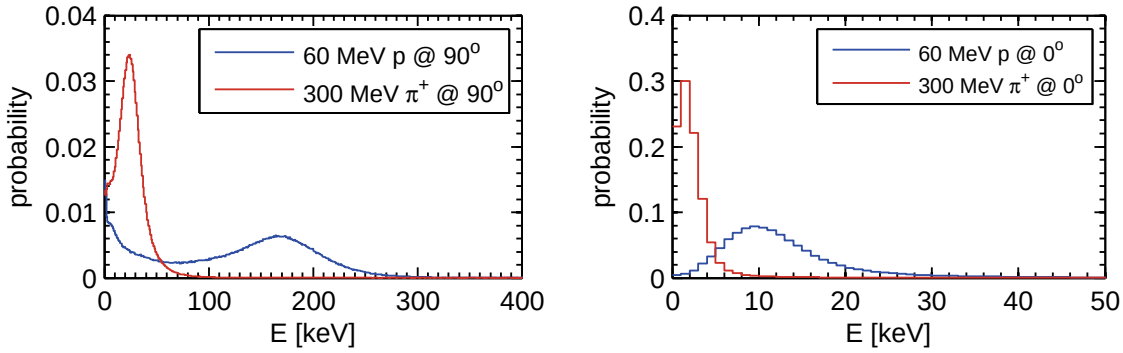

(a) 90° orientation (b) 0° orientation

Figure 5.4: Simulated energy deposit in ⌀60 × 4 µm InGaAs sensitive volume.

The energy scale was converted to a dBm scale of equivalent optical signal using the following relation:

$$P_{eq} = 10\log\left(\frac{q_e R}{rW} E_{dep}\right), \tag{5.3}$$

where P_{eq} is the power of an optical signal (in dBm), W is the ionization energy, which is 2.94 eV for InGaAs [13], r is the responsivity of a photodiode (in A/W), q_e is the electron charge (in C) and R is the data-rate (in s^{-1}).

5.2.2 SEU simulation with optical pulses

In order to determine the value of E_{crit}, a *Pulse Injection Test* was set up. The experimental set-up is similar to the one used in SEU measurements [52], except for the fact that instead of incident protons an optical pulse is used as shown in Figure 5.5.

For a given power of the 2.5 Gb/s pseudo-random optical data pattern signal, the shape of the detector threshold curve was scanned by changing the amplitude of optical error pulses and measuring the BER of the system. The optical error pulses were not synchronized with the data pattern signal during the measurement.

The dependence of BER on the OMA of error pulses for three different levels of data pattern signal is shown in Figure 5.6. The points represent the measured values. Due to the inability of the Altera BER tester to cope with high bit-error rates, the behaviour of detector threshold was

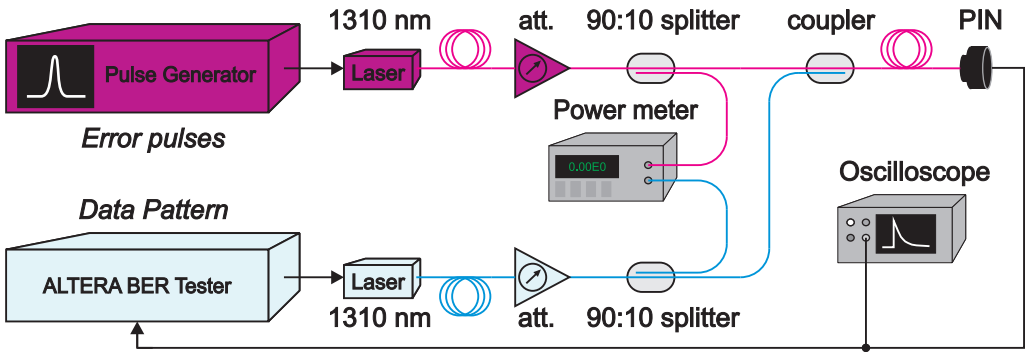

Figure 5.5: Pulse injection test schematics. A pulse generator is used as a source of error pulses which are coupled to the data pattern stream. The OMA of both optical signals can be individually set and is measured by an optical power meter.

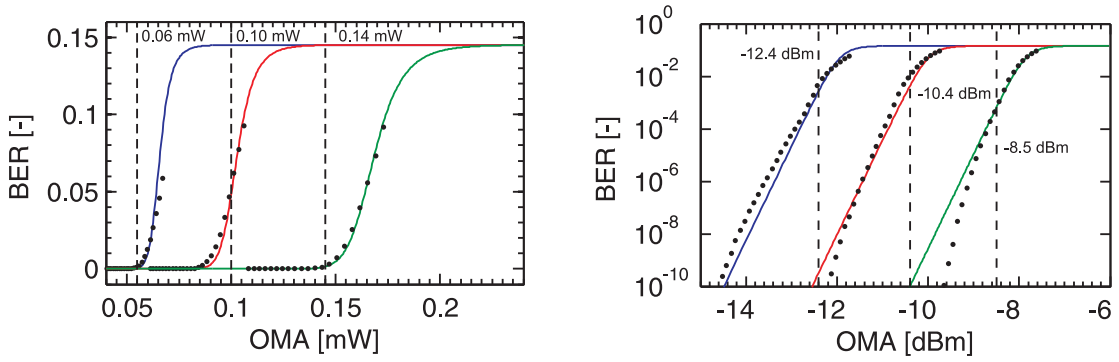

(a) linear scale

(b) logarithmic scale

Figure 5.6: Fitted curves of BER versus OMA of optical error pulses for three different OMAs of a 2.5 Gb/s data pattern.

extrapolated for higher OMA. The saturation limit was given by the ratio of data pattern and error pulses data rates which represents the maximum allowable BER. The measured data were fitted by a modified high-pass Bessel filter:

$$H(x) = \frac{(x/b)^{34}}{1 + (x/b)^{17} + (x/b)^{34}}. \tag{5.4}$$

In this particular case, the parameter b is directly proportional to the OMA of the data pattern signal.

5.3 Comparison between model and data

The bit-error cross-section was calculated as a parametric convolution of the deposited energy and threshold curves, i.e. simulated data from Figure 5.4 convoluted with the equation (5.4). The results for protons, π^+ and neutrons are shown in Figure 5.7.

The difference between proton and π^+ bit-error cross-section is apparent. According to the simulation, both the direct ionization losses and losses by nuclear interactions of π^+ are less significant than those of protons. This statement, however, is still to be proven experimentally. The bit-error cross-section curves of neutrons for 0° and 90° orientation illustrate the contribution of nuclear interactions to the overall bit-error cross-section.

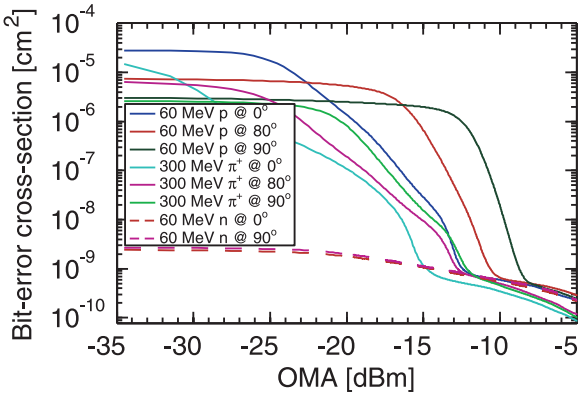

Figure 5.7: Dependence of simulated bit-error cross-section on OMA for the 2.5 Gb/s data pattern signal in $\varnothing 60 \times 4$ µm InGaAs sensitive volume for protons, neutrons and π^+.

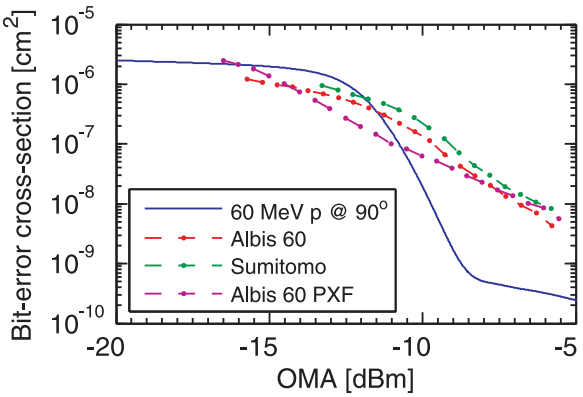

Figure 5.8: Comparison of simulated bit-error cross-section with measured data for three different devices with $\varnothing 60 \times 4$ µm InGaAs sensitive volume at 90° for the 2.5 Gb/s data pattern signal.

The comparison of the simulated bit-error cross-section of protons at 90° orientation with measured data derived from [52] for three different commercially available devices with similar sensitive volume dimensions is depicted in Figure 5.8.

The evident absence of higher energy deposits in the simulation may be caused by the simplified photodiode model used. However, Figure 5.9 shows a comparison of an energy distribution of a simple photodiode model, the same one as is in Figure 5.4(a), with a model shielded by a ring of plastics and aluminium to simulate packaging. It can be clearly seen that the energy distributions are identical; thus the surrounding material does not have any significant impact on deposited energy of 60 MeV protons in the active volume of the photodiode. Another reason for this discrepancy might arise from the simulation tool used, in this case GEANT4. This is contradicted by comparison of simulated bit-error cross-sections with former FLUKA simulations [30]. Figure 5.10 clearly demonstrates that both results from GEANT4 and FLUKA give very similar results. This disagreement between model and data will stay unresolved in this work.

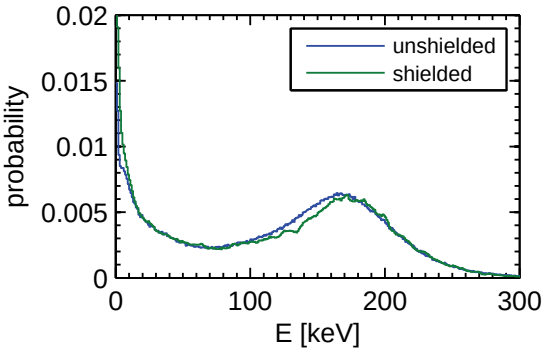

Figure 5.9: Comparison of simulated energy deposit for shielded and bare photodiode model.

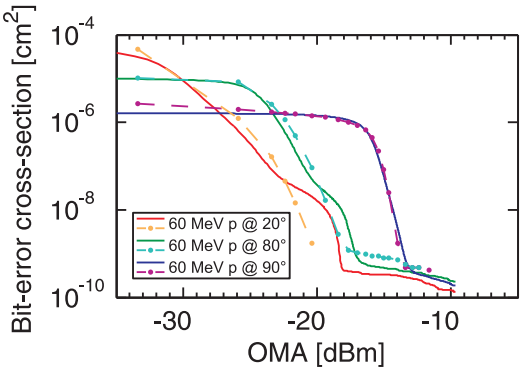

Figure 5.10: Comparison of simulated bit-error cross-sections using GEANT4 – solid line – and FLUKA – dashed line – tools for different angles of incidence.

Chapter 6

Use of optoelectronic devices in digital data transmission systems in HEP detectors

6.1 General optical link review

This section reviews a general bi-directional optical link between front-end and back-end for future particle detectors with its main components. Key parameters of a transmission chain are identified and a description of data flow with required transfer rate and error rate is provided for both uplink and downlink.

An optical link always consists of three main elements: an optical transmitter, optical fibre and an optical receiver. In addition, several connectors or splices are used to join individual optical fibre sections. Bi-directionality of the system is achieved either by two point-to-point links which transmit in opposite directions or by only one fibre with splitters and couplers to couple the transmitting and receiving sides.

The uplink branch, which transmits data from the detector, is characterized by high data-rates, of the order of Gb/s, with relatively low error rate. This results in a need for fast and powerful lasers as transmitters. The accompanying laser drivers have to provide high enough currents for bias and modulation of the laser during the whole lifetime of the experiments. Both laser threshold increase and efficiency decrease caused by radiation degradation of the components magnify already stringent demands on laser drivers.

Conversely to the uplink, the downlink transmits only control and timing signals to detectors. In this case minimum error rate is more important than the data-rate. Receiving electronics has to be sensitive enough to compensate for the radiation induced decrease in responsivity of the photodiode while sinking leakage current which may increase by several orders of magnitude.

A way to proceed when designing an optical fibre link in HEP environments involves in the first instance a power budget calculation with radiation degradation of the link components taken into account. To ensure a high reliability of the link in the radiation environment, tools

for link performance monitoring must be also considered at the design stage. The following sections deal with these issues more in detail.

6.2 System performance prediction in HEP environment

The prediction of high-speed data transmission system behaviour in high radiation environments, which are typically those of the final application, is of paramount importance for system design and reliability. There are several factors which have an impact on performance of the electro-optical system. The front-end part of the system has to be designed to sustain high radiation doses over the whole lifetime of the experiment. Since the lifetime is of the order of at least ten years, the ageing of the components also becomes an issue. Some parts of the system may be operated at low temperatures, typically tens of degrees below zero degrees Celsius. The impact of these external influences on individual components has to be carefully studied in order to design a reliable system.

6.2.1 The power budget calculation

The first step in optical data transmission system design is to determine how much power has to be transmitted and how sensitive receivers need to be in order to ensure the required speed and error rate, taking into account all the losses in the transmission chain. Another step is to define the allowable margin for component degradation. This margin includes the reduction of responsivity and the increase of leakage current of photodetectors as well as fibre attenuation caused by radiation. The laser performance degradation caused by radiation will be mitigated by the increase of laser drive current such that the transmitting power is kept above the required level during the whole life-time of the experiment.

The process of power budget calculation starts with an allocation of available link power, difference between minimum transmitted power and receiver sensitivity, into all lossy components of a transmission chain. Insertion losses, fibre attenuation, link penalties and radiation allowance are all taken into account. Any unconsumed injected power represents the power margin of a link.

In the framework of the Versatile link project, two operating wavelengths of 850 and 1310 nm are specified. This represents four different link configurations in total with uplink and downlink for each wavelength. The open source IEEE 10GbE link model available as a Microsoft Office Excel spreadsheet [24] was used to determine key link specifications. This non-linear model calculates link power penalties as a function of data-rate and link length. The predicted penalty for the 150 m long link, specified by the Versatile link, is 1.0 dB and 1.5 dB at 850 nm and 1310 nm respectively. These values are not significant for such a short link but for a longer one link the penalty might become an issue.

In addition to the link penalties, fibre attenuation is 3.5 and 0.4 dB/km for multi-mode and single-mode fibres, respectively. As for insertion losses, a maximum of four connections of no

more than 0.5 dB each resulting in 2.0 dB loss in total are incorporated in the power budget.

Concerning the radiation allowance, two variants of the Versatile link are specified using 20 MeV neutrons as a benchmark to distinguish if high-radiation tolerance components or intermediate tolerance componens shall be used. One tracker-grade variant with total fluence of 6×10^{15} n/cm^2 and one calorimeter-grade with total fluence of 5×10^{14} n/cm^2. These levels correspond to evenly distributed fluxes over 10 years of 1.9×10^7 n/cm^2/s and 1.6×10^6 n/cm^2/s, respectively. The corresponding link penalties are 5.4 dB for tracker-grade and 2.5 dB for calorimeter-grade link for both 850 and 1310 nm operation, confront Figure 4.23. InGaAs photodiodes are considered for both operating wavelengths. This possibility was well demonstrated in section 4.4.2. Up to the tracker-grade neutron fluence, the increase in photodiode leakage current is well below a maximum specified receiver sink current of 1 mA. The radiation induced attenuation in fibres qualified for Versatile link should not exceed 1.0 dB for multi-mode fibre and 0.05 dB for single-mode fibre.

6.2.2 The flux dependence of device performance degradation

Due to a fact that lasers anneal a significant part of their radiation induced damage, the total degradation will be different for devices placed at locations with different radiation intensity but with the same accumulated dose. However, this will contribute to the possibility of using less radiation resistant devices in locations with lower radiation fields.

The laser degradation model described in section 4.7 allows the prediction of laser degradation for arbitrary flux profiles. Figure 6.1 shows the relative laser threshold increase of three different lasers up to a fluence of 10^{15} n/cm^2 for different fluxes.

It can clearly be seen that for lower fluxes the increase in laser threshold current saturates. In other words, the amount of threshold increase does not depend on flux, provided that the flux is low enough. This behaviour is due to the fact that part of the radiation-induced damage in lasers is permanent. The biggest difference in the relative threshold increase between high and low fluxes is for the short-wavelength VCSEL, a laser which exhibits the largest amount of annealing of all the tested devices.

The knowledge of laser degradation as a function of particle flux is also beneficial for the radiation testing of lasers. Irradiation tests are carried at much higher fluxes, generally three to four orders of magnitude higher than those present at final applications. The flux scaling thus enables the transformation of measured degradation to the environment present in HEP detectors.

As a demonstration, Figure 6.2 and 6.3 show predicted *L-I* curves of a Mitsubishi Fabry-Pérot laser and Finisar VCSEL for tracker-grade and calorimeter-grade environment, respectively. These plots will find their importance in design of a compensation mechanism for radiation induced degradation in various places inside a detector. The degradation of *L-I* curves was calculated using a laser model described in section 4.7. Data were taken from Louvain irradiation campaign in 2010.

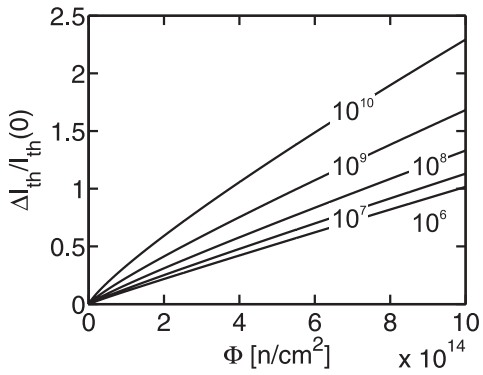

(a) Mitsubishi Fabry-Pérot laser.

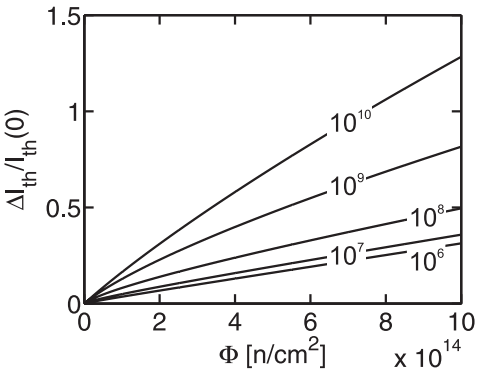

(b) Finisar VCSEL.

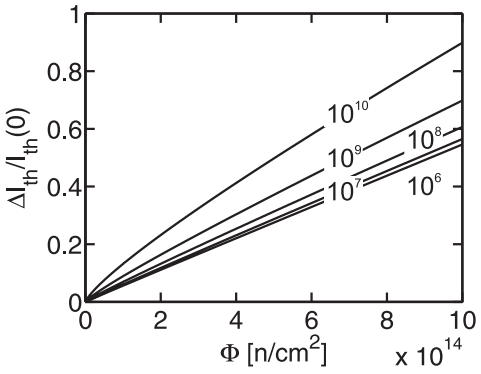

(c) BeamExpress VCSEL.

Figure 6.1: Simulated relative threshold increase up to a fluence of 10^{15} n/cm^2 for different fluxes in [n/cm^2/s].

6.2.3 Impact on system

Knowing the beam activity foreseen over the lifetime of the experiment with the radiation density map, the system performance degradation can be predicted and then confronted with the available power budget. In this way, the right components will be selected for the final application.

Accelerators in HEP almost always operate with some longer or shorter interruptions. These beam-off periods represent annealing periods for various devices. The total accumulated radiation damage will be thus lower than if it were acquired in one go. This presents a significant advantage in selection of candidate devices.

For the LHC machine one can estimate the annual contribution to the increase of laser threshold current to be composed of 2 800 hours followed by a beam inactivity for the rest of the year. Figure 6.4 shows the estimated accumulated relative threshold current increase of 1310 nm Fabry-Pérot laser during 10 years of LHC and HL-LHC operation. The flux profile for LHC was set as 0.2×10^6, 0.66×10^6, 1.3×10^6, and 2×10^6 n/cm^2/s during the first year, second, third and the rest of the operation, respectively. The simulated flux profile for HL-LHC was ten-times higher.

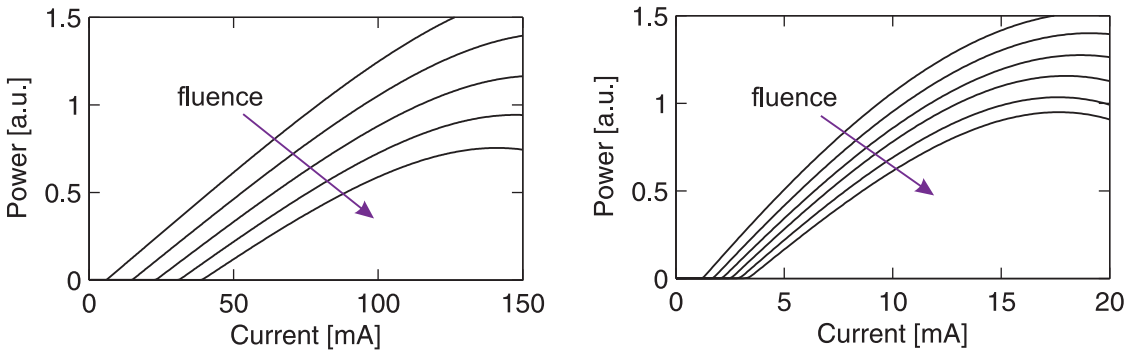

(a) Mitsubishi Fabry-Pérot laser.

(b) Finisar VCSEL.

Figure 6.2: Simulated degradation of *L-I* curves for tracker-grade Versatile link. The curves represent a degradation due to a radiation induced damage up to a total fluence of 6×10^{15} n/cm^2 in equidistant steps.

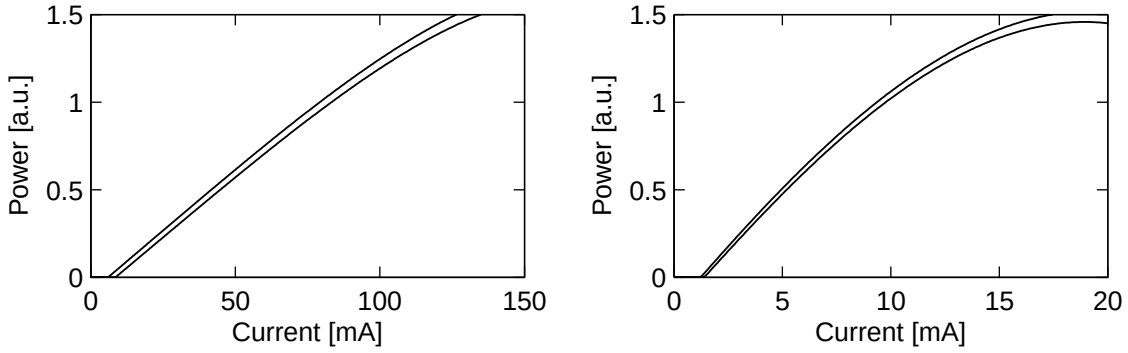

(a) Mitsubishi Fabry-Pérot laser.

(b) Finisar VCSEL.

Figure 6.3: Simulated degradation of *L-I* curves for calorimeter-grade Versatile link. The left curve is for an unirradiated laser while the right one is for a laser irradiated up to a fluence of 5×10^{14} n/cm^2.

The particular device chosen to demonstrate the effect has a pre-irradiation threshold current in the range of 5–10 mA, which means that the expected increase in laser threshold current for HL-LHC operation is 8–18 mA. The laser driver used in Versatile link project has a design maximum bias current of 45 mA which easily accommodates such change. The situation is even simpler for VCSELs whose threshold current increase as well as threshold current itself is minimal compared to edge-emitting lasers. Several devices meet the requirements for use in HL-LHC trackers. As a result, there is no power budget penalty for uplink transmitters as was assumed in section 6.2.1.

Due to the minimal annealing of photodiodes, the total radiation damage is not flux dependent. The selection of the right component for the final application can be made directly from measured data taken during the testing at irradiation facilities. The only restriction in terms of radiation hardness is the required maximum fluence and available power budget.

Referring back to section 6.2.1, the four variants of the Versatile link power budget are summarized in Table 6.1. Both uplink and 1310 nm downlink variants meet the 10GbE specifi-

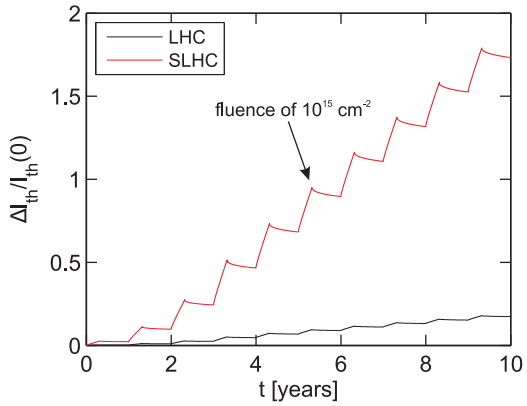

Figure 6.4: Calculated relative laser threshold current increase for a 1310 nm Fabry-Pérot laser during 10 years of LHC and HL-LHC operation with alternating beam-on and beam-off periods.

cation with some margin, mostly owing to the short length of the link. However, the downlink at 850 nm is not 10GbE compliant due to the radiation degradation of photodetectors. The versatile receiver and its corresponding transmitter must exceed the standard component specifications. The receiver sensitivity was set to −13.1 dBm for 850 nm operation. The remainder of the power deficit is compensated by an increase of transmitted power. The calculated margin can be improved by an additional 2–3 dB by an error coding scheme.

	850 nm uplink	**850 nm downlink**	**1310 nm uplink**	**1310 nm downlink**
Transceiver power level				
min. transmitted OMA	−3.8 dBm	−3.1 dBm	−3.2 dBm	−3.2 dBm
min. receiver OMA	−11.1 dBm	−13.1 dBm	−12.6 dBm	−12.6 dBm
Power budget Tx−Rx	7.3 dB	10.0 dB	9.4 dB	9.4 dB
insertion losses	2.0 dB	2.0 dB	2.0 dB	2.0 dB
fibre attenuation	0.6 dB	0.6 dB	0.1 dB	0.1 dB
link penalty	1.0 dB	1.0 dB	1.5 dB	1.5 dB
Rx radiation degrad.	–	5.4 dB	–	5.4 dB
fibre radiation degrad.	1.0 dB	1.0 dB	–	–
Margin	2.7 dB	0.0 dB	5.8 dB	0.4 dB

Table 6.1: Four power budget variants of the Versatile link.

6.3 Online system performance monitoring

The online monitoring of system performance will be required in order to determine how much the devices are degraded during the running of the experiment and also to adjust the operating settings to compensate for the radiation induced damage.

6.3.1 Compensation of radiation-induced system degradation

On the transmitter side, laser threshold increases and efficiency decreases with accumulated dose, thus lasers need an adjustment of bias and modulation current in order to preserve the design data rate. This compensation for radiation induced damage of a laser is well demonstrated in Figure 6.5. There are several methods to achieve this task depending on indicator signals which are available in the current system. Photodetectors are compensated automatically for changes in leakage current and responsivity by a TIA.

6.3.2 Systems with a Receive Signal Strength Indicator

These systems have a direct indicator of an input signal strength and the adjustment of laser bias and modulation current is relatively easy. It is sufficient to change the bias point with a known modulation amplitude. Once there is a change in received signal power, the laser threshold can be tripped by a low edge of the modulated signal as illustrated in Figure 6.6. The laser threshold can be roughly determined as a bias current minus modulation amplitude. This measurement is relatively easy to perform during the beam-off periods. The correct operation of a laser transmitter is achieved with minimum effort.

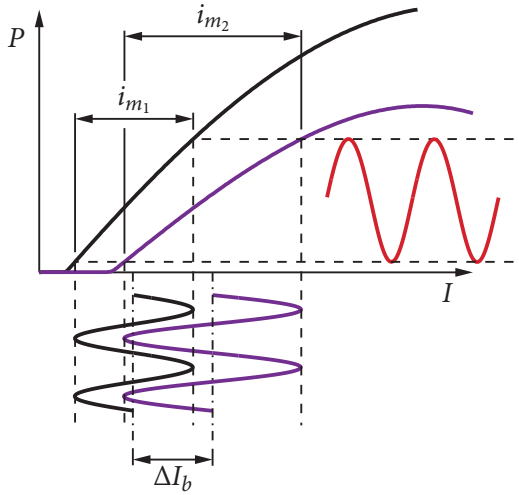

Figure 6.5: The compensation of laser bias I_b and modulation current i_m to maintain constant output power due to radiation damage.

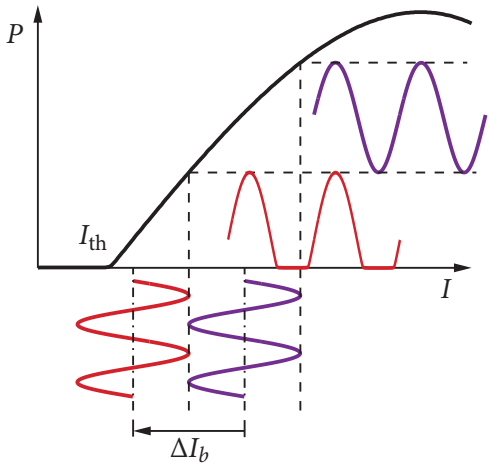

Figure 6.6: Tripping of the lower edge of the output signal due to a decrease in laser bias current I_b.

6.3.3 Systems without a Receive Signal Strength Indicator

Since there is no means to directly determine the input signal strength, it must be measured indirectly by changing bias and modulation current, as in the previous case, while observing changes in bit error rate.

A prerequisite of this method is a well known signal pattern for which the BER can be measured. The modulation signal of a laser needs to be set to a minimal value for which the BER

is below the measuring resolution. In this way, the modulation signal serves as a scanning window and the bias current can be subsequently reduced until the BER rises. The laser threshold current is then deduced from the shape of the measured BER curve. The precision of this measurement depends on a steepness of the BER curve.

This method is not as straightforward as the previous one. A special signal pattern must be implemented in the serializer, as is the case of the GBTX, and the measured BER curve has to be analysed. However, satisfactory results can be obtained and the measurement itself can be automated with careful programming. A correct calibration of the system is essential prior to its deployment.

If this measurement is not possible for some reason, the worst case scenario has to be employed. In the beginning, bias and modulation currents are set to a values which corresponds to a maximum predicted radiation induced damage. The biggest disadvantage of this method is its huge power consumption and the associated high laser currents which negatively affect the ageing of the lasers.

There still remains one straightforward method which has to be mentioned. It is the direct measurement per channel with an optical power meter. This method is feasible only for systems with limited number of links. Unfortunately, this is definitely not the case of the HEP experiments.

Chapter 7

Summary and Conclusion

An overview of current optical link architectures of the ATLAS and CMS experiments has been presented in the context of the LHC upgrade to the HL-LHC which requires a new radiation-hard readout based on the Versatile Link framework. The emphasis was placed on the increased radiation environment of the HL-LHC and its impact on the radiation hardness of optoelectronic components.

Basic operational principles of semiconductor lasers and p-i-n photodiodes were outlined together with a review of radiation effects in these devices. Both total fluence irradiation effects and SEUs in optoelectronic components were introduced. A description of laser operation via rate-equations currently found in literature for both steady state and small signal analysis was also introduced.

Results of three irradiation campaigns of semiconductor lasers and p-i-n photodiodes were presented. A very large number of edge-emitting lasers and VCSELs with p-i-n photodiodes operating at both 850 and 1310 nm wavelengths were tested. Several 850 and 1310 nm candidate devices for the Versatile Link transceiver were identified. The outcome of these tests confirmed the assumption that VCSELs are more radiation hard than edge emitting lasers. Globally, modern fast devices perform better than their predecessors which are currently used by the LHC experiments.

It was shown that, in contrast to p-i-n photodiodes, lasers are able to recover a substantial part of the induced damage. They even start lasing again after their apparent destruction by radiation. This will be significant in the final application where the irradiation to maximum fluence takes place over the system lifetime which is typically measured in years. A surprising result of the last neutron test is that laser annealing does not depend on laser bias current. The annealing rate is affected by the junction temperature whose increase can be a result of increased current density in the device. Previous results found in the literature can be explained by this mechanism.

For the description and prediction of the laser behaviour during and after irradiation a compact rate-equation based model was devised. Good agreement between the calculated/predicted and measured values was reached in both neutron and pion tests. This model has widespread applicability in future irradiation test refinements. It will help to minimize the time spent in

irradiation facilities.

Irradiation by two particle species allowed the comparison of their destructiveness. Simulations of NIEL in various semiconductor compounds were attempted using FLUKA and GEANT4. Of these two only FLUKA results were considered. Even though FLUKA predicts higher NIEL for GaAs than the one found in literature, the finding that 191 MeV pions are approximately twice as damaging as 20 MeV neutrons is in accordance with the experimental data.

In addition to the laser degradation model, a method developed to simulate Single Event Upset effects in photodetectors was presented. The method allows comparison of the SEU effects of different particles impinging on various detector materials. Unfortunately this method was based on GEANT4 simulations and a discrepancy between simulated and measured data was found. Simulations of energy deposit using FLUKA might have produced a better agreement with experimental data.

Last chapter presents different methods of online performance monitoring of optical links and their performance prediction under various conditions.

7.1 Further research opportunities

The topic of radiation testing of optoelectronic components is extensive and there are certain areas which deserve further attention. These are mainly in theoretical background. Present NIEL calculations are rather basic and as new semiconductor compounds emerge, the knowledge of the NIEL in radiation field becomes more and more important. For example the overall effect of a tracker radiation environment on devices would be of high interest.

Concerning the laser rate-equation model, the physical meaning of fitting constants remains yet to be fully understood. The model was developed to describe laser behaviour using a minimal set of free parameters. However, the knowledge of which laser parameters are affected by radiation, and how, is also important. In this way, new radiation hard lasers could be designed.

Bibliography

[1] Abdesselam, A., et al.: *The Optical Links of the ATLAS SemiConductor Tracker*. Tech. Rep. ATL-INDET-PUB-2007-013, CERN, Geneva, Aug 2007.

[2] Acosta, D., et al.: *CMS physics: Technical Design Report*. Geneva: CERN, 2006.

[3] Agostinelli, S., et al.: *GEANT4 – a simulation toolkit*. *Nucl. Instrum. Methods Phys. Res. A*, 2003, vol. 506, pp. 250–303.

[4] Agrawal, G. P.: *Spectral hole-burning and gain saturation in semiconductor lasers: Strong-signal theory*. *J. Appl. Phys.*, 1988, vol. 63, no. 4, pp. 1 232–1 235.

[5] Agrawal, G. P.: *Effect of Gain and Index Nonlinearities on Single-Mode Dynamics in Semiconductor Lasers*. *IEEE Quantum Electron.*, 1990, vol. 26, no. 11, pp. 1 901–1 909.

[6] Agrawal, G. P., Dutta, N. K.: *Semiconductor Lasers*. 2nd ed., New York: Van Nostrand Reinhold, 1993, ISBN: 0-442-01102-4.

[7] Amaral, L., et al.: *Evaluation of Multi-Gbps Optical Transceivers for Use in Future HEP Experiments*. In *Topical Workshop on Electronics for Particle Physics*, Naxos, 2008 pp. 151–155.

[8] Amaral, L., et al.: *The versatile link, a common project for super-LHC*. *J. Instrum.*, 2009, vol. 4, p. 12 003.

[9] Arms, K. E., et al.: *ATLAS Pixel Opto-Electronics*. *Nucl. Instrum. Methods Phys. Res. A*, 2005, vol. 554, pp. 458–468.

[10] Axer, M., et al.: *First High Fluence Irradiation Tests of Lasers for Upgraded CMS at SLHC*. In *11th Workshop on Electronics for LHC and Future Experiments*, Lyons, 2005 pp. 316–320.

[11] Barnes, C. E.: *Effects of Co^{60} Gamma Irradiation on Epitaxial GaAs Laser Diodes*. *Phys. Rev. B*, 1970, vol. 1, no. 12, pp. 4 735–4 747.

[12] Barnes, C. E.: *Increased radiation hardness of GaAs laser diodes at high current densities*. *J. Appl. Phys.*, 1970, vol. 45, no. 8, pp. 3 485–3 489.

[13] Belogurov, S., et al.: *InGaAs photodiode as an ionizing particle detector*. *Nucl. Instrum. Methods Phys. Res. A*, 2000, vol. 452, pp. 377–380.

[14] Bortoletto, D.: *The atlas and cms Plans for the lhc Luminosity Upgrade*. In *19th Hadron Collider Physics Symposium*, Galena, 2008 In print.

[15] Bowers, J.: *High speed semiconductor laser design and performance*. *Solid State Electron*, 1987, vol. 30, no. 1, pp. 1–11.

[16] Bruensteiner, M., Papen, G. C.: *Extraction of vcsel Rate-Equation Parameters for Low-Bias System Simulation*. *ieee Quantum Electron.*, 1999, vol. 5, no. 3, pp. 487–494.

[17] Brüning, O. S., et al., eds.: *Lhc Design Report*. Geneva: cern, 2004.

[18] Buchanan, N. J., et al.: *Design and implementation of the Front End Board for the readout of the atlas liquid argon calorimeters*. *J. Instrum.*, 2008, vol. 3.

[19] Campabadal, F., et al.: *Design and performance of the abcd3ta asic for readout of silicon strip detectors in the atlas semiconductor tracker*. *Nucl. Instrum. Methods Phys. Res. A*, 2005, vol. 552, pp. 292–328.

[20] Carson, R. F., Chow, W. W.: *Neutron effects in high-power GaAs laser diodes*. *ieee Trans. Nucl. Sci.*, 1989, vol. 36, no. 6, pp. 2 076–2 082.

[21] Checcucci, B., et al.: *Joint atlas-cms working group on optical links. Optical Link Evaluation Criteria and Test Procedures*. Tech. rep., cern, Geneva, Jan 2007.

[22] Chilingarov, A., Meyer, J. S., Sloan, T.: *Radiation Damage due to niel in GaAs Particle Detectors*. Tech. Rep. INDET-NO-134, cern, Geneva, Jun 1996.

[23] Chu, M. L., et al.: *Radiation hardness studies of vcsels and pins for the opto-links of the Atlas SemiConductor Tracker*. *Nucl. Instrum. Methods Phys. Res. A*, 2005, vol. 579, pp. 795–800.

[24] Dawe, P., et al.: *ieee 10GbE link model*. url: <http://www.ieee802.org/3/ae/public/adhoc/serial_pmd/documents/>.

[25] de Rijk, G.: *Functioning collaboration communication structure*. Tech. rep., cern, Geneva, Feb 2009, url: <http://info-slhc-pp.web.cern.ch/>.

[26] Duzellier, S., et al.: *Seu Induced by Pions in Memories from Different Generations*. *ieee Trans. Nucl. Sci.*, 2001, vol. 48, no. 6, pp. 1 960–1 965.

[27] Ellis, J.: *Beyond the standard model with the lhc*. *Nature*, 2007, vol. 448, pp. 297–301.

[28] Encyclopædia Britannica Inc.: *Photoelectric effect*. 2012, url: <http://www.britannica.com/EBchecked/topic/457841/photoelectric-effect>.

[29] Evans, B., Hager, H., Hughlock, B.: *5.5-MeV Proton Irradiation of a Strained Quantum-Well Laser Diode and a Multiple Quantum-Well Broad-Band led*. *ieee Trans. Nucl. Sci.*, 1993, vol. 40, no. 6, pp. 1 645–1 654.

[30] Faccio, F., et al.: *Single event upset tests of an 80 Mbit/s optical receiver*. *ieee Trans. Nucl. Sci.*, 2000, vol. 48, no. 5, pp. 1 700–1 707.

[31] Fukushima, T., et al.: *Relative Intensity Noise Reduction in InGaAs /InP Multiple Quantum Well Lasers with Low Nonlinear Damping*. *ieee Photon. Technol. Lett.*, 1991, vol. 3, no. 8, pp. 691–693.

[32] Gan, K. K., et al.: *Joint atlas-cms working group on optical links. Lessons Learned and to be Learned from lhc*. Tech. rep., cern, Geneva, Nov 2007.

[33] Gan, K. K., et al.: *Joint atlas-cms working group on optical links. Optical System Irradiation Guidelines*. Tech. rep., cern, Geneva, Nov 2007.

[34] *Geant4 Reference Physics Lists*. url: <http://geant4.web.cern.ch/geant4/support/proc_mod_catalog/physics_lists/referencePL.shtml>.

[35] Gill, K., Troska, J., Vasey, F.: *Cms Tracker Optical Links Quality Assurance Manual*. Tech. Rep. CMS-TK-MA-0001, cern, Geneva, Apr 2001.

[36] Gill, K., et al.: *Radiation damage studies of optoelectronic components for the cms tracker optical links*. In *3rd Workshop on Electronics for lhc Experiments*, London, 1997 pp. 276–281.

[37] Gill, K., et al.: *Comparative study of radiation hardness of optoelectronic components for the cms tracker optical links*. In *4th Workshop on Electronics for lhc Experiments*, Rome, 1998 pp. 96–99.

[38] Gill, K., et al.: *Radiation damage studies of optical link components for applications in future high-energy physics experiments*. *Proc. spie*, 1998, vol. 3440, pp. 89–99.

[39] Gill, K., et al.: *Radiation damage and annealing in 1310 nm InGaAsP/InP lasers for the cms tracker*. *Proc. spie*, 2000, vol. 4134, pp. 176–184.

[40] Gill, K., et al.: *Combined radiation damage, annealing, and ageing studies of InGaAsP/InP 1310 nm lasers for the cms tracker optical links*. *Proc. spie*, 2002, vol. 4823, pp. 19–33.

[41] Gill, K., et al.: *Radiation Hardness Qualification of InGaAsP/InP 1310 nm Lasers for the cms Tracker Optical Links*. *ieee Trans. Nucl. Sci.*, 2002, vol. 49, no. 6, pp. 2 923–2 929.

[42] Gill, K., et al.: *High Statistics Testing of Radiation Hardness and Reliability of Lasers and Photodiodes*. In *10th Workshop on Electronics for lhc and Future Experiments*, Boston, 2004 pp. 153–157.

[43] Grahl, J.: *Optical Data Links in cms ecal*. In *10th Workshop on Electronics for lhc and Future Experiments*, Boston, 2004 pp. 158–163.

[44] Gregor, I.-M.: *Optical Links for the atlas Pixel Detector*. Ph.D. thesis, Bergische Universität Wuppertal, Fachbereich Physik, Wuppertal, 2001.

[45] Gregor, I.-M., et al.: *Optical data links for the atlas sct and Pixel Detector*. *Nucl. Instrum. Methods Phys. Res. A*, 2001, vol. 465, no. 1, pp. 131–134.

[46] Hadley, G. R., et al.: *Comprehensive Numerical Modeling of Vertical- Cavity Surface-Emitting Lasers*. *ieee Quantum Electron.*, 1996, vol. 32, no. 4, pp. 607–616.

[47] Haywood, S.: *Atlas inner detector: Technical Design Report*. Geneva: cern, 1997.

[48] Hessey, N. P.: *Overview and Electronics Needs of atlas and cms High Luminosity Upgrades*. In *Topical Workshop on Electronics for Particle Physics*, Naxos, 2008 pp. 323–327.

[49] Huhtinen, M.: *Simulation of non-ionising energy loss and defect formation in silicon. Nucl. Instrum. Methods Phys. Res. A*, 2002, vol. 491, pp. 194–215.

[50] Huhtinen, M., Faccio, F.: *Computational method to estimate Single Event Upset rates in an accelerator environment. Nucl. Instrum. Methods Phys. Res. A*, 2000, vol. 450, pp. 155–172.

[51] Ioffe Physico-Technical Institute: *New Semiconductor Materials. Characteristics and Properties*. url: <http://www.ioffe.ru/SVA/NSM/>.

[52] Jimenez Pacheco, A., et al.: *Single-Event Upsets in Photoreceivers for Multi-Gb/s Data Transmission. ieee Trans. Nucl. Sci.*, 2009, vol. 56, no. 4, pp. 1 978–1 986.

[53] Karimäki, V.: *Cms tracker system project: Technical Design Report*. Geneva: cern, 1997.

[54] Laird, J. S., et al.: *A comparison of heavy ion and picosecond laser microbeams for investigating single event transients in InGaAs on InP photodetectors. Nucl. Instrum. Methods Phys. Res. B*, 2003, vol. 210, pp. 243–249.

[55] Li, Z.-M., Bradford, T.: *A Comparative Study of Temperature Sensitivity of InGaAsP and AlGaAs mqw Lasers Using Numerical Simulations. ieee Quantum Electron.*, 1995, vol. 31, no. 10, pp. 1 841–1 847.

[56] Lim, C., Iezekiel, S., Nowden, C.: *Effects of Current-Dependent and Frequency-Dependent Gain Suppression on the Nonlinear Dynamics of Semiconductor Lasers*. In *8th ieee International Symposium on High Performance Electron Devices for Microwave and Optoelectronic Applications*, Glasgow, 2000 pp. 51–54.

[57] Macias, R., et al.: *Advance Validation of Radiation Hardness and Reliability of Lasers for cms Optical Links. ieee Trans. Nucl. Sci.*, 2005, vol. 52, no. 5, pp. 1 488–1 496.

[58] Marshall, P. W., Dale, C. J., Burke, E. A.: *Space Radiation Effects on Optoelectronic Materials and Components for a 1300 nm Fiber Optic Data Bus. ieee Trans. Nucl. Sci.*, 1992, vol. 39, no. 6, pp. 1 982–1 989.

[59] Marshall, P. W., Dale, C. J., LaBel, K. A.: *Space Radiation Effects in High Performance Fiber Optic Data Links for Satellite Data Management. ieee Trans. Nucl. Sci.*, 1996, vol. 43, no. 2, pp. 645–653.

[60] Mazza, G., et al.: *A radiation tolerant 5 Gb/s Laser Driver in 130 nm cmos technology. J. Instrum.*, Jan 2012, vol. 7.

[61] Mena, P. V., et al.: *A Comprehensive Circuit-Level Model of Vertical-Cavity Surface-Emitting Lasers. J. Lightwave Techn.*, 1999, vol. 17, no. 12, pp. 2 612–2 632.

[62] Mena, P. V., et al.: *A Simple Rate-Equation-Based Thermal vcsel Model. J. Lightwave Techn.*, 1999, vol. 17, no. 5, pp. 865–872.

[63] Menouni, M., et al.: *The gbtia, a 5 Gbit/s Radiation-Hard Optical Receiver for the slhc Upgrades*. In *Topical Workshop on Electronics for Particle Physics*, Paris, 2009 pp. 326–330.

[64] Messenger, S. R., et al.: *Proton Displacement Damage and Ionizing Dose for Shielded Devices in Space*. *ieee Trans. Nucl. Sci.*, 1997, vol. 44, no. 6, pp. 2 169–2 172.

[65] Messenger, S. R., et al.: *Modeling Solar Cell Degradation in Space: A Comparison of the nrl Displacement Damage Dose and the jpl Equivalent Fluence Approaches*. *Prog. Photovolt: Res. Appl.*, 2001, vol. 9, no. 2, pp. 103–121.

[66] Militaru, O.: *High flux neutron irradiation facility at Louvain-la-Neuve Cyclotron: What you need to know about neutron irradiation in T2*. Tech. rep., ucl, Louvain-la-Neuve, 2008.

[67] Moreira, P., et al.: *The gbt Project*. In *Topical Workshop on Electronics for Particle Physics*, Paris, 2009 pp. 342–346.

[68] Ng, W.-C., Liu, Y., Hess, K.: *Lattice Temperature Model and Temperature Effects in Oxide-Confined vcsel's*. *J. Comp. Electron.*, 2004, vol. 3, no. 2, pp. 103–116.

[69] Obarski, G. E., Splett, J. D.: *Transfer standard for the spectral density of relative intensity noise of optical fiber sources near 1550 nm*. *J. Opt. Soc. Am. B*, 2001, vol. 18, no. 6, pp. 750–761.

[70] Paganoni, M.: *The cms electromagnetic calorimeter*. *Nucl. Instrum. Methods Phys. Res. A*, 2004, vol. 535, pp. 461–465.

[71] Pailharey, E., et al.: *Degradation of carrier lifetime in irradiated lasers*. *Proc. spie*, 2000, vol. 4134, pp. 222–230.

[72] Raymond, M., et al.: *The apv25 0.25 µm cmos readout chip for the cms tracker*. In *47th ieee Nuclear Science Symposium and Medical Imaging Conference*, Heidelberg, 2000 pp. 113–118.

[73] Sadrozinski, H. F. W., Seiden, A.: *Tracking detectors for the slhc, the lhc upgrade*. *Nucl. Instrum. Methods Phys. Res. A*, 2005, vol. 541, pp. 434–440.

[74] Salathé, R., Voumard, C., Weber, H.: *Rate equation approach for diode lasers*. *Opt. Quant. Electron.*, 1974, vol. 6, no. 6, pp. 451–456.

[75] Saleh, B. E. A., Teich, M. C.: *Fundamentals of Photonics*. 2nd ed., New Jersey: Wiley, 2007, isbn: 0-471-35832-9.

[76] Scott, J. W., et al.: *Modeling Temperature Effects and Spatial Hole Burning to Optimize Vertical-Cavity Surface-Emitting Laser Performance*. *ieee Quantum Electron.*, 1993, vol. 29, no. 5, pp. 1 295–1 308.

[77] Silfvast, W. T.: *Laser Fundamentals*. 2nd ed., Cambridge: Cambridge Univ. Press, 2004, isbn: 0-521-83345-0.

[78] Statz, H., Tang, C. L., Lavine, J. M.: *Spectral Output of Semiconductor Lasers*. *J. Appl. Phys.*, 1964, vol. 35, no. 9, pp. 2 581–2 585.

[79] Stejskal, P.: *Development of VHDL Code for the DAQ and Monitoring Boards of the VELO Subdetector of the LHCb Experiment*. Master's thesis, České vysoké učení technické v Praze, Fakulta jaderná a fyzikálně inženýrská, Prague, 2007.

[80] Summers, G. P., et al.: *Damage Correlations in Semiconductors Exposed to Gamma, Electron and Proton Radiations*. *IEEE Trans. Nucl. Sci.*, 1993, vol. 40, no. 6, pp. 1 372–1 378.

[81] Summers, G. P., et al.: *A new approach to damage prediction for solar cells exposed to different radiations*. In *1st IEEE World Conference on Photovoltaic Energy Conversion*, vol. 2, Waikoloa, 1994 pp. 2 068–2 075.

[82] Tapprogge, S., ed.: *Outline of R&D activities for ATLAS at an upgraded LHC*, 2005.

[83] Teng, P. K., et al.: *Radiation hardness and lifetime studies of the VCSELs for the ATLAS SemiConductor Tracker*. *Nucl. Instrum. Methods Phys. Res. A*, 2003, vol. 497, pp. 294–304.

[84] The CMS Collaboration: *A New Boson with a Mass of 125 GeV Observed with the CMS Experiment at the Large Hadron Collider*. *Science*, 2012, vol. 338, no. 6114, pp. 1 569–1 575.

[85] Thompson, G. H. B.: *Physics of semiconductor laser devices*. Chichester: Wiley, 1980, ISBN: 0-471-27685-5.

[86] Troska, J.: *Radiation-hard optoelectronic data transfer for the CMS Tracker*. Ph.D. thesis, Imperial College London, London, 1999.

[87] Troska, J., et al.: *Neutron, Proton and Gamma Radiation Effects in Candidate InGaAs p-i-n Photodiodes for the CMS Tracker Optical Links*. Tech. Rep. CMS-NOTE-1997-102, CERN, Geneva, Dec 1997.

[88] Troska, J., et al.: *Optical readout and control systems for the CMS tracker*. *IEEE Trans. Nucl. Sci.*, 2003, vol. 50, no. 4, pp. 1 067–1 072.

[89] Troska, J., et al.: *Radiation Damage Studies of Lasers and Photodiodes for Use in Multi-Gb/s Optical Data Links*. *IEEE Trans. Nucl. Sci.*, 2011, vol. 58, no. 6, pp. 3 103–3 110.

[90] Vankov, P.: *ATLAS Upgrade for the HL-LHC: meeting the challenges of a five-fold increase in collision rate*. In *Hadron Collider Physics Symposium*, Paris, 2011 .

[91] Walters, R., et al.: *Space radiation effects in InP solar cells*. *IEEE Trans. Nucl. Sci.*, 1991, vol. 38, no. 6, pp. 1 153–1 158.

[92] Warner, J. H., et al.: *Displacement Damage Correlation of Proton and Silicon Ion Radiation in GaAs*. *IEEE Trans. Nucl. Sci.*, 2005, vol. 52, no. 6, pp. 2 678–2 682.

[93] Weaver, B. D., et al.: *Atomic disorder and the transition temperature of cuprate superconductors*. *Phys. Rev. B*, 1992, vol. 46, no. 2, p. 1 134–1 137.

[94] Weidberg, A. R.: *VCSEL reliability in ATLAS and development of robust arrays*. *J. Instrum.*, Jan 2012, vol. 7.

[95] Wermes, N., Hallewel, G.: *Atlas pixel detector: Technical Design Report*. Geneva: cern, 1998.

[96] Yao, J., et al.: *Semiconductor laser dynamics beyond the rate-equation approximation*. *Optics Comm.*, 1995, vol. 119, pp. 246–255.

[97] Yousefi, M., et al.: *Rate Equation Model for Semiconductor Lasers With Multilongitudinal Mode Competition and Gain Dynamics*. *ieee Quantum Electron.*, 2003, vol. 39, no. 10, pp. 1 229–1 237.

[98] Zee, B.: *Broadening Mechanism in Semiconductor (GaAs)Lasers: Limitations to Single Mode Power Emission*. *ieee Quantum Electron.*, 1978, vol. 14, no. 10, pp. 727–736.